

Investigation and development of dual-phase oxygen-transporting membranes for oxygen production and chemical reactors

Von der Naturwissenschaftlichen Fakultät
der Gottfried Wilhelm Leibniz Universität Hannover

zur Erlangung des Grades

Doktor der Naturwissenschaften

Dr. rer. nat.

genehmigte Dissertation

von

Wei Fang, Magister (China)

geboren am 10.02.1988 in Hefei, Anhui, China

2016

Referent: Prof. Dr. Armin Feldhoff

Korreferent: Prof. Dr. Chusheng Chen

Korreferent: Prof. Dr. Kevin Huang

Tag der Promotion: 11.11.2016

Preface

Energy is considered to be the lifeblood for the development of technology and economy. In the next decades, traditional fossil fuels will continue to be the most important energy resource to power human society. Thus, how to convert the fossil fuels into suitable forms of energy in a more efficient way will be of particular concern for future energy development and policy formulation. Besides, it is also urgent to minimize the environmental impact induced by industrial processes, such as CO₂ and NO_x emissions from conventional coal-fired power plants operated with air. Nowadays, a considerable amount of primary energy has been converted to electricity by combustion. Very recently, oxy-fuel combustion integrated with CO₂ capture emerges as a promising option to reduce the emissions of both CO₂ and NO_x drastically. However, pure oxygen supply is regarded as the main bottleneck of this technology for industrialization. Compared with the energy-intensive cryogenic distillation, oxygen-transporting membranes (OTMs) consisting of mixed ionic and electronic conducting (MIEC) materials have gained much attention as a potentially economical and efficient means of producing oxygen by separation from air or other oxygen-containing gas mixtures at elevated temperatures. Moreover, another unique advantage of OTM technology that have attracted increasing interest in research is to construct membrane reactors. For example, chemical reactions can be coupled with the membrane separation, which will benefit to process intensification and even result in a higher conversion of the reactant owing to the shift of chemical equilibrium.

Unfortunately, permeability and stability are the two foremost obstacles prohibiting the commercialization of OTMs. Generally, these two hurdles are essentially rooted in slow oxygen transport (including bulk diffusion and surface exchange kinetics) and insufficient phase/chemical/mechanical stability of the materials, respectively. Although the high operating temperature activates the oxygen permeation process, it undoubtedly gives rise to exceptional issues, for instance the excessive heat in the exhaust gas. Up to now, there are two basic categories of prevailing OTM materials: single-phase and dual-phase materials. Nevertheless, single-phase materials seldomly fulfill all the requirements for diverse applications. Accordingly, dual-phase composite materials have been proposed by the combination of a predominantly ionic conducting material and a predominantly electronic conducting material. However, a systematic narrative of the dual-phase OTM technology with a relatively in-depth analysis is still very lacking. The present thesis is intended to fill this gap to some degree and provide a fundamental understanding of dual-phase OTMs for researchers and engineers in both academia and industry.

Four research articles in which I have been the first author as well as one of the corresponding authors are involved in this thesis. All the presented results of this thesis were obtained during my Ph.D. study at the Institute of Physical Chemistry and Electrochemistry, Leibniz University Hannover, under the supervision of Prof. Dr. Armin Feldhoff. The following statement will clearly point out my contribution to these articles.

The first article, *A mixed ionic and electronic conducting dual-phase membrane with high oxygen permeability*, makes section 2.2. I wrote the draft manuscript and revised it in close dialogue with Prof. Dr. A. Feldhoff. I conceived, designed and conducted the experiments including membrane preparation and oxygen permeation measurements. Besides, I performed the characterization of X-ray diffraction (XRD) and analyzed the XRD refinement data. Moreover, the characterizations of scanning electron microscopy (SEM) and energy-dispersive X-ray spectroscopy (EDXS) were accomplished by F. Steinbach and me together. Transmission electron microscopy (TEM) and electron energy-loss spectroscopy (EELS) characterizations were supported by Prof. Dr. A. Feldhoff. In addition, Prof. Dr. F. Y. Liang and Dr. Z. W. Cao gave many valuable suggestions on the manuscript preparation.

The second article, *An approach to enhance the CO₂ tolerance of fluorite-perovskite dual-phase oxygen-transporting membrane*, makes section 2.3. I wrote the draft of this article and received support for manuscript preparation from Prof. Dr. A. Feldhoff and Prof. Dr. C. S. Chen. I proposed the primary ideas and carried out the experiments of membrane preparation and oxygen permeation. Furthermore, I conducted the XRD measurements and interpreted the data myself. The SEM and EDXS characterizations were performed by F. Steinbach and me. Additionally, Prof. Dr. A. Feldhoff supported the TEM and EELS characterizations.

The third article, *A highly efficient sandwich-like symmetrical dual-phase oxygen-transporting membrane reactor for hydrogen production by water splitting*, makes section 3.2. I wrote the draft of the manuscript and revised it with the help from Prof. Dr. A. Feldhoff and Prof. Dr. X. F. Zhu. I put forward the original innovations for the experiments and Prof. Dr. X. F. Zhu gave helpful advice on the optimization. The sandwich-like symmetrical OTMs were provided by Z. W. Cao from the Dalian Institute of Chemical Physics, Chinese Academy of Science. Moreover, I conducted XRD measurements and related analysis. The SEM-EDXS characterizations were done by F. Steinbach together with me.

The fourth article, *A method of stabilizing perovskite structure via interdiffusional tailoring and its application in an oxygen-transporting membrane reactor*, makes section 3.3. I wrote the draft paper and Prof. Dr. A. Feldhoff devoted to perfecting it. The basic thought and the corresponding experiments (for example preparation, measurements and analysis) were almost implemented by myself. Besides, F. Steinbach aided me with the SEM-EDXS characterizations. The electron probe micro-analysis (EPMA) measurements were performed by Dr. C. Zhang.

Putting it all together, dual-phase OTMs have been widely investigated, which will provide a guide for the materials design and membrane fabrication. Finally, it is the authors' sincere hope that this thesis can be meaningful to the development and industrialization of the OTM technology.

Wei Fang

September, 2016

Acknowledgement

This thesis has been financially supported by the German Research Foundation (DFG; no. FE928/7-1). All the work was supervised by Prof. Dr. Armin Feldhoff, at the Institute of Physical Chemistry and Electrochemistry, Leibniz University Hannover.

First of all, I would like to thank my supervisor Prof. Dr. Armin Feldhoff for giving me the opportunity to study and conduct this attractive and interesting scientific research in his group. I greatly appreciate for his very fruitful support and extremely patient guidance during my Ph.D. study. Specially, I am deeply impressed by his precise attitude and enormous dedication to science. Moreover, I feel fortunate to benefit from his rich experience in scientific activities.

Besides, I am very grateful to Prof. Dr. Chusheng Chen from School of Chemistry and Materials Science at University of Science and Technology of China and Prof. Dr. Xuefeng Zhu from Dalian Institute of Chemical Physics at Chinese Academy of Sciences, for their valuable cooperation and brilliant wisdom on my research topics.

Furthermore, I would thank Prof. Dr. Jürgen Caro, Prof. Dr. Heqing Jiang, Prof. Dr. Jianxi Yi and Prof. Dr. Yanying Wei for their meaningful discussions and comments on my research work. Special thanks to Prof. Dr. Yi Liu and Prof. Dr. Fangyi Liang for their tremendous help at the beginning of my Ph.D. career. Exceptional acknowledgement is given to Frank Steinbach for his wonderful cooperation on the characterization of materials.

Additionally, I feel grateful to Dr. Nanyi Wang, Dr. Chao Zhang, M.Sc. Alexander Wollbrink, Dr. Andre Düvel, Dr. Kaveh Partovi, M.Sc. Benjamin Geppert, Dr. Jian Xue, Dr. Zhengwen Cao and M.Sc. Wenyuan Liang for their helpful assistance in the past three years. I also would like to express my thanks to Yvonne Gabbey-Uebe and Kerstin Janze for their excellent support in the administrative or laboratorial aspects. I kindly appreciate the nice job done by the mechanical and electrical workshop as well. Many thanks to all the people who have aided and encouraged me during my daily life in Germany.

Finally, I want to express my deepest appreciation to my parents for their unconditional understanding, unlimited support, infinite love and inspiring encouragement. Therefore, this dissertation is dedicated to my dearest mother on the occasion of her upcoming birthday.

Abstract

Dual-phase oxygen-transporting membranes (OTMs) comprising of a predominantly ionic conducting (IC) conductor and a predominantly electronic conducting (EC) conductor, hold great potential for applications in high-purity oxygen production, oxy-fuel combustion integrated with CO₂ capture and catalytic membrane reactors. However, the unsatisfactory oxygen permeability and/or insufficient phase/chemical stability of OTMs, especially under harsh operating conditions (such as intermediate temperatures, CO₂-rich or reducing atmospheres), as well as the frequent catalyst deactivation are the most crucial issues for industrialization.

Chapter one gives an overview of the research and development efforts on OTM technology, including its basic fundamentals, effective functional components, state-of-the-art materials, history, advantages, potential markets and leading fabrication techniques.

In chapter two, in order to obtain a well-balanced performance between permeability and stability, a novel concept for dual-phase OTM consisting of two separate mixed ionic and electronic conducting (MIEC) materials has been firstly proposed. Based on this strategy, a MIEC-MIEC composite dual-phase membrane was favorably fabricated. Good oxygen permeability and excellent stability even in the presence of CO₂-rich atmosphere were achieved. Afterwards, the mechanisms of CO₂ tolerance in alkaline-earth containing OTMs have been systematically summarized and further developed. Furthermore, it is clearly pointed out that the chemical potential of oxygen can significantly affect the CO₂ tolerance of the membrane materials. Moreover, it is also confirmed that the competitive effect between oxygen desorption and CO₂ absorption occurs during the oxygen permeation process. In other words, oxygen molecules could act as an effective “protector” to inhibit the CO₂ absorption as well as carbonate formation.

In chapter three, first of all a Ni-infiltrated sandwich-like symmetrical dual-phase OTM reactor has been developed for hydrogen production by water splitting combined with partial oxidation of methane (POM). Moreover, it is demonstrated that a novel approach based on simple valve switching can effectively in-situ regenerate the deactivated catalyst by water steam in a single unit, which greatly contributes to the intensification of chemical processes. Subsequently, the universal interdiffusional behaviors in the fluorite-perovskite dual-phase OTMs have been carefully investigated. Accordingly, a new method has been put forward to stabilize perovskite structure via interdiffusional tailoring. Consequently, the stabilized dual-phase membrane exhibited excellent performance for diverse applications (for example, POM membrane reactor). This findings open up a door to overcome the drawbacks in phase stability for perovskites.

Keywords: oxygen transport • dual-phase materials • CO₂ tolerance • membrane reactors

Zusammenfassung

Zweiphasige keramische Sauerstofftransportmembranen (OTM), bestehend aus einem vorwiegend sauerstoff-ionischen Leiter (IC) und einem vorwiegend elektronischen Leiter (EC) haben ein großes Anwendungspotenzial in der Herstellung von Reinstsauerstoff, Oxy-Fuel-Verbrennungsprozessen mit CO₂-Rückhaltung sowie katalytischen Membranreaktoren. Allerdings stellen eine ungenügende Sauerstoffpermeabilität sowie ungenügende Phasenstabilität oder chemische Stabilität der Membranen, besonders unter harten Einsatzbedingungen (wie mittlere Temperaturen, CO₂-reiche oder reduzierende Atmosphären) und die rasche Deaktivierung von Katalysatoren die größten Hürden für eine industrielle Nutzung derartiger Membranreaktoren dar.

Kapitel 1 gibt einen Überblick über den aktuellen Stand der Forschung und Entwicklung der OTM-Technologie, wobei Grundlagen, wesentliche funktionelle Komponenten, den Stand der Technik prägende Materialien, historische Aspekte, Vorteile gegenüber anderen Technologien, aussichtsreiche Anwendungsfelder und etablierte Herstellverfahren diskutiert werden.

In Kapitel 2 wird, erstmals ein Konzept für eine zweiphasige keramische OTM vorgestellt, welches zwei separierte Phasen mit gemischter sauerstoff-ionischer und elektronischer Leitfähigkeit (MIEC) beinhaltet und einen gut ausbalancierten Kompromiss zwischen Sauerstoffpermeabilität und Stabilität darstellt. Dazu wurde eine zweiphasige MIEC-MIEC-Kompositmembran hergestellt und funktionell sowie mikrostrukturell charakterisiert. Diese Membran weist eine gute Sauerstoffpermeabilität und herausragende Stabilität, sogar in CO₂-reicher Atmosphäre, auf. Weiterhin werden Mechanismen, die CO₂-Toleranz von erdalkali-haltigen OTM betreffend, diskutiert und es wird gezeigt, dass das lokale chemische Potenzial des Sauerstoffs in vorteilhafter Weise zur Stabilisierung eingestellt werden kann, da die Sauerstoffdesorption und die CO₂-Adsorption an der Membranoberfläche konkurrierende Prozesse sind. Sauerstoffmoleküle schützen die Membranoberfläche als effiziente für CO₂-Adsorption und damit vor der Bildung einer impermeablen Carbonatschicht.

In Kapitel 3 wird eine neuartige Ni-infiltrierte sandwich-artige symmetrische zweiphasige OTM in einem Membranreaktor eingesetzt, der die Wasserstoffherstellung aus Wasserspaltung mit der Partialoxidation von Methan (POM) zu Synthesgas kombiniert. Es wird gezeigt, dass ein innovativer Ansatz, welcher auf dem einfachen Schalten von Gasventilen beruht, effizient zur In-Situ-Regenerierung eines deaktivierten Katalysators unter Nutzung von Wasserdampf in der kompakten Anlage genutzt werden kann. Damit wird ein bedeutender Beitrag zur industriellen Prozessintensivierung gegeben. Weiterhin wird ein Interdiffusionsansatz in einem Fluorit-Perowskit-Oxidsystem vorgestellt, der zur Stabilisierung der Perowskitphase in einer zweiphasigen OTM genutzt wurde. Dabei wird genutzt, dass Kationen des fluoritartigen Oxids partiell in den Perowskiten eingebaut werden und seine vorteilhafte kubische Struktur merklich stabilisieren. Eine solche zweiphasige OTM mit stabilisierter Perowskitphase vermeidet viele der bisherigen Nachteile von perowskit-basierten OTM und erweitert deren Anwendungsspektrum (z.B. Membranreaktoren für POM).

Schlüsselwörter: Sauerstofftransport • Zweiphasige Materialien • CO₂-Toleranz • Membranreaktoren

Abbreviations

BSE	Back-scattered electron
CCS	CO ₂ capture and storage
EC	Electronic conducting
EDTA	Ethylenediaminetetraacetic acid
EDXS	Energy-dispersive X-ray spectroscopy
EELS	Electron energy-loss spectroscopy
EPMA	Electron probe micro-analysis
IC	Ionic conducting
MIEC	Mixed ionic and electronic conducting
OTMs	Oxygen-transporting membranes
OSER	Oxygen surface exchange reaction
POM	Partial oxidation of methane
SE	Secondary electron
SOFC	Solid oxide fuel cell
SRM	Steam reforming of methane
TEC	Thermal expansion coefficient
TEM	Transmission electron microscopy
TPB	Triple phase boundary
WDS	Wave-length dispersive spectroscopy
WGS	Water gas shift
XRD	X-ray diffraction
D	Chemical bulk diffusion coefficient
δ	Oxygen non-stoichiometry

F	Faraday constant
h	Electron hole
J_{O_2}	Oxygen permeation flux
k	Chemical surface exchange coefficient
$\mu_{O_2}^o$	Standard oxygen chemical potential
μ'_{O_2}	Oxygen chemical potential at the feed side
μ''_{O_2}	Oxygen chemical potential at the sweep side
O_O^\times	Lattice oxygen
$p_{O_2}^o$	Standard oxygen partial pressure
p'_{O_2}	Oxygen partial pressure at the feed side
p''_{O_2}	Oxygen partial pressure at the sweep side
R	Gas constant
r	Ionic radius
σ_e	Electronic conductivity
σ_i	Oxygen-ionic conductivity
T	Temperature
t	Tolerance factor
$V_O^{\ddot{\cdot}}$	Oxygen vacancy
CGO	$Ce_{1-x}Gd_xO_{2-\delta}$
CGCO	$Ce_{0.85}Gd_{0.1}Cu_{0.05}O_{2-\delta}$
LCF	$La_{0.6}Ca_{0.4}FeO_{3-\delta}$
SDC	$Ce_{0.85}Sm_{0.15}O_{1.925}$
SFO	$SrFeO_{3-\delta}$
SSAF	$Sm_{0.6}Sr_{0.4}Al_{0.3}Fe_{0.7}O_{3-\delta}$

Content

Preface	I
Acknowledgement	III
Abstract	V
Zusammenfassung	VI
Abbreviations	VII
Content	IX
1 Introduction	1
1.1 Motivation.....	1
1.2 Fundamentals	1
1.3 Materials	4
1.3.1 Single-phase perovskites.....	4
1.3.2 Single-phase fluorites.....	5
1.3.3 Dual-phase composites	9
1.4 Fabrication	12
1.4.1 Planar membranes	12
1.4.2 Hollow fibers	13
1.5 Application.....	14
1.5.1 Oxygen production.....	14
1.5.2 Oxy-fuel combustion	15
1.5.3 Partial oxidation of methane	17
1.6 Bibliography	20

2	Investigation of CO₂-tolerant dual-phase oxygen-transporting membranes for oxy-fuel combustion.....	29
2.1	Summary	29
2.2	A mixed ionic and electronic conducting dual-phase membrane with high oxygen permeability	30
2.3	An approach to enhance the CO ₂ tolerance of fluorite-perovskite dual-phase oxygen-transporting membrane	55
3	Development of dual-phase membrane reactors for hydrogen and syngas production.....	75
3.1	Summary	75
3.2	A highly efficient sandwich-like symmetrical dual-phase oxygen-transporting membrane reactor for hydrogen production by water splitting	76
3.3	A method of stabilizing perovskite structure via interdiffusional tailoring and its application in an oxygen-transporting membrane reactor	90
	Publications and conferences.....	105
	Curriculum Vitae	106

1 Introduction

1.1 Motivation

The increasing demand for primary energy has extremely attracted attention in order to keep pace with the world's rapidly growing economy. Meanwhile, energy security and climate change issues have led to a globally diversified energy development trend, particularly focused on power production from renewable sources such as wind, solar, nuclear or biofuels.^[1] Up to now, renewable energy still cannot cope with fluctuations in power demand. Thus far, fossil fuels (oil, coal and natural gas) are extensively utilized in most conventional, combustion-based power generation systems.^[2] Therefore, it is urgent to explore the most efficient and cost-effective way to make full use of fossil fuels.

Nevertheless, the problem with the continuing use of fossil fuels is that it has a high CO₂ emission, resulting in the significant increased global atmospheric CO₂ concentration, thus raising serious concerns on its potential impact on environmental issues, for example climate change. Recently, CO₂ capture and storage (CCS) technologies as well as the utilization of CO₂ have gained great interest as a promising approach to reduce CO₂ emissions drastically.^[3] However, CCS must be economically competitive to be commercially viable.

It is also worth noting that oxygen can play a major role in the energy conversion process of fossil fuels. So far, numerous efforts have been devoted to the development of oxygen-transporting membranes (OTMs), which can produce pure oxygen by separation from air or other oxygen-containing gas mixtures.^[4] Compared with the cryogenic distillation or the pressure swing adsorption processes, OTMs consisting of mixed ionic and electronic conducting (MIEC) materials will be less cost and less energy consuming as well as more competitive, especially at small and intermediate scale level. Another important application of OTMs is to be found in the field of chemical processing, including oxy-fuel combustion integrated with the CCS process^[5] and the partial oxidation of light hydrocarbons, for example natural gas/methane to syngas.^[6]

This thesis addresses recent developments in the area of OTMs for oxygen separation and membrane reactors, in which the OTM materials have been fully investigated and discussed. Emphasis is on the understanding of effective factors for oxygen permeation and the coupling of chemical reactions for process intensification, providing some basic or novel knowledge which aids further improvements of OTMs for the aforementioned applications.

1.2 Fundamentals

The basic assumption of the theory presented in this section is that the diffusion of oxygen vacancies or the transport of electrons/electron holes through the bulk oxide

and the exchange of oxygen between oxide/gas interfaces determine the rate of the overall oxygen permeation under the driving force of a gradient in oxygen chemical potential.^[4] A more complete description is depicted in Figure 1.1.

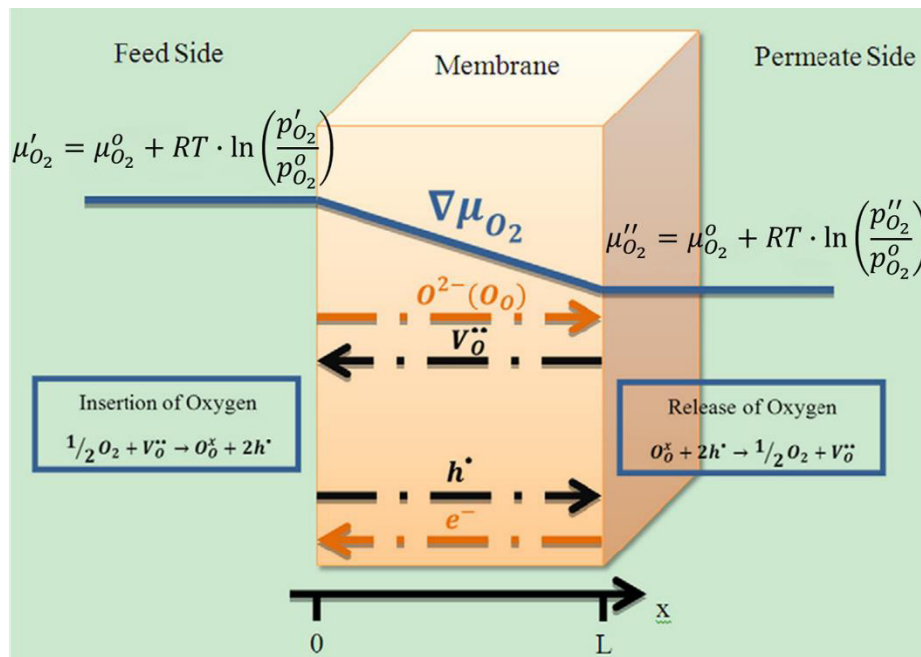


Figure 1.1 Schematic diagram of oxygen permeation through a MIEC membrane.^[7] Note that oxygen chemical potential μ_{O_2} , oxygen partial pressure p_{O_2} , temperature T , gas constant R , oxygen vacancy $V_o^{..}$, lattice oxygen O_o^x , electron hole $h^•$ and membrane thickness L .

Oxygen permeation through a dense MIEC material involves three progressive steps:^[4]

- (i) **the oxygen surface-exchange reaction (OSER) on the feed side**, and the possible process for the insertion of oxygen include adsorption, dissociation, charge transfer, surface diffusion and incorporation;
- (ii) **the simultaneous bulk diffusion of oxygen vacancies and electrons/electron holes in the oxide**, besides the flux of oxygen vacancies is charge compensated by the flux of electrons/electron holes;
- (iii) **the OSER on the sweep side**, and generally it is considered that the release of oxygen follows the same process in the reverse direction.

Moreover, for a dense ceramic MIEC membrane, the oxygen flux can be obviously increased by reducing the membrane thickness until its thickness becomes less than a characteristic value, at which the oxygen permeation is under mixed control of bulk diffusion and surface exchange kinetics.^[4] In the case that the bulk diffusion is rate-limiting, when the thickness of the membrane is relatively thick, the oxygen permeation flux J_{O_2} through an OTM can be described by the Wagner equation (see Equation 1.1):^[8]

$$J_{O_2} = - \frac{RT}{16F^2L} \cdot \int_{\ln p'_{O_2}}^{\ln p''_{O_2}} \frac{\sigma_i \cdot \sigma_{el}}{\sigma_i + \sigma_{el}} d \ln p_{O_2} \quad (\text{Equation 1.1})$$

where σ_i and σ_{el} are the oxygen-ionic and electronic (the sum of electrons and electron holes) conductivity respectively, and note that the oxygen partial pressure p_{O_2} , gas constant R , temperature T , Faraday constant F and membrane thickness L .

Additionally, if the ionic and electronic conductivities can be assumed as

$$\sigma_i = \text{const} \quad (\text{Equation 1.2})$$

$$\sigma_{el} = \sigma_{el_0} p_{O_2}^n \quad (\text{Equation 1.3})$$

the oxygen partial pressure at a given position x in the bulk of the OTM can be determined from the following equation:

$$\frac{x}{L} = \frac{\int_{\ln p'_{O_2}}^{\ln p_{O_2}(x)} \frac{p_{O_2}^n}{\sigma_i + \sigma_{el_0} p_{O_2}^n} d \ln p_{O_2}}{\int_{\ln p'_{O_2}}^{\ln p''_{O_2}} \frac{p_{O_2}^n}{\sigma_i + \sigma_{el_0} p_{O_2}^n} d \ln p_{O_2}} \quad (\text{Equation 1.4})$$

where p'_{O_2} and p''_{O_2} are the oxygen partial pressures at the feed and sweep side respectively, n is index number and σ_{el_0} is pre-exponential factor. Further detailed discussion is presented in Section 3 of this thesis.

Furthermore, it is generally accepted that the oxygen permeability of the materials is essentially controlled by two factors: chemical surface exchange coefficient k and chemical bulk diffusion coefficient D . Figure 1.2 shows the k and D values for a number of common pure phase materials, which gives some useful hints for the development of OTMs.

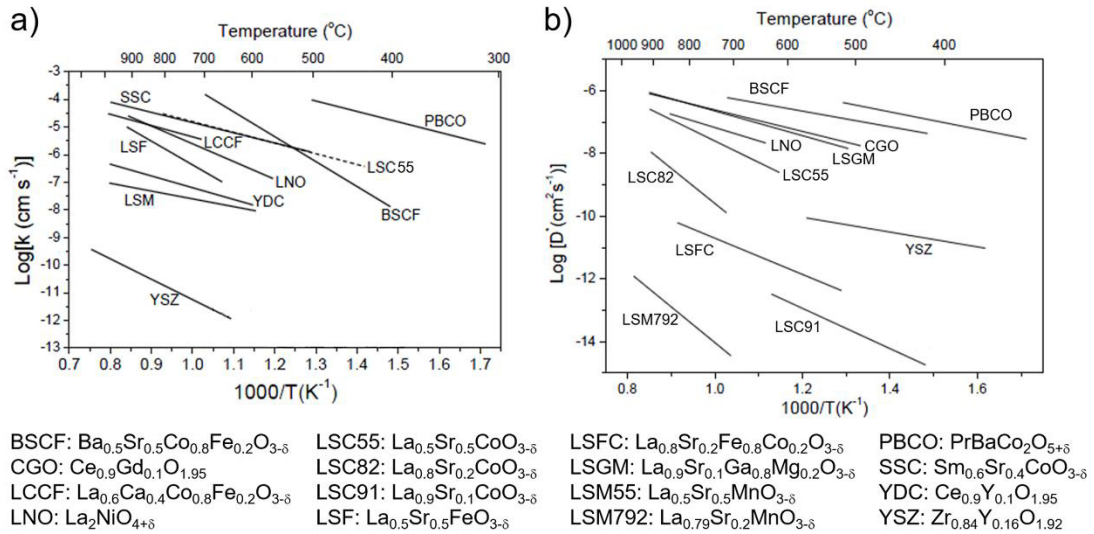


Figure 1.2 Temperature dependent values of a) chemical surface exchange coefficient k and b) chemical bulk diffusion coefficient D for some pure single-component materials.^[9-11]

1.3 Materials

Generally speaking, most of the well-established MIEC materials for OTMs can be divided into two basic categories: single-phase and dual-phase materials.^[4] There are several requirements for OTM materials in industrial applications: (i) high oxygen permeability; (ii) good chemical stability under various circumstances, such as CO₂-rich or reducing atmospheres; (iii) enough mechanical strength; (iv) low costs.

1.3.1 Single-phase perovskites

Perovskite oxides comprise of a large family of promising OTM materials because of the structural simplicity and flexibility, good phase stability under a certain temperature range and a wide range of oxygen nonstoichiometry. The general formula of perovskite oxides can be expressed as ABO₃, where the A cation is 12-fold coordinated and the B cation is 6-fold coordinated to the oxygen anions. In the typical ABO₃ structure, the A cation is usually an alkaline-earth or rare-earth metal element, while the B cation is normally a transition metal element. An ideal ABO₃ perovskite (Figure 1.3) displays a cubic symmetry with tolerance factor $t = 1$, which is defined as

$$t = \frac{r_A + r_O}{\sqrt{2}(r_B + r_O)} \quad (\text{Equation 1.5})$$

where r_A , r_B and r_O denote the ionic radii of A, B and oxygen ions, respectively.^[12]

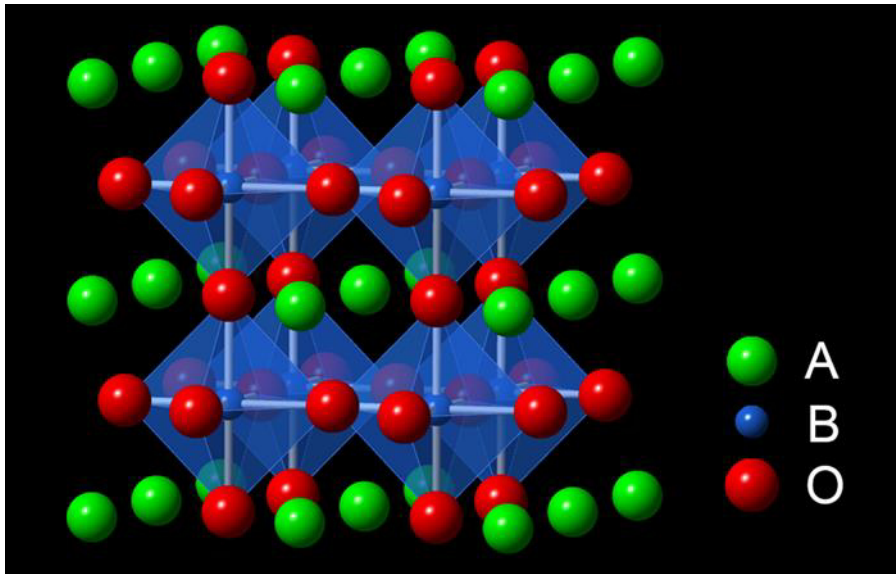


Figure 1.3 Crystal structure of the ideal cubic perovskite (space group $Pm\bar{3}m$). Atomic positions were calculated from ICSD #23076.

To compose a stable perovskite structure, it is normally regarded that t should lie between 0.75-1.0. Besides, a slightly distorted perovskite structure with orthorhombic or rhombohedral symmetry can be induced by a lower t value (< 1). Additionally, it is noticed that the cubic perovskite structure preferentially exists in the case where t is very close to 1 and often at high temperatures. Furthermore, either A or B site can be

partially substituted by other dopants, which extends the ABO_3 type perovskites into a broader family of $A_xA'_{1-x}B_yB'_{1-y}O_{3\pm\delta}$. The substitution of multiple cations into the A or B sites can change the symmetry of the crystal structure and thus alter the defect concentrations of the perovskites, which has a great influence on the ionic/electronic and catalytic properties as well as the oxygen permeation process.

As is now well known, the defect concentrations of perovskites can be controlled by doping with different valent cations. For instance, oxygen vacancies can be introduced by replacing B-site elements with cations of lower valence, forming the compounds of $AB_yB'_{1-y}O_{3-\delta}$, or by substitution of A-site ions with cations of lower valence, producing the compounds of $A_xA'_{1-x}BO_{3-\delta}$. In principle, A-site vacancies are much easier to be observed since the BO_3 octahedra in the perovskite structure forms a stable network, the large A cations at 12 coordinated sites can be partially missing. However, due to the small size and large charge of the B cations, B-site vacancies are not common because they are not thermodynamically stable.

With regard to OTMs, the first studies by Teraoka et al. were the series of $La_{1-x}Sr_xCo_{1-y}Fe_yO_{3-\delta}$ (LSCF) perovskite membranes, which proved that the oxygen fluxes increased with Co and Sr content and the highest flux being found for $SrCo_{0.8}Fe_{0.2}O_{3-\delta}$ (SCF) with, however, poor phase stability under relatively low p_{O_2} .^[13] In a subsequent study, it was found that a partial substitution of Sr^{2+} with the same valent but larger cation like Ba^{2+} could improve the phase stability under oxidizing conditions while keeping the oxygen flux at the same level, for instance, $Ba_{0.5}Sr_{0.5}Co_{0.8}Fe_{0.2}O_{3-\delta}$ (BSCF), a high-performance material for oxygen permeation.^[14] However, the cubic BSCF material decomposed gradually into a cobalt-rich (e.g. hexagonal $Ba_{0.5\pm 0.1}Sr_{0.5\pm 0.1}CoO_{3-\delta}$) and a cobalt-depleted phase at lower temperatures (e.g. below 850 °C), which impeded their commercial application.^[15] In order to improve the phase stability of these perovskites, high valent cations, for example Cr, Al, Zr, V, Ti or Nb were introduced into the Co or Fe lattice positions, nevertheless at the expense of oxygen permeability.^[16-20] To date, a considerable number of investigations have appeared, consequently the list of OTM materials has been tremendously extended, including $La_{0.6}A_{0.4}Co_{0.8}Fe_{0.2}O_{3-\delta}$ (A= Ba, Ca, Sr, La),^[21] $La_{0.6}Sr_{0.4}B_{0.2}Co_{0.8}O_{3-\delta}$ (B= Ni, Cu, Cr, Mn),^[21] $Ln_{0.3}Sr_{0.7}CoO_{3-\delta}$ (Ln= La, Nd, Sm, Gd),^[22] $Ba_{0.5}Sr_{0.5}X_{0.2}Fe_{0.8}O_{3-\delta}$ (X= Zn, Cu),^[23,24] $BaY_xFe_{1-x}O_{3-\delta}$ (Y= Ce, Zr),^[25,26] $Ba_{0.95}La_{0.05}FeO_{3-\delta}$,^[27] $La_{1-x}Sr_xGa_{1-y}Fe_yO_{3-\delta}$,^[28] $CaTi_{1-x}Fe_xO_{3-\delta}$.^[29]

Although the single-phase perovskites have a bright future for use as OTMs, the precise composition still need to be tailored to obtain good permeability as well as sufficient stability for the specific applications, since one of the most important issues for perovskites is their low structural, chemical and mechanical stability, particularly under harsh conditions such as CO_2 -rich, steam-containing or reducing (e.g. methane) atmospheres.^[30-31]

1.3.2 Single-phase fluorites

Alternatively, cubic fluorite-type oxides (Figure 1.4) are especially attractive due to a combination of fast oxygen-ion mobility and excellent chemical stability under

CO₂, steam or reducing conditions at elevated temperatures.^[32] However, a more possible application of these fluorite materials such as ZrO₂ and Bi₂O₃ is used as solid electrolyte in fuel cells, oxygen pumps or sensors, owing to their very low electronic conductivity.^[33] Further studies reveal mixed ionic-electronic conduction can occur under sufficiently low oxygen partial pressure, where electronic defects are generated for charge compensation of the excess of ionic defects (e.g. oxygen vacancies). It is demonstrated that the reduction of Ce⁴⁺ (at about $p_{O_2} = 10^{-10}$ atm, 1000 °C) is much easier than that of Zr⁴⁺ (below $p_{O_2} = 10^{-30}$ atm, 1000 °C).^[34,35] Hence, pure and doped ceria-based materials have been widely investigated as a potential candidate for OTMs.

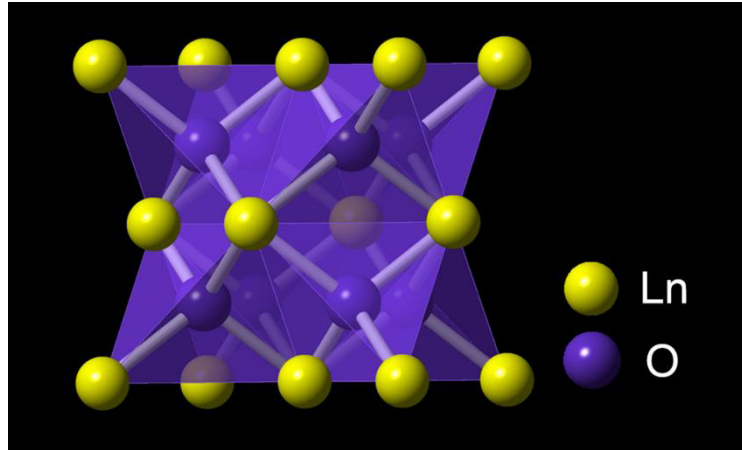
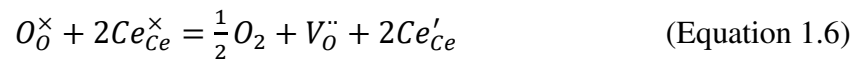
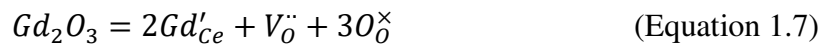


Figure 1.4 Crystal structure of the ideal cubic fluorite-type oxide (space group $Fm\bar{3}m$). Ln=lanthanide. Atomic positions were calculated from ICSD #28795.

Pure stoichiometric CeO₂ has a calcium fluorite type structure over the whole temperature range (from room temperature to the melting point). When CeO₂ is reduced to CeO_{2-δ}, defects are produced in the form of Ce'_{Ce} as the Ce³⁺ has one negative charge compared to the normal lattice. In the meantime, oxygen vacancies are formed as the main compensating defects, which can be expressed as



Besides, oxygen vacancies can also be introduced by doping with lower valent metal cations, for instance, by dissolution of Gd₂O₃ or CaO:



Assuming that no interaction between the various defects occurs (valid for very low concentrations), owing to the concentrations of Ce'_{Ce} and O_O^{\times} are also constant, an ideal relationship can be given:

$$[V_O^{\bullet\bullet}][Ce'_{Ce}]^2 p_{O_2}^{1/2} = \text{constant} \quad (\text{Equation 1.9})$$

For undoped ceria, $[Ce'_{Ce}] = 2[V_O^{\bullet\bullet}] = constant' p_{O_2}^{-1/6}$. In the case of doped ceria, since the concentration of oxygen vacancies can be regarded as a constant, the result becomes $[Ce'_{Ce}] = constant'' p_{O_2}^{-1/4}$.

It is now considered that the n-type conductivity of pure ceria takes place by the transport of small polaron (identified as Ce'_{Ce}).^[36] Therefore, the electronic conductivity σ_e can be described as

$$\sigma_e = [Ce'_{Ce}]e\mu \quad (\text{Equation 1.10})$$

where $[Ce'_{Ce}]$ is the concentration of Ce^{3+} cation, e is the charge of the electron and μ is the mobility. Moreover, the mobility has the form:

$$\mu = (B/T)\exp(-E_H/kT) \quad (\text{Equation 1.11})$$

Finally, rearranging gives

$$\sigma_e = (A/T)\exp(-E_H/kT) \quad (\text{Equation 1.12})$$

where E_H is the activation energy for the electron mobility as well as the electronic conductivity, and A or B is constant. More detailed explanations and discussions are given in reference [37], and further investigations show that the activation energy increases with increasing δ .^[36]

In addition, some researchers have also searched for the possible p-type conductivity in pure ceria. It is reported that p-type electronic conductivity can be obviously gained at high p_{O_2} (up to 400 atm) between 700 to 1100 °C.^[38] This conduction may be attributed to vacancies induced by lower valent impurities according to the reaction:



For doped ceria, oxygen vacancies are easily generated by acceptor dopants (such as Gd^{3+} or Sm^{3+}) compared to pure ceria, which leads to a shift of the n- and p- type regimes with respect to the p_{O_2} .^[39] It is worth noting that the ceria fluorite structure is very tolerant to dissolution of lower valent metal oxides. For instance, lanthanide oxides are highly soluble in ceria, about 40% or more.^[40] On the other hand, alkaline-earth oxides have a lower solubility even at high temperatures, such as the solubility of MgO is about 2%, SrO 9% and CaO 10% at 1600, 1600 and 1000 °C respectively.^[40,41] However, the solubility of transition metal oxides (e.g. CoO and NiO) are found to be very limited about 0.5%.^[42] Besides temperature, the solubility limit may be determined by the elastic energy, which indicates that the larger elastic energy per substituted ion, the lower solubility.^[43] In addition, the entropy of mixing of the solute into solution was deemed to be another factor by Mogensen et al.^[32]

Generally, the electronic conductivity of doped ceria in air is very low, therefore the total conductivity using classical four-point conductivity measurements is thought to be predominantly ionic, which can be further divided into bulk and grain boundary

contributions by means of alternating current (AC) impedance analysis.^[44] It is now agreed that Gd- or Sm-doped cerias exhibit the highest total conductivity in air.^[45] Figure 1.5 summarises the results of the total conductivity of doped cerias at 800 °C in air as a function of the ionic radius of the doped cation.^[45]

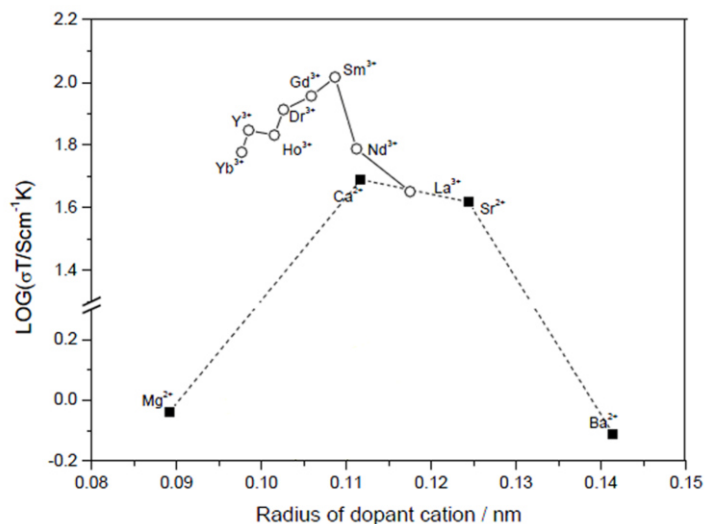


Figure 1.5 Dependency of the total conductivity σ for $(\text{CeO}_2)_{0.8}(\text{XO}_{1.5})_{0.2}$ at $T=1073$ K in air on the radius of dopant cations.^[45] X=Ln (lanthanide), Mg, Ca, Sr, Ba.

Besides, C. R. Xia et al. reported the maximum total conductivity was observed to be at a dopant concentration of $x=0.15$ at the temperature range of 400-850 °C for both Gd- and Sm-doped cerias ($\text{Ce}_{1-x}\text{Ln}_x\text{O}_{2-\delta}$), which is in agreement with the most common argument (x around 0.1-0.2).^[46] This is probably related to the interaction of defects, since the oxygen vacancies may react with the dopant cations to form associates (such as $[\text{Ln}_{\text{Ce}}\text{V}_\text{O}]^\cdot$), which increases the activation energy for bulk ionic conductivity especially at higher dopant concentrations.^[47]

On the other hand, it is believed that the segregation of the dopant ions may take the most possible responsibility for the grain boundary resistance, and in other words, the presence of relatively high-resistivity impurity along the grain boundaries causes an extra arc in the impedance spectra, which is prone to be seen especially at low temperature.^[35] However, the grain boundary resistance can be partially resolved by suitable dopants. For example, it was demonstrated that the grain boundary resistance of CaO-doped CeO_2 decreased with increasing dopant concentration from 0.6 to 11 mol%.^[48] Moreover, the enrichment of the calcia in the surroundings of the grain boundaries was also found for high dopant concentration.^[48] Additionally, except for the existence of foreign phases in the grain boundaries, grain size can play an important role as well. More specifically, for nanocrystalline (about 10 nm) Gd-doped CeO_2 , it was stated that grain boundary became much more resistive than the bulk;^[49] nevertheless, for the grain size of several microns or above, the contribution from the grain boundary to the total resistivity can be very low;^[50,51] furthermore, van Berkel et al. reported that a clear minimum in the grain boundary conductivity occurred at a grain

size of 3 μm for $\text{Ce}_{0.8}\text{Gd}_{0.2}\text{O}_{2-\delta}$ (CGO) ceramic over the temperature range 250-500 $^{\circ}\text{C}$.^[51]

Subsequently, studies of the total conductivity for $\text{Ce}_{0.8}\text{Sm}_{0.2}\text{O}_{2-\delta}$ as a function of oxygen partial pressure p_{O_2} at 673-1073 K have been carried out (see Figure 1.6).^[52] The dependence of the total conductivity on the p_{O_2} clearly showed that Ce^{4+} was partially reduced to Ce^{3+} , and obvious electronic conduction can be observed at relatively low p_{O_2} at elevated temperatures.

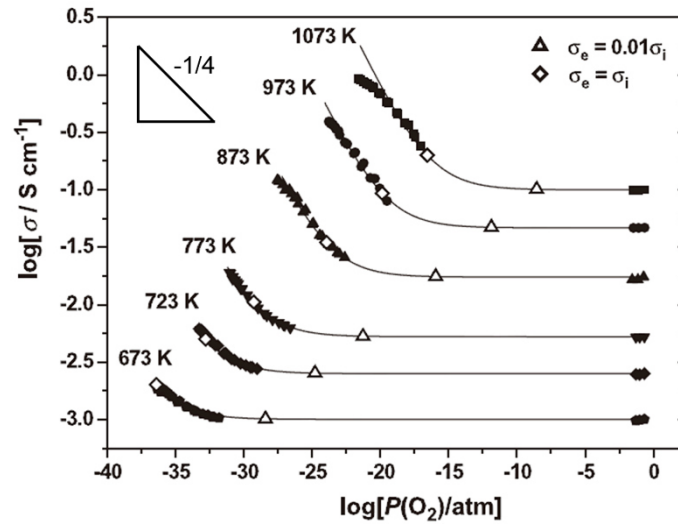


Figure 1.6 Dependency of the total conductivity σ , ionic conductivity σ_i and electronic conductivity σ_e of $\text{Ce}_{0.8}\text{Sm}_{0.2}\text{O}_{2-\delta}$ on the oxygen partial pressure.^[52]

Recently, a large number of doped cerias have been employed as a promising candidate for oxygen permeation membranes, owing to their excellent chemical stability against CO_2 , H_2O steam as well as reducing gases.^[53] It is generally agreed that oxygen vacancies will be produced by doping lanthanide like Gd^{3+} , Sm^{3+} and Nd^{3+} . Nevertheless these dopants do not change the band gap, thus a co-doping strategy is quite necessary.^[39] Normally, a further dopant is used to reduce the band gap by producing an additional density of electronic states near the Fermi level.^[54] In short, doping ceria with multivalent cations may allow the extension of the mixed conduction for cerias to higher p_{O_2} .^[39] Until now, only several works have focused on these dopants. Fagg et al. confirmed an increase of hole transport in the p-region for CGO doped with 2% Pr.^[55] Furthermore, they also pointed out the p-type conduction in 2% cobalt-doped CGO would be about 25 times higher than that in pure CGO.^[56] Note that the electronic conductivity was measured by the Hebb-Wagner polarization technique with ion-blocking microcontacts.^[39] Consequently, Serra et al. fabricated supported thin film membranes of CGO+2%Co, which exhibited practical oxygen permeability under CO_2 or methane containing atmospheres,^[57] but the oxygen permeation may still be limited by insufficient electronic conductivity.

1.3.3 Dual-phase composites

In order to obtain a good performance of OTM, the material should have both high

enough ionic conductivity and electronic conductivity in the appropriate range of temperature and oxygen partial pressure. Usually, it is found very difficult to realize all the requirements in one single-component material. Therefore, dual-phase composite membranes have been developed by the combination of ionic conducting (IC) materials and electronic conducting (EC) materials.^[4]

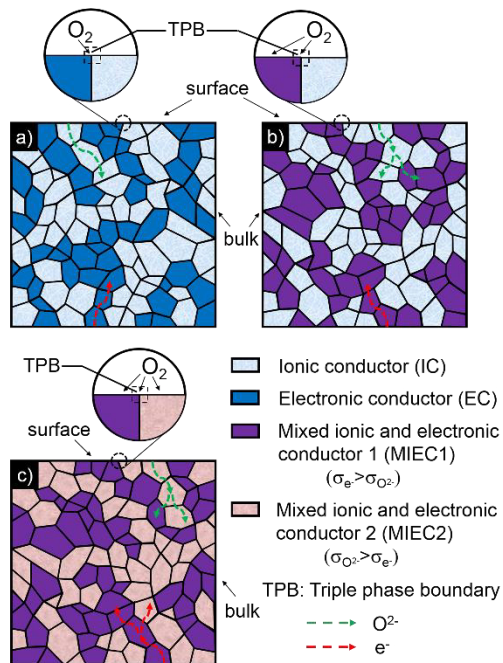


Figure 1.7 Schematic diagrams of concepts for the dual-phase membranes. a) IC-EC, b) IC-MIEC1 and c) MIEC1-MIEC2.^[63]

The pioneering work by C. S. Chen et al. reported a 2.0 mm thick percolative composite membrane consisting of 40 vol.% Pd-60 vol.% $Zr_{0.84}Y_{0.16}O_{1.92}$ (YSZ) exhibited an obvious oxygen permeability under air/He gradient at 1100 °C.^[58] In the subsequent studies, doped cerias were widely used in dual-phase composites mainly because of their higher ionic conductivity compared to YSZ at the elevated temperatures.^[59] At the same time, the noble metal phase was replaced by low cost pure EC perovskite oxides, for example $La_{0.7}Sr_{0.3}MnO_{3-\delta}$ (LSM) by Kharton et al., to achieve better compatibility between two phases,^[60] while the oxygen surface exchange reaction (OSER) is still only confined at the triple phase boundary (TPB).^[61] Afterwards, tremendous efforts have been devoted to the introduction of predominantly electronic MIEC perovskites such as $La_{0.8}Sr_{0.2}Fe_{0.8}Co_{0.2}O_{3-\delta}$ (LSCF) into dual-phase composites for both oxygen ionic and electronic transport,^[62] thereby OSER could take place not only at the TPBs but also at the surface of MIEC oxides.^[61] Very recently, another exciting option that has been explored for the development of dual-phase OTM is to replace the pure IC phase by predominantly ionic MIEC fluorite (e.g. copper-doped CGO).^[63] To sum up, the dual-phase membranes can be basically classified into three types: IC-EC, IC-MIEC and MIEC-MIEC composites (Figure 1.7).^[63] More detailed description can be found in Section 2 of this thesis.

As far as concerned, there are several factors that significantly affect the oxygen permeability of dual-phase composite membranes.

- (i) **Percolation.** Theoretically, the critical volume fraction of both phases to form a continuous percolative network could have a great influence on the oxygen permeation. Early studies demonstrated that the percolation threshold for the volume fraction of Pd in a Pd-YSZ composite was 40 vol.%.^[58] For the OTMs, the electronic conductivity is normally 10 times or more higher than the ionic conductivity,^[4] thus the oxygen permeation flux can be expected purely on the basis of IC phase. Following this idea, Joo et al. developed a high-performance fluorite (IC phase)-rich 80 vol.% CGO-20 vol.% LSCF dual-phase membrane, and showed that the percolation threshold of the composites for necessary electronic conduction can be reduced to 20 vol.%, which was predicted from the percolation theory for the total conductivity behavior.^[64]
- (ii) **Microstructure.** For actual composite dual-phase membranes, the interconnectivity between grains cannot be ideal and it is much easier to form “dead-ends” in the percolative system. Hence, the grain size as well as the distributions of both phases will be closely related to the oxygen permeability. Accordingly, X. F. Zhu et al. investigated the effects of sintering temperature on the oxygen permeability for dual-phase membranes, and concluded that the grain growth with increasing the temperature degraded the homogeneity of the phase distribution. This might even lead to phase segregation at high temperatures,^[65] which probably enhanced the tortuosity of the migrating path for oxygen ions/electrons, followed by a decrease in oxygen fluxes. Moreover, H. X. Luo et al. studied the influence of fabrication methods for dual-phase membranes on the oxygen permeability, and pointed out that compared to the powder-mixing membrane, the one-pot membrane with fine grains revealed higher oxygen fluxes due to the uniform distribution of two phases.^[66] Nevertheless, it was also reported that a less homogeneous membrane prepared by using solid state reaction method displayed a better performance than a more homogeneous membrane via ethylenediaminetetraacetic acid (EDTA) citrate complex method.^[67] To some extent, these contradictory results can be ascribed to the different rate-limiting steps. Specifically, the homogeneous distribution of two phases with smaller grains will contribute to a high TPB density on the membrane surface, which accelerates the OSER process; on the contrary, the doped cerias with larger grains may result in a decrease in the grain boundary resistance, which benefits the bulk diffusion for oxygen-ionic transport.
- (iii) **Interdiffusion.** With respect to dual-phase composites, it is commonly regarded that the interdiffusion between two phases (e.g. fluorite and perovskite) often occurs during the sintering process, resulting in an interfacial barrier. L. Hong et al. confirmed that an additional phase

consisting of BaCeO_3 was detected at the grain boundaries of $\text{Ce}_{0.8}\text{Gd}_{0.2}\text{O}_{2-\delta}$ - $\text{La}_{0.4}\text{Ba}_{0.6}\text{Fe}_{0.8}\text{Zn}_{0.2}\text{O}_{3-\delta}$ dual-phase membrane,^[68] and the existence of such impurity with low ionic conductivity may be detrimental to the oxygen ionic transport. Although scientists in this field have realized the importance of interdiffusion behavior, much effort is still based on trial and incorrect at present. Recently, a popular one-pot method has been widely applied into the development of dual-phase membranes.^[69] It was noticed that the membranes prepared by one-pot method exhibited a more homogeneous distribution of two phases as well as possessed a more serious interdiffusion during the powder synthesis process. Latest studies by W. Fang and A. Feldhoff et al. demonstrated that the obvious interdiffusion zone of lanthanide cations between fluorite and perovskite phase varied greatly from tens of nanometers (e.g. La in $\text{La}_{0.6}\text{Ca}_{0.4}\text{FeO}_{3-\delta}$ extended to $\text{Ce}_{0.85}\text{Gd}_{0.1}\text{Cu}_{0.05}\text{O}_{2-\delta}$) to the whole range (e.g. Gd in both $\text{CeO}_{2-\delta}$ and $\text{SrFeO}_{3-\delta}$ lattices).^[63,70] Furthermore, these interdiffusions may change the chemical composition of two phases, and alter the concentration of oxygen vacancies in both phases, even lead to the phenomena of phase transformation. In addition, it was also reported that the impurity with electronic conductivity segregated at the grain boundaries between two ionic conducting grains could extend the density of TPBs for OSER process, thus improving the oxygen permeability of dual-phase membranes.^[63]

In conclusion, dual-phase composite membranes are considered to be the most competitive OTMs mostly because of their capacity to meet the various requirements under diverse conditions. Therefore, a systematic evaluation (such as permeability, compatibility and stability) of dual-phase membranes is very urgent, which is also the aim of this thesis.

1.4 Fabrication

To date, great efforts have been made to improve the oxygen permeability by designing thin membranes in order to reduce the bulk diffusion resistance for oxygen permeation.^[4] Currently, most of the state-of-art asymmetric OTMs can be divided into two categories, planar membranes and hollow fibers.

1.4.1 Planar membranes

For supported planar membranes, it is necessary to fabricate the ultra-thin dense oxygen functional layer on a porous MIEC substrate for enhancing not only the mechanical strength but also the surface oxygen exchange kinetics. So far, tape-casting was demonstrated to be the simplest and most effective method for preparing planar thin membranes with increased oxygen permeability.^[71] It was shown by Baumann et al. that a self-supported BSCF asymmetric membrane by using multilayer tape casting and co-sintering method exhibited a very high oxygen flux of $12.2 \text{ mL min}^{-1} \text{ cm}^{-2}$ at $1000 \text{ }^\circ\text{C}$ under air/Ar gradient.^[71] The BSCF asymmetric membrane comprised of a gas-tight layer with $70 \text{ }\mu\text{m}$ thickness and a porous support layer (34% open porosity, corn

starch as pore former) with 830 μm thickness. Besides, a porous surface activation layer on the air side was introduced to the asymmetric membrane by screen printing,^[72] which further accelerated the oxygen surface exchange reaction for oxygen permeation. Very recently, a modified tape-casting combined with co-lamination method was applied into the fabrication of a sandwich-like dual-phase membrane,^[73] which provided a more convenient way to tailor the OTMs with multilayer structure.

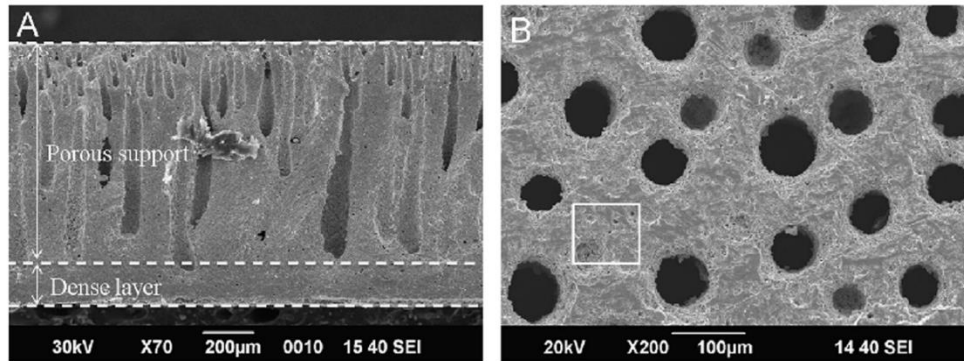


Figure 1.8 Cross-sectional microstructure of the YSZ-LSM dual-phase membranes by phase-inversion tape-casting technique. a) Overview and b) section of the support perpendicular to the thickness direction.^[74]

Moreover, it is worth to be noticed that the phase-inversion tape-casting method has been successfully put forward in order to enable the fabrication of asymmetric membranes in one single step.^[74] In the process, a slurry made of ceramic powders in an organic polymer solution is firstly cast on a temporary substrate (e.g. a glass plate), then transferred into a water bath for solidification. In the water bath the organic polymer solution can easily separate into a polymer-rich and a polymer-lean phase respectively due to the exchange between organic solvent and water. Subsequently, the polymer-rich phase can be solidified into a green tape, meanwhile the polymer-lean phase can be removed after a drying step, resulting in large finger-like pores left in the green tape. Since the phase inversion process proceeds from the slurry-water interface into the bulk, the as-prepared green tape has a two-layer structure: a thick finger-like pores layer and a thin sponge layer with very fine pores. This special asymmetric structure will be preserved even after heat treatment at high temperature. Consequently, the thick layer with large pores provides the membrane with low gas diffusion resistance and sufficient mechanical strength, while the thin layer could be gas-tight after sintering, thus can function as the separation layer. Recently, C. S. Chen et al. developed an asymmetric dual-phase membrane with the composition of YSZ-LSM via phase-inversion tape casting method (see Figure 1.8),^[74] which made a great progress in the construction of planar membranes.

1.4.2 Hollow fibers

Alternatively, hollow fiber via phase inversion technology for OTMs has attracted great attention in the past few years, because the hollow fiber has a small diameter of

1-2 mm, leading to a high surface to volume ratio.^[75] Thus far, a number of single-phase perovskite membranes such as $\text{BaCo}_x\text{Zr}_y\text{Fe}_z\text{O}_{3-\delta}$ ($x+y+z=1.0$)^[76] as well as dual-phase fluorite-perovskite composite membranes including YSZ-LSM^[75] and $\text{Ce}_{0.8}\text{Sm}_{0.2}\text{O}_{1.9}\text{-La}_{0.8}\text{Sr}_{0.2}\text{Cr}_{0.5}\text{Fe}_{0.5}\text{O}_{3-\delta}$ ^[77] have been prepared into the hollow-fiber geometry. Moreover, K. Li et al. systematically investigated the dominating factors (e.g. suspension viscosity, air-gap and non-solvent concentration) that influenced the morphologies of ceramic hollow-fiber membranes.^[78] Recently, a highly compact dual-layer ceramic hollow-fiber OTM was prepared by using a single-step co-extrusion and co-sintering technique (see Figure 1.9),^[79] which displayed an interesting approach to tailor the composition and structure of hollow fiber. Additionally, a BSCF U-shaped hollow-fiber membrane was reported to avoid the breakage of the membrane owing to the mismatch of shrinkage and expansion between the hollow fiber and sealant.^[80]

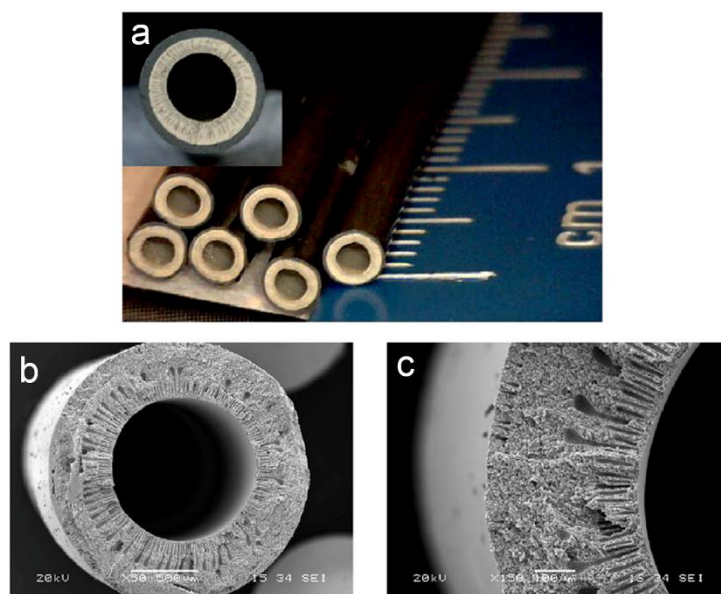


Figure 1.9 Images of the precursor YSZ-LSM/NiO-YSZ dual-layer hollow fibers. a) Photograph. Secondary electron micrographs of b) whole view and c) cross-section.^[79]

1.5 Application

So far, the potential applications for OTMs can be summarized as oxygen supply, CO_2 capture combined with oxy-fuel combustion and chemical membrane reactors.^[4,63,73] Accordingly, numerous efforts have been made to balance the good oxygen permeability and sufficient stability of OTMs in order to meet the requirements of industrialization. And it is necessary to understand the factors that affect and control the quality criteria for any given applications.

1.5.1 Oxygen production

Nowadays, oxygen is considered as one of the largest industrial chemicals by volume in the world, and three-quarters of the produced oxygen are used for the production of primary metals and chemicals. Currently, oxygen is mostly produced by

the cryogenic distillation process which is very capital and energy-intensive. Furthermore, pure oxygen also can be separated from air by using high-temperature OTM technology, which facilitates an expected and significant turndown of 30% total costs.^[81]

Generally speaking, upon exposure to an oxygen partial pressure p_{O_2} gradient, oxygen molecules can be transported through the OTM from the high p_{O_2} side to the low p_{O_2} side. Moreover, the permselectivity of oxygen is unrivaled in principal. Usually, in order to evaluate the oxygen permeability of OTMs, inert gas (e.g. He) with much lower p_{O_2} is used as the sweep gas, while air as the feed gas. However, this method is only limited into the laboratory studies, which can be ascribed to the need for a subsequent separation of the oxygen/sweep gas mixture. Hence, for industrial application, the compressed air and vacuum will be applied on the feed and permeate side respectively.

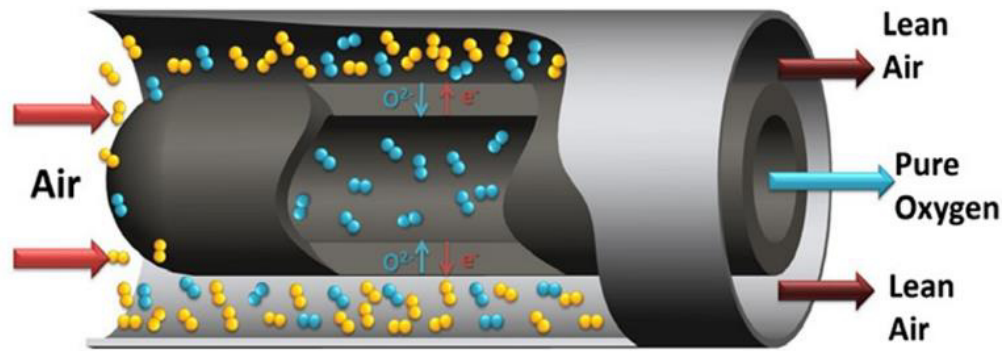


Figure 1.10 Pure oxygen production through a one end-dead tube membrane by vacuum.^[7]

Recently, a two-step operation method for pure oxygen production has been proposed to improve the permeated oxygen space-time yields.^[7,82] Firstly, the oxygen-enriched air (> 50 vol% O₂) will be produced from air through the OTM by decreasing the p_{O_2} on the permeate side. Afterwards, the oxygen with very high purity can be obtained by using vacuum in which the pressurized oxygen-enriched air produced from the first step is used as the feed gas. Accordingly, F. Y. Liang et al. reported a very high oxygen permeation flux of 10.2 mL min⁻¹ cm⁻² was achieved in the pure oxygen production at 900 °C via a dead-end BSCF tube membrane (see Figure 1.10)^[7] by feeding pressurized O₂-enriched air with 50 vol% O₂ at 5 bar and keeping the pressure on the permeate side at 0.05 bar through a vacuum pump.^[82]

1.5.2 Oxy-fuel combustion

Oxy-fuel combustion based on the oxygen-transporting membrane (OTM) technique has been proposed as one possible option for CO₂ capture integrated in the power plants.^[5,83] In this system (see Figure 1.11)^[83], an OTM module has been introduced into the traditional combustor for air separation, thus fossil fuels can be burning in a mixture of oxygen and recirculated flue gas (mainly consisting of CO₂ and

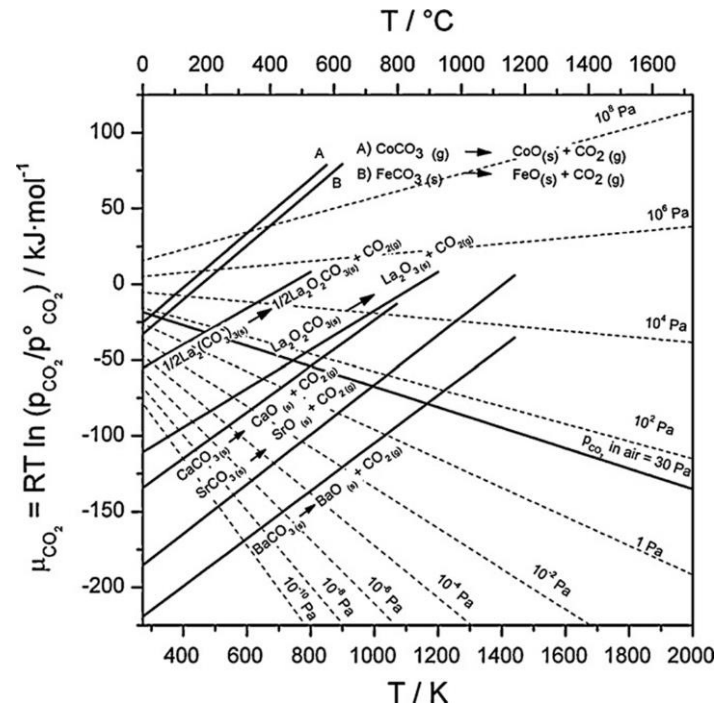
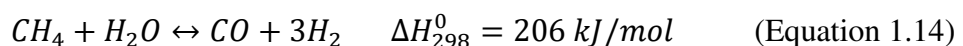


Figure 1.12 Ellingham diagram for the decomposition of carbonates under various partial pressures of CO_2 .^[85]

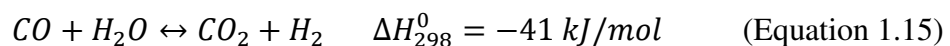
To sum up, doping strategy for single-phase perovskites may obviously enhance the CO_2 tolerance at the expense of oxygen permeation fluxes, which can be ascribed to a decrease in the concentration of oxygen vacancies.^[19] Compared to single-phase materials, the oxygen permeability of dual-phase membranes will also rely on the ionic conduction of fluorite phase, which reveals a high possibility to gain the good oxygen permeability as well as sufficient chemical stability at the same time. Therefore, it is concluded that the dual-phase membranes display the most promising potentials in industrial applications under harsh conditions, such as oxy-fuel combustion combined with CO_2 capture.^[63]

1.5.3 Partial oxidation of methane

The production of syngas (primarily consisting of H_2 and CO) is one of the most important chemical processes, because it is the first key step in the production of hydrogen, ammonia, methanol and a wide variety of valuable hydrocarbons, along with all the chemicals or materials made from these basic building blocks.^[89] Methane, which is the major component of natural gas, functions as the primary feedstock for syngas production. In most current industrial processes, the syngas is commonly produced by steam reforming of methane (SRM) according to the following reaction:

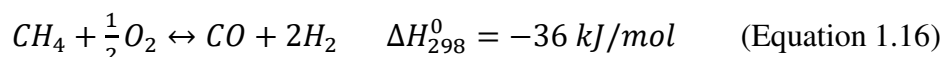


Under typical conditions, the water-gas-shift (WGS) reaction (see Equation 1.15) will also occur at appreciable rates.

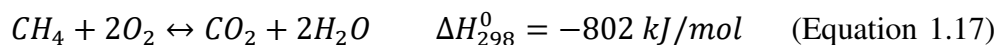


Finally, the reactions are assumed to reach the equilibrium. Unluckily, SRM is a highly endothermic reaction, which requires large amounts of additional heat to maintain the reaction temperature as well as to favor high equilibrium conversions, resulting in a substantial energy input and capital investment.^[90]

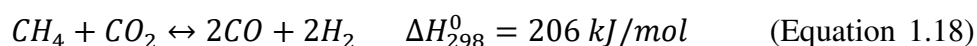
Alternatively, the partial oxidation of methane (POM) is considered to be another approach to convert methane to syngas. In a direct POM mode,^[90] oxygen reacts with methane to generate H₂ and CO:



The reaction is slightly exothermic, and the H₂/CO ratio of 2 is very suitable for the Fischer-Tropsch synthesis.^[91] However, the obtained products are more reactive than methane and can be further oxidized to H₂O and CO₂. Therefore, the actual mechanism for POM occurs most likely via a combustion and reforming process.^[90] In this mode, a portion of methane firstly combusts with oxygen completely:



The rest part of methane is then reformed by steam (see Equation 1.14) or CO₂ via the reaction:



Compared to SRM, the main bottleneck of POM is the pure oxygen supply, because the downstream processing of syngas cannot tolerate nitrogen.^[90,92]

Fortunately, OTM reactors can overcome the drawbacks of traditional fixed-bed reactors for POM reaction. Moreover, both the reaction stoichiometry and the interaction of the reactants can be controlled, which is beneficial to eliminate the hot-spot problem due to the high exothermic reaction above (Equation 1.17).^[90,92] Nevertheless, the commercial requirements of OTM for this application are quite stringent, because the membrane should possess economically feasible oxygen permeability (estimated to be 5~10 mL min⁻¹ cm⁻²)^[93] as well as adequate chemical and mechanical stability. Up to now, various materials have been investigated as potential candidates for fabricating the POM membrane reactors. U. Balachandran et al. observed that both SrCo_{0.8}Fe_{0.2}O_{3-δ} and La_{0.2}Sr_{0.8}Co_{0.8}Fe_{0.2}O_{3-δ} tube membranes fractured under POM conditions at 850 °C, which can be attributed to the mechanical strain caused by the lattice expansion in reducing atmospheres.^[94,95] On the contrary, C. S. Chen et al. successfully fabricated an oxygen permeable Zr_{0.84}Y_{0.16}O_{1.92}-La_{0.8}Sr_{0.2}Cr_{0.5}Fe_{0.5}O_{3-δ} (YSZ-LSCrF) dual-phase hollow-fiber POM membrane reactor, revealing high and stable oxygen permeation fluxes of ~7.9 mL min⁻¹ cm⁻² and remarkable methane conversion rates of over 90% at 950 °C under ~600 hours of operation.^[96] In short, the OTM reactors can reform methane at a high efficiency ascribed to the integration of oxygen separation from air and POM reaction in a single unit.

Furthermore, the fuels (mainly syngas) produced from methane by OTM reactors have a very desirable composition, since the atomic O/C ratio is greater than 1, resulting

in no carbon deposition on the Ni-based anodes of solid oxide fuel cells (SOFCs).^[97] Hence, a zero-emission methane-fuelled SOFC system integrated with CO₂ capture can be built up by placing OTM-based burners before and after the fuel cell (see Figure 1.13).^[96] The advantage is not only achieving high and stable energy efficiencies of the SOFCs, but also favoring efficient capture of CO₂ discharged from the fuel cells.

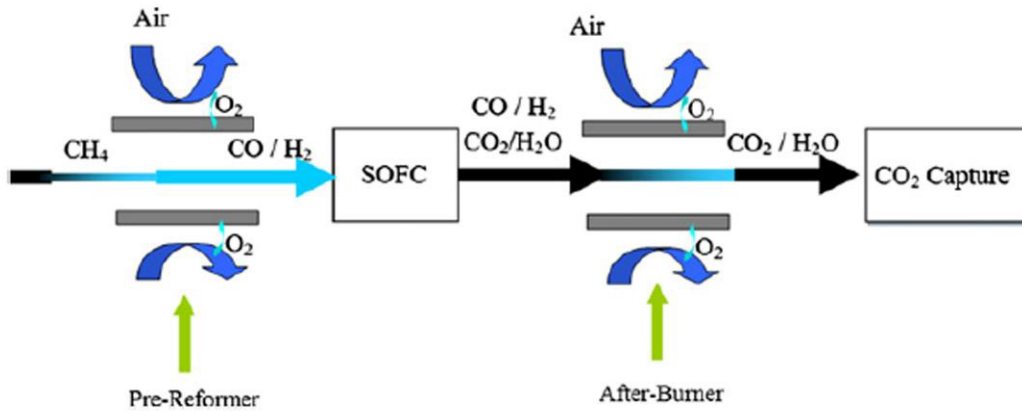


Figure 1.13 Concept of a zero-emission methane fuelled SOFC system.^[96]

In addition, the OTM reactors have been also constructed for coupling different chemical reactions on both sides of the membranes. Recently, H. Q. Jiang and J. Caro et al. reported the direct decomposition of N₂O with 100% conversion via a perovskite OTM by combining the POM reaction simultaneously (see Figure 1.14).^[98] Analogously, the water or CO₂ splitting reaction can be incorporated into the OTM reactor as well, which may contribute to the intensification of chemical processes.^[73,99,100]

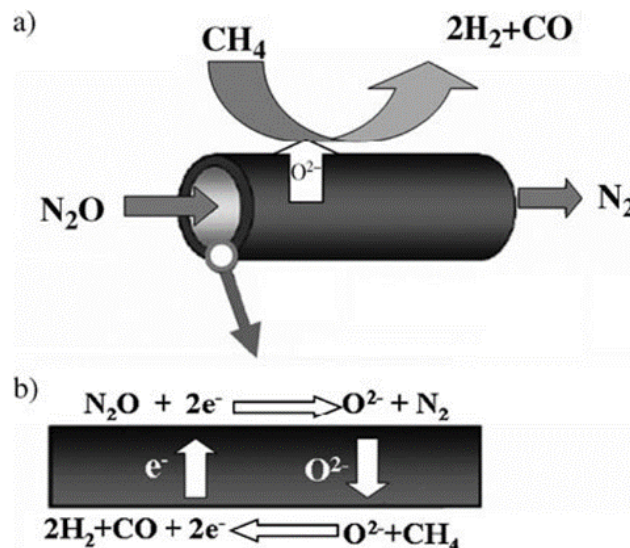


Figure 1.14 a) Mechanism of the N₂O decomposition by the in-situ removal of oxygen via an OTM. b) Description of the membrane reactions.^[98]

1.6 Bibliography

- [1] International Energy Agency, Key World Energy Statistics 2006.
- [2] S. Smart, C. X. C. Lin, L. Ding, K. Thambimuthu, J. C. D. da Costa, Ceramic membranes for gas processing in coal gasification, *Energy Environ. Sci.* **2010**, 3, 268-278.
- [3] P. Markewitz, W. Kuckshinrichs, W. Leitner, J. Linssen, P. Zapp, R. Bongartz, A. Schreiber, T. E. Müller, Worldwide innovations in the development of carbon capture technologies and the utilization of CO₂, *Energy Environ. Sci.* **2012**, 5, 7281-7305.
- [4] H. J. M. Bouwmeester, A. J. Burggraaf, Dense ceramic membranes for oxygen separation, A. J. Burggraaf, L. Cot (Eds.), Fundamentals of inorganic membrane science and technology, *Elsevier Science B. V., Amsterdam*, **1996**, pp. 435-528.
- [5] W. Chen, C. S. Chen, H. J. M. Bouwmeester, A. Nijmeijer, L. Winnubst, Oxygen-selective membranes integrated with oxy-fuel combustion, *J. Membr. Sci.* **2014**, 463, 166-172.
- [6] C. S. Chen, S. J. Feng, S. Ran, D. C. Zhu, W. Liu, H. J. M. Bouwmeester, Conversion of methane to syngas by a membrane-based oxidation-reforming process, *Angew. Chem. Int. Ed.* **2003**, 42, 5196-5198.
- [7] Y. Y. Wei, W. S. Yang, J. Caro, H. H. Wang, Dense ceramic oxygen permeable membranes and catalytic membrane reactors, *Chem. Eng. J.* **2013**, 220, 185-203.
- [8] C. Wagner, Equations for transport in solid oxides and sulfides of transition metals, *Prog. Solid State Chem.* **1975**, 10, 3-16.
- [9] R. Doshi, V. L. Richards, J. D. Carter, X. P. Wang, M. Krumpelt, Development of solid-oxide fuel cells that operate at 500 °C, *J. Electrochem. Soc.* **1999**, 146, 1273-1278.
- [10] G. Kim, S. Wang, A. J. Jacobson, L. Reimus, P. Brodersen, C. A. Mims, Rapid oxygen ion diffusion and surface exchange kinetics in PrBaCo₂O_{5+x} with a perovskite related structure and ordered A cations, *J. Mater. Chem.* **2007**, 17, 2500-2505.
- [11] L. Wang, R. Merkle, J. Maier, T. Acartürk. U. Starke, Oxygen tracer diffusion in dense Ba_{0.5}Sr_{0.5}Co_{0.8}Fe_{0.2}O_{3-δ} films, *Prog. Solid State Chem.* **1975**, 10, 3-16.
- [12] M. A. Peña, J. L. G. Fierro, Chemical structures and performance of perovskite oxides, *Chem. Rev.* **2001**, 101, 1981-2018.
- [13] Y. Teraoka, H. M. Zhang, S. Furukawa, N. Yamazoe, Oxygen permeation through perovskite-type oxides, *Chem. Lett.* **1985**, 14, 1743-1746.
- [14] Z. P. Shao, W. S. Yang, Y. Cong, H. Dong, J. H. Tong, G. X. Xiong, Investigation of the permeation behavior and stability of a Ba_{0.5}Sr_{0.5}Co_{0.8}Fe_{0.2}O_{3-δ} oxygen membrane, *J. Membr. Sci.* **2000**, 172, 177-188.

- [15] K. Efimov, Q. Xu, A. Feldhoff, Transmission electron microscopy study of $\text{Ba}_{0.5}\text{Sr}_{0.5}\text{Co}_{0.8}\text{Fe}_{0.2}\text{O}_{3-\delta}$ perovskite decomposition at intermediate temperatures, *Chem. Mater.* **2010**, *22*, 5866-5875.
- [16] T. Nagai, W. Ito, T. Sakon, Relationship between cation substitution and stability of perovskite structure in $\text{SrCoO}_{3-\delta}$ -based mixed conductors, *Solid State Ionics* **2007**, *177*, 3433-3444.
- [17] V. V. Kharton, A. L. Shaula, F. M. M. Snijkers, J. F. C. Coymans, J. J. Luyten, A. A. Yaremchenko, A. A. Valente, E. V. Tsipis, J. R. Frade, F. M. B. Marques, J. Rocha, Processing, stability and oxygen permeability of $\text{Sr}(\text{Fe}, \text{Al})\text{O}_{3-\delta}$ -based ceramic membranes, *J. Membr. Sci.* **2005**, *252*, 215-225.
- [18] J. H. Tong, W. S. Yang, B. C. Zhu, R. Cai, Investigation of ideal zirconium-doped perovskite-type ceramic membrane materials for oxygen separation, *J. Membr. Sci.* **2002**, *203*, 175-189.
- [19] Q. Zeng, Y. B. Zuo, C. G. Fan, C. S. Chen, CO_2 -tolerant oxygen separation membranes targeting CO_2 capture application, *J. Membr. Sci.* **2009**, *335*, 140-144.
- [20] J. X. Yi, J. Brendt, M. Schroeder, M. Martin, Oxygen permeation and oxidation states of transition metals in (Fe, Nb)-doped $\text{BaCoO}_{3-\delta}$ perovskites, *J. Membr. Sci.* **2012**, *387-388*, 17-23.
- [21] Y. Teraoka, T. Nobunaga, N. Yamazoe, Effect of cation substitution on the oxygen semipermeability of perovskite-type oxides, *Chem. Lett.* **1988**, *3*, 503-506.
- [22] A. V. Kovalevsky, V. V. Kharton, V. N. Tikhonovich, E. N. Naumovich, A. A. Tonoyan, O. P. Reut, L. S. Boginsky, Oxygen permeation through $\text{Sr}(\text{Ln})\text{CoO}_{3-\delta}$ (Ln= La, Nd, Sm, Gd) ceramic membranes, *Mater. Sci. Eng. B* **1998**, *52*, 105-116.
- [23] H. H. Wang, C. Tablet, A. Feldhoff, J. Caro, A cobalt-free oxygen-permeable membrane based on the perovskite-type oxide $\text{Ba}_{0.5}\text{Sr}_{0.5}\text{Zn}_{0.2}\text{Fe}_{0.8}\text{O}_{3-\delta}$, *Adv. Mater.* **2005**, *17*, 1785-1788.
- [24] K. Efimov, T. Halfer, A. Kuhn, P. Heitjans, J. Caro, A. Feldhoff, Novel cobalt-free oxygen-permeable perovskite-type membrane, *Chem. Mater.* **2010**, *22*, 1540-1544.
- [25] X. F. Zhu, H. H. Wang, W. S. Yang, Novel cobalt-free oxygen permeable membrane, *Chem. Comm.* **2004**, *9*, 1130-1131.
- [26] K. Watanabe, D. Takauchi, M. Yuasa, T. Kida, K. Shimanoe, Y. Teraoka, N. Yamazoe, Oxygen permeation properties of Co-free perovskite-type oxide membranes based on $\text{BaFe}_{1-y}\text{Zr}_y\text{O}_{3-\delta}$, *J. Electrochem. Soc.* **2009**, *156*, E81-E85.
- [27] T. Kida, D. Takauchi, K. Watanabe, M. Yuasa, K. Shimanoe, Y. Teraoka, N. Yamazoe, Oxygen permeation properties of partially A-site substituted $\text{BaFeO}_{3-\delta}$ perovskites, *J. Electrochem. Soc.* **2009**, *156*, E187-E191.

- [28] E. Juste, A. Julian, G. Etchegoyen, P. M. Geffroy, T. Chartier, N. Richet, P. D. Gallo, *J. Membr. Sci.* **2008**, *319*, 185-191.
- [29] F. M. Figueiredo, V. V. Kharton, A. P. Viskup, J. R. Frade, Surface enhanced oxygen permeation in $\text{CaTi}_{1-x}\text{Fe}_x\text{O}_{3-\delta}$ ceramic membranes, *J. Membr. Sci.* **2004**, *236*, 73-80.
- [30] I. Kaus, K. Wiik, B. Krogh, M. Dahle, K. H. Hofstad, S. Aasland, Stability of SrFeO_3 -based materials in $\text{H}_2\text{O}/\text{CO}_2$ -containing atmospheres at high temperatures and pressures, *J. Am. Ceram. Soc.* **2007**, *90*, 2226-2230.
- [31] S. Pei, M. S. Kleefisch, T. P. Kobylinski, J. Faber, C. A. Udovich, V. Z. McCoy, B. Dabrowski, U. Balachandran, R. L. Mieville, R. B. Poeppel, Failure mechanisms of ceramic membrane reactors in partial oxidation of methane to synthesis gas, *Catal. Lett.* **1994**, *30*, 201-212.
- [32] M. Mogensen, N. M. Sammes, G. A. Tompsett, Physical, chemical and electrochemical properties of pure and doped ceria, *Solid State Ionics* **2000**, *129*, 63-94.
- [33] E. C. Subbarao, H. S. Maiti, Solid electrolytes with oxygen ion conduction, *Solid State Ionics* **1984**, *11*, 317-338.
- [34] H. L. Tuller, A. S. Nowick, Doped ceria as a solid oxide electrolyte, *J. Electrochem. Soc.* **1975**, *122*, 255-259.
- [35] J. Kilner, B. C. H. Steele, Mass transport in anion-deficient fluorite oxides, O. Sørensen (Ed.), Nonstoichiometric oxides, *Academic Press, New York*, **1981**, pp. 233-269.
- [36] I. K. Naik, T. Y. Tien, Small-polaron mobility in nonstoichiometric cerium dioxide, *J. Phys. Chem. Solids* **1978**, *39*, 311-315.
- [37] H. L. Tuller, A. S. Nowick, Small polaron electron transport in reduced CeO_2 single crystals, *J. Phys. Chem. Solids* **1977**, *38*, 859-867.
- [38] E. H. Baker, M. Iqbal, B. E. Knox, Conductivity measurements on ceria at high oxygen pressures, *J. Mater. Sci.* **1977**, *12*, 305-310.
- [39] K. Schmale, M. Grünebaum, M. Janssen, S. Baumann, F. S. Küppers, H. D. Wiemhöfer, Electronic conductivity of $\text{Ce}_{0.8}\text{Gd}_{0.2-x}\text{Pr}_x\text{O}_{2-\delta}$ and influence of added CoO , *Phys. Status Solidi B* **2011**, *248*, 314-322.
- [40] T. H. Etsell, S. N. Flengas, Electrical properties of solid oxide electrolytes, *Chem. Rev.* **1970**, *70*, 339-376.
- [41] B. Z. Christiansen, T. Jacobsen, S. Skaarup, Electrochemical determination of oxygen stoichiometry and entropy in oxides, *Solid State Ionics* **1996**, *86-88*, 725-731.
- [42] J. D. Sirman, D. Waller, J. A. Kilner, Solid oxide fuel cells V, U. Stimming, S. C. Singhal, H. Tagawa, W. Lehnert (Eds.), *Electrochem. Soc. Proc.* **1997**, *97*, 1159.

- [43] D. J. Kim, Lattice parameters, ionic conductivities, and solubility limits in fluorite-structure MO₂ oxide [M= Hf⁴⁺, Zr⁴⁺, Ce⁴⁺, Th⁴⁺, U⁴⁺] solid solutions, *J. Am. Ceram. Soc.* **1989**, 72, 1415-1421.
- [44] X. D. Zhou, W. Huebner, I. Kosacki, H. U. Anderson, Microstructure and grain-boundary effect on electrical properties of gadolinium-doped ceria, *J. Am. Ceram. Soc.* **2002**, 85, 1757-1762.
- [45] K. Eguchi, T. Setoguchi, T. Inoue, H. Arai, Electrical properties of ceria-based oxides and their application to solid oxide fuel cells, *Solid State Ionics* **1992**, 52, 165-172.
- [46] S. Zha, C. R. Xia, G. Y. Meng, Effect of Gd (Sm) doping on properties of ceria electrolyte for solid oxide fuel cells, *J. Power Sources* **2003**, 115, 44-48.
- [47] J. Faber, C. Geoffroy, A. Roux, A. Sylvestre, P. Abélard, A systematic investigation of the dc electrical conductivity of rare-earth doped ceria, *Appl. Phys. B* **1989**, 49, 225-232.
- [48] K. E. Adham, A. Hammou, "Grain boundary effect" on ceria based solid solutions, *Solid State Ionics* **1983**, 9-10, 905-912.
- [49] Y. M. Chiang, E. B. Lavik, D. A. Blom, Defect thermodynamics and electrical properties of nanocrystalline oxides: pure and doped CeO₂, *Nanostruct. Mater.* **1997**, 9, 633-642.
- [50] H. L. Tuller, Ionic conduction in nanocrystalline materials, *Solid State Ionics* **2000**, 131, 143-157.
- [51] G. M. Christie, F. P. F. van Berkel, Microstructure-ionic conductivity relationships in ceria-gadolinia electrolytes, *Solid State Ionics* **1996**, 83, 17-27.
- [52] T. Matsui, M. Inaba, A. Mineshige, Z. Ogumi, Electrochemical properties of ceria-based oxides for use in intermediate-temperature SOFCs, *Solid State Ionics* **2005**, 176, 647-654.
- [53] M. Balaguer, C. Solís, J. M. Serra, Study of the transport properties of the mixed ionic electronic conductor Ce_{1-x}Tb_xO_{2-δ} + Co (x= 0.1, 0.2) and evaluation as oxygen-transport membrane, *Chem. Mater.* **2011**, 23, 2333-2343.
- [54] T. S. Stefanik, H. L. Tuller, Nonstoichiometry and defect chemistry in praseodymium-cerium oxide, *J. Electroceram.* **2004**, 13, 799-803.
- [55] V. V. Kharton, A. P. Viskup, F. M. Figueiredo, E. N. Naumovich, A. A. Yaremchenko, F. M. B. Marques, Electron-hole conduction in Pr-doped Ce(Gd)O_{2-δ} by faradaic efficiency and emf measurements, *Electrochim. Acta.* **2001**, 46, 2879-2889.
- [56] D. P. Fagg, V. V. Kharton, J. R. Frade, P-type electronic transport in Ce_{0.8}Gd_{0.2}O_{2-δ}: the effect of transition metal oxide sintering aids, *J. Electroceram.* **2002**, 9, 199-207.
- [57] M. P. Lobera, J. M. Serra, S. P. Foghmoes, M. Sjøgaard, A. Kaiser, On the use

- of supported ceria membranes for oxyfuel process/syngas production, *J. Membr. Sci.* **2011**, 385-386, 154-161.
- [58] C. S. Chen, B. A. Boukamp, H. J. M. Bouwmeester, G. Z. Cao, H. Kruidhof, A. J. A. Winnubst, A. J. Burggraaf, Microstructural development, electrical properties and oxygen permeation of zirconia-palladium composites, *Solid State Ionics* **1995**, 76, 23-28.
- [59] K. Huang, J. B. Goodenough, Solid oxide fuel cell technology: principles, performance and operations, *Woodhead Publishing, Cambridge*, **2009**.
- [60] V. V. Kharton, A. V. Kovalevsky, A. P. Viskup, F. M. Figueiredo, A. A. Yaremchenko, E. N. Naumovich, F. M. B. Marques, Oxygen permeability of $\text{Ce}_{0.8}\text{Gd}_{0.2}\text{O}_{2-\delta}\text{-La}_{0.7}\text{Sr}_{0.3}\text{MnO}_{3-\delta}$ composite membranes, *J. Electrochem. Soc.* **2000**, 147, 2814-2821.
- [61] S. B. Adler, Factors governing oxygen reduction in solid oxide fuel cell cathodes, *Chem. Rev.* **2004**, 26, 4387-4394.
- [62] V. V. Kharton, A. V. Kovalevsky, A. P. Viskup, A. L. Shaula, F. M. Figueiredo, E. N. Naumovich, F. M. B. Marques, Oxygen transport in $\text{Ce}_{0.8}\text{Gd}_{0.2}\text{O}_{2-\delta}$ -based composite membranes, *Solid State Ionics* **2003**, 160, 247-258.
- [63] W. Fang, F. Y. Liang, Z. W. Cao, F. Steinbach, A. Feldhoff, A mixed ionic and electronic conducting dual-phase membrane with high oxygen permeability, *Angew. Chem. Int. Ed.* **2014**, 54, 4847-4850.
- [64] J. H. Joo, K. S. Yun, Y. Lee, J. Jung, C. Y. Yoo, J. H. Yu, Dramatically enhanced oxygen fluxes in fluorite-rich dual-phase membrane by surface modification, *Chem. Mater.* **2014**, 26, 4387-4394.
- [65] Q. M. Li, X. F. Zhu, Y. F. He, Y. Cong, W. S. Yang, Effects of sintering temperature on properties of dual-phase oxygen permeable membranes, *J. Membr. Sci.* **2011**, 367, 134-140.
- [66] H. X. Luo, K. Efimov, H. Q. Jiang, A. Feldhoff, H. H. Wang, J. Caro, CO_2 -stable and cobalt-free dual-phase membrane for oxygen separation, *Angew. Chem. Int. Ed.* **2011**, 50, 759-763.
- [67] X. F. Zhu, Y. Liu, Y. Cong, W. S. Yang, $\text{Ce}_{0.85}\text{Sm}_{0.15}\text{O}_{1.925}\text{-Sm}_{0.6}\text{Sr}_{0.4}\text{Al}_{0.3}\text{Fe}_{0.7}\text{O}_3$ dual-phase membranes: one-pot synthesis and stability in a CO_2 atmosphere, *Solid State Ionics* **2013**, 253, 57-63.
- [68] M. Sun, X. W. Chen, L. Hong, Influence of the interfacial phase on the structural integrity and oxygen permeability of a dual-phase membrane, *ACS Appl. Mater. Interfaces* **2013**, 5, 9067-9074.
- [69] X. F. Zhu, H. H. Wang, W. S. Yang, Relationship between homogeneity and oxygen permeability of composite membrane, *J. Membr. Sci.* **2008**, 309, 120-127.
- [70] W. Fang, F. Steinbach, C. S. Chen, A. Feldhoff, An approach to enhance the

- CO₂ tolerance of fluorite-perovskite dual-phase oxygen-transporting membrane, *Chem. Mater.* **2015**, *27*, 7820-7826.
- [71] S. Baumann, J. M. Serra, M. P. Lobera, S. Escolástico, F. S. Küppers, W. A. Meulenber, Ultrahigh oxygen permeation flux through supported Ba_{0.5}Sr_{0.5}Co_{0.8}Fe_{0.2}O_{3-δ} membranes, *J. Membr. Sci.* **2011**, *377*, 198-205.
- [72] C. R. Xia, F. L. Chen, M. L. Liu, Reduced-temperature solid oxide fuel cells fabricated by screen printing, *Electrochem. Solid-State Lett.* **2001**, *4*, A52-A54.
- [73] W. Fang, F. Steinbach, Z. W. Cao, X. F. Zhu, A. Feldhoff, A highly efficient sandwich-like symmetrical dual-phase oxygen-transporting membrane reactor for hydrogen production by water splitting, *Angew. Chem. Int. Ed.* **2016**, *55*, 8648-8651.
- [74] W. He, H. Huang, J. F. Gao, L. Winnubst, C. S. Chen, Phase-inversion tape casting and oxygen permeation properties of supported ceramic membranes, *J. Membr. Sci.* **2014**, *452*, 294-299.
- [75] W. Li, J. J. Liu, C. S. Chen, Hollow fiber membrane of yttrium-stabilized zirconia and strontium-doped lanthanum manganite dual-phase composite for oxygen separation, *J. Membr. Sci.* **2009**, *340*, 266-271.
- [76] H. H. Wang, C. Tablet, T. Schiestel, S. Werth, J. Caro, Partial oxidation of methane to syngas in a perovskite hollow fiber membrane reactor, *Catal. Commun.* **2006**, *7*, 907-912.
- [77] T. Liu, W. He, H. Huang, S. W. Wang, H. J. M. Bouwmeester, C. S. Chen, Ce_{0.8}Sm_{0.2}O_{1.9}-La_{0.8}Sr_{0.2}Cr_{0.5}Fe_{0.5}O_{3-δ} dual-phase hollow fiber membranes operated under different gradients, *Ind. Eng. Chem. Res.* **2014**, *53*, 6131-6136.
- [78] B. F. K. Kingsbury, K. Li, A morphological study of ceramic hollow fibre membranes, *J. Membr. Sci.* **2009**, *328*, 134-140.
- [79] Z. T. Wu, B. Wang, K. Li, A novel dual-layer ceramic hollow fibre membrane reactor for methane conversion, *J. Membr. Sci.* **2010**, *352*, 63-70.
- [80] Y. Y. Wei, H. F. Liu, J. Xue, Z. Li, H. H. Wang, Preparation and oxygen permeation of U-shaped perovskite hollow-fiber membranes, *AIChE. J.* **2011**, *57*, 975-984.
- [81] P. A. Armstrong, D. L. Bennett, E. P. Foster, V. E. Stein, ITM oxygen for gasification, *Proceedings of gasification technologies, Washington D. C.*, **2011**.
- [82] F. Y. Liang, H. Q. Jiang, T. Schiestel, J. Caro, High-purity oxygen production from air using perovskite hollow fiber membranes, *Ind. Eng. Chem. Res.* **2010**, *49*, 9377-9384.
- [83] K. E. Colombo, O. Bolland, V. V. Kharton, C. Stiller, Simulation of an oxygen membrane-based combined cycle power plant: part-load operation with operational and material constraints, *Energy Environ. Sci.* **2009**, *2*, 1310-1324.
- [84] J. X. Yi, S. J. Feng, Y. B. Zuo, W. Liu, C. S. Chen, Oxygen permeability and

- stability of $\text{Sr}_{0.95}\text{Co}_{0.8}\text{Fe}_{0.2}\text{O}_{3-\delta}$ in a CO_2 - and H_2O -containing atmosphere, *Chem. Mater.* **2005**, *17*, 5856-5861.
- [85] K. Efimov, T. Klande, N. Juditzki, A. Feldhoff, Ca-containing CO_2 -tolerant perovskite materials for oxygen separation, *J. Membr. Sci.* **2012**, *389*, 205-215.
- [86] T. Klande, O. Ravkina, A. Feldhoff, Effect of A-site lanthanum doping on the CO_2 tolerance of $\text{SrCo}_{0.8}\text{Fe}_{0.2}\text{O}_{3-\delta}$ oxygen-transporting membranes, *J. Membr. Sci.* **2013**, *437*, 122-130.
- [87] F. Y. Liang, H. X. Luo, K. Partovi, O. Ravkina, Z. W. Cao, Y. Liu, J. Caro, A novel CO_2 -stable dual phase membrane with high oxygen permeability, *Chem. Commu.* **2014**, *50*, 2451-2454.
- [88] W. Chen, C. S. Chen, L. Winnubst, Ta-doped $\text{SrCo}_{0.8}\text{Fe}_{0.2}\text{O}_{3-\delta}$ membranes: phase stability and oxygen permeation in CO_2 atmosphere, *Solid State Ionics* **2011**, *196*, 30-33.
- [89] A. S. Yu, J. M. Vohs, R. J. Gorte, Interfacial reactions in ceramic membrane reactors for syngas production, *Energy Environ. Sci.* **2014**, *7*, 944-953.
- [90] J. Kniep, Y. S. Lin, Partial oxidation of methane and oxygen permeation in SrCoFeO_x membrane reactor with different catalysts, *Ind. Eng. Chem. Res.* **2011**, *50*, 7941-7948.
- [91] H. Schulz, Short history and present trends of Fischer-Tropsch synthesis, *Appl. Catal. A* **1999**, *186*, 3-12.
- [92] J. H. Tong, W. S. Yang, R. Cai, B. C. Zhu, L. W. Lin, Novel and ideal zirconium-based dense membrane reactors for partial oxidation of methane to syngas, *Catal. Lett.* **2002**, *78*, 129-137.
- [93] M. Ikeguchi, T. Mimura, Y. Sekine, E. Kikuchi, M. Matsukata, Reaction and oxygen permeation studies in $\text{Sm}_{0.4}\text{Ba}_{0.6}\text{Fe}_{0.8}\text{Co}_{0.2}\text{O}_{3-\delta}$ membrane reactor for partial oxidation of methane to syngas, *Appl. Catal. A* **2005**, *290*, 212-220.
- [94] U. Balachandran, J. T. Dusek, P. S. Maiya, B. Ma, R. L. Mieville, M. S. Kleefisch, C. A. Udovich, Ceramic membrane reactor for converting methane to syngas, *Catal. Today* **1997**, *36*, 265-272.
- [95] U. Balachandran, J. T. Dusek, R. L. Mieville, R. B. Poeppel, M. S. Kleefisch, S. Pei, T. P. Kobylinski, C. A. Udovich, A. C. Bose, Dense ceramic membranes for partial oxidation of methane to syngas, *Appl. Catal. A* **1995**, *133*, 19-29.
- [96] J. J. Liu, S. Q. Zhang, W. D. Wang, J. F. Gao, W. Liu, C. S. Chen, Partial oxidation of methane in a $\text{Zr}_{0.84}\text{Y}_{0.16}\text{O}_{1.92}\text{-La}_{0.8}\text{Sr}_{0.2}\text{Cr}_{0.5}\text{Fe}_{0.5}\text{O}_{3-\delta}$ hollow fiber membrane reactor targeting solid oxide fuel cell applications, *J. Power Sources* **2012**, *217*, 287-290.
- [97] Z. L. Zhan, Y. B. Lin, M. Pillai, I. Kim, S. A. Barnett, High-rate electrochemical partial oxidation of methane in solid oxide fuel cells, *J. Power Sources* **2006**, *161*, 460-465.

- [98] H. Q. Jiang, H. H. Wang, F. Y. Liang, S. Werth, T. Schiestel, J. Caro, Direct decomposition of nitrous oxide to nitrogen by in situ oxygen removal with a perovskite membrane, *Angew. Chem. Int. Ed.* **2009**, *48*, 2983-2986.
- [99] C. Zhang, W. Q. Jin, C. Yang, N. P. Xu, Decomposition of CO₂ coupled with POM in a thin tubular oxygen-permeable membrane reactor, *Catal. Today* **2009**, *148*, 298-302.
- [100] W. P. Li, X. F. Zhu, S. G. Chen, W. S. Yang, Integration of nine steps into one membrane reactor to produce synthesis gases for ammonia and liquid fuel, *Angew. Chem. Int. Ed.* **2016**, *128*, 8708-8712.

2 Investigation of CO₂-tolerant dual-phase oxygen-transporting membranes for oxy-fuel combustion

2.1 Summary

Dual-phase oxygen-transporting membranes (OTMs), especially perovskite-fluorite composites, are considered to be the most promising candidates for oxy-fuel combustion combined with CO₂ capture. Nowadays, oxygen permeability and stability are two crucial bottlenecks which limit the process of industrialization for OTMs. Therefore, the challenge is mainly focused on designing the dual-phase materials with both good permeability and sufficient stability, as well as understanding the mechanism of CO₂ tolerance.

In section 2.2, instead of combining an ionic conductor (IC) and an electron conductor (EC), two separated mixed ionic-electronic conductors (MIECs) are involved to build the dual-phase OTM. Based on this strategy, a dual-phase membrane with the nominal composition of 75 wt.% Ce_{0.85}Gd_{0.1}Cu_{0.05}O_{2-δ}-25 wt.% La_{0.6}Ca_{0.4}FeO_{3-δ} (CGCO-LCF) has been successfully developed via a one-pot method, which shows a very high oxygen permeation flux of 0.70 mL min⁻¹ cm⁻² under CO₂-rich atmosphere at 950 °C and excellent stability in the presence of CO₂ even at lower temperature (800 °C) during long-term operation. Furthermore, it is considered that copper doping into the CGO oxide enhances both ionic and electronic conduction, which results in an enhancement of the oxygen surface exchange kinetics and the bulk diffusion rate of the CGCO-LCF dual-phase membrane. Moreover, the formation of an emergent intergranular film was detected at the grain boundary between two CGCO grains, which may be beneficial to the grain boundary conduction. This study demonstrates the great potential of a CGCO-LCF one-pot membrane as one of the most competitive OTMs, and expands the concepts of dual-phase composite membranes as well.

In section 2.3, the chemical potential of oxygen is firstly identified as a novel possible factor that dramatically impacts the CO₂ tolerance of dual-phase OTMs. Thus, a simple but remarkably effective approach is put forward to enable the stabilization of oxygen permeation fluxes of fluorite-perovskite dual-phase OTM in the presence of CO₂ by increasing the chemical potential of oxygen at the feed side. In other words, it is demonstrated that oxygen can serve as a “buffer” and effectively prevent the formation of carbonates. Accordingly, high and stable oxygen permeation fluxes of over 0.84 mL min⁻¹ cm⁻² were gained in a 80 wt.% Ce_{0.8}Gd_{0.15}Cu_{0.05}O_{2-δ}-20 wt.% SrFeO_{3-δ} (CGCO-SFO, nominal composition) dual-phase membrane at 900 °C under CO₂-rich condition by applying oxygen-enriched air as the feed gas. Additionally, the drop in chemical potential of oxygen across the dual-phase OTM was discussed in detail and further addressed in the model, which is beneficial to the principle fundamentals of dual-phase OTMs.

2.2 A mixed ionic and electronic conducting dual-phase membrane with high oxygen permeability

Wei Fang,* Fangyi Liang, Zhengwen Cao, Frank Steinbach and Armin Feldhoff

Angewandte Chemie International Edition 2015, 54, 4847-4850.

Reprinted (adapted) with permission from (Angewandte Chemie International Edition). Copyright (2015) Wiley-VCH Verlag GmbH & Co. KGaA, Weinheim.

A Mixed Ionic and Electronic Conducting Dual-Phase Membrane with High Oxygen Permeability**

Wei Fang,* Fangyi Liang, Zhengwen Cao, Frank Steinbach, and Armin Feldhoff

Abstract: To combine good chemical stability and high oxygen permeability, a mixed ionic–electronic conducting (MIEC) 75 wt % $\text{Ce}_{0.85}\text{Gd}_{0.1}\text{Cu}_{0.05}\text{O}_{2-\delta}$ –25 wt % $\text{La}_{0.6}\text{Ca}_{0.4}\text{FeO}_{3-\delta}$ (CGCO–LCF) dual-phase membrane based on a MIEC–MIEC composite has been developed. Copper doping into $\text{Ce}_{0.9}\text{Gd}_{0.1}\text{O}_{2-\delta}$ (CGO) oxide enhances both ionic and electronic conductivity, which then leads to a change from ionic conduction to mixed conduction at elevated temperatures. For the first time we demonstrate that an intergranular film with 2–10 nm thickness containing Ce, Ca, Gd, La, and Fe has been formed between the CGCO grains in the CGCO–LCF one-pot dual-phase membrane. A high oxygen permeation flux of $0.70 \text{ mL min}^{-1} \text{ cm}^{-2}$ is obtained by the CGCO–LCF one-pot dual-phase membrane with 0.5 mm thickness at 950°C using pure CO_2 as the sweep gas, and the membrane shows excellent stability in the presence of CO_2 even at lower temperatures (800°C) during long-term operation.

Mixed ionic–electronic conducting (MIEC) oxides are promising candidate materials for catalysts,^[1] electrodes of batteries and fuel cells,^[2] and also oxygen-transporting membranes (OTMs).^[3] OTMs have gained increasing attention owing to their potential applications in oxygen supply,^[4] CO_2 capture integrated in oxy-fuel power plants,^[5] and catalytic membrane reactors.^[6] Most of the well-established MIEC materials for OTMs are oxygen-deficient perovskite oxides, for example, $\text{Ba}_{0.5}\text{Sr}_{0.5}\text{Co}_{0.8}\text{Fe}_{0.2}\text{O}_{3-\delta}$ ^[7] and $\text{La}_{1-x}\text{Sr}_x\text{Co}_{1-y}\text{Fe}_y\text{O}_{3-\delta}$.^[8] Unfortunately, these perovskites degrade rapidly in the presence of CO_2 , H_2O , and other reactive gases,^[9] and accordingly their use is rather limited. Although Ca-containing perovskites (for example, $\text{La}_{1-x}\text{Ca}_x\text{FeO}_{3-\delta}$) show great tolerance to CO_2 ,^[10] the oxygen flux is relatively poor and thus it is not desired for practical applications.

Alternatively, fluorite-type CeO_2 -based oxides are especially attractive owing to a combination of fast oxygen-ion mobility, good redox catalytic properties, and excellent chemical compatibility with CO_2 and H_2O at elevated

temperatures.^[11] Furthermore, these materials exhibit n-type electronic conductivity under reducing conditions that is due to a small-polaron hopping process between cerium sites.^[12] To improve CeO_2 -based oxides with high oxygen-ion conductivity, aliovalent doping with lanthanide cations have been extensively investigated, and the highest ionic conductivities are reported in Gd- and Sm-doped cerias.^[12] The conductivities of such cerias are found to be predominantly ionic under oxidizing atmospheres.^[12] Many efforts are underway to improve the properties of these oxides further by co-doping techniques.^[13] Transition metal oxides such as CuO , Co_3O_4 , and MnO_2 have been proposed to improve the sintering behavior and densification of cerias.^[14] However, the effect of co-doping of lanthanide and multivalent cations in the CeO_2 structure has not attracted much attention.^[15,16] The co-doping behavior increases the ionic conductivity, and also develops the p-type electronic conductivity, which allows the extension of the mixed ionic–electronic conduction to higher oxygen partial pressures (10^{-5} to 10^{-1} atm), but the oxygen permeation of these materials may still be limited by insufficient electronic conductivity.^[16,17]

Besides single-phase membranes, dual-phase membranes could be also developed by the combination of ionic conducting (IC) materials and electronic conducting (EC) materials.^[18,19] The oxygen transport processes in two conventional concepts for dual-phase membranes are illustrated in Figure 1 a and Figure 1 b, respectively. For an IC–EC composite conductor, it is comprised of a fluorite-type IC oxide (for example, $\text{Ce}_{0.9}\text{Gd}_{0.1}\text{O}_{2-\delta}$, CGO) for oxygen ionic transport and a pure EC oxide ($\text{La}_{0.7}\text{Sr}_{0.3}\text{MnO}_{3-\delta}$) for electronic transport,^[18] and the oxygen surface-exchange reaction (OSER) is generally thought to be confined at the triple phase boundary (TPB; Figure 1 a).^[20] One strategy to improve the performance has been to replace the pure EC oxide with a perovskite predominantly electronic MIEC oxide ($\text{La}_{0.6}\text{Sr}_{0.4}\text{Co}_{0.2}\text{Fe}_{0.8}\text{O}_{3-\delta}$) for both oxygen ionic and electronic transport (Figure 1 b).^[21] By introducing ionic transport to the EC phase, OSER could take place not only at the TPBs, but also over a significant portion of the MIEC surface, thereby extending the size of the active region and improving the kinetics at high temperatures (800 – 1000°C ; Figure 1 b).^[20] Recently, a MIEC–EC composite membrane ($\text{Ce}_{0.8}\text{Tb}_{0.2}\text{O}_{2-\delta}$ – NiFe_2O_4) has been also reported.^[22] However, the application of these dual-phase materials is still limited owing to low oxygen permeability.

Herein, we report a novel concept of dual-phase membrane, 75 wt % $\text{Ce}_{0.85}\text{Gd}_{0.1}\text{Cu}_{0.05}\text{O}_{2-\delta}$ (CGCO)–25 wt % $\text{La}_{0.6}\text{Ca}_{0.4}\text{FeO}_{3-\delta}$ (LCF), comprising of a predominantly ionic MIEC oxide CGCO with a fluorite structure and a predominantly electronic MIEC oxide LCF with a perovskite struc-

[*] W. Fang, Dr. F. Y. Liang, Dr. Z. W. Cao, F. Steinbach, Prof. Dr. A. Feldhoff
 Institute of Physical Chemistry and Electrochemistry
 Leibniz University Hannover
 Callinstrasse 22, 30167 Hannover (Germany)
 E-mail: wei.fang@pci.uni-hannover.de

[**] This work has been supported by German Research Foundation (DFG) (no. FE928/7-1). We also acknowledge Y. Y. Wei, A. Schulz, B. Geppert, A. Düvel, and O. Ravkina for technical support.

Supporting information for this article is available on the WWW under <http://dx.doi.org/10.1002/anie.201411963>.

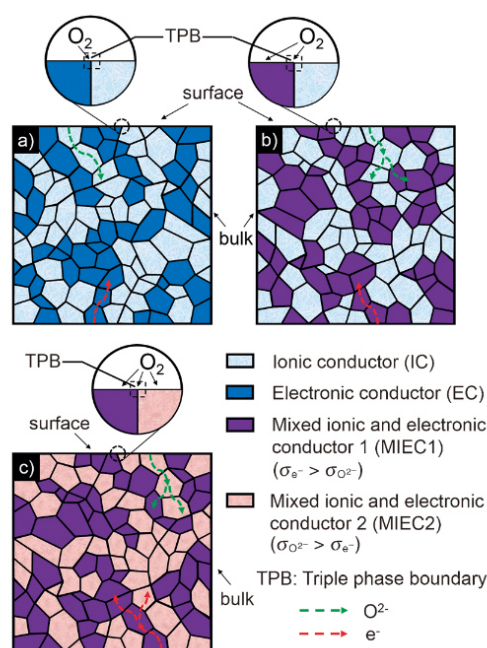


Figure 1. Concept of dual-phase membranes. a) IC-EC conductor. b) IC-MIEC1 conductor. c) MIEC1-MIEC2 conductor. $\sigma_{O^{2-}}$: oxygen ionic conductivity, σ_{e^-} : electronic conductivity.

ture. As illustrated in Figure 1c, with this composite strategy, the oxygen ions and electrons are transported in both MIEC phases at the same time, which enables the OSER to be extended to the overall surface area of the dual-phase membrane, thus significantly increasing the rate of OSER and bulk diffusion for oxygen permeation. This CGCO-LCF dual-phase membrane demonstrates considerable oxygen permeability and excellent stability in the presence of CO_2 , exhibiting great potential as competitive OTM.

The dual-phase membranes were prepared by using the powder mixing and one-pot method. X-ray diffraction patterns (Supporting Information, Figure S1) of the as-synthesized powders of these membranes clearly show that both the CGO and CGCO powders consist of a major cubic fluorite phase with space group $Fm\bar{3}m$, while the LCF powder exhibits an orthorhombic perovskite structure with space group $Pnma$. Compared to CGO powders ($a = 541.8$ pm), a slight decrease in lattice parameters was found for CGCO ($a = 541.6$ pm) at room temperature in air, since the radius of Cu^{2+} (73 pm) is smaller than that of Ce^{4+} (97 pm).^[23] And CGCO has larger thermal expansion coefficient (TEC) of cell parameters than CGO in air and N_2 atmospheres (Supporting Information, Figure S2 and Table S2). Moreover, it is noticed that the copper doping for the ceria-based oxide enables a substantial improvement of the total conductivity (determined by ionic conductivity) and ambipolar conductivity (determined by the rate limiting steps; Supporting Information, Figures S3–S5). In situ XRD was used to characterize the phase stability of the CGCO-LCF dual-phase materials in air and pure CO_2 . The CGCO phase remains unchanged with an increase in the temperature, while the LCF phase reveals

a reversible change from orthorhombic to cubic perovskite structure above $700^\circ C$ (Supporting Information, Figure S6 and Table S3), and no carbonate formation could be detected over the whole temperature range (Supporting Information, Figure S7).

The surface morphologies of the sintered dual-phase membranes are shown in Figure 2. In comparison to powder

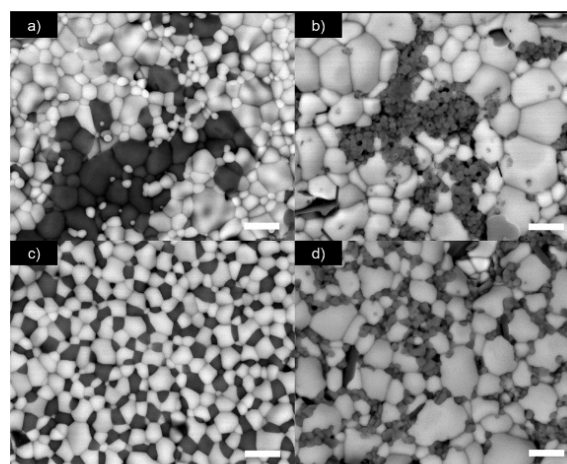


Figure 2. BSE micrographs of the surface of the dual-phase membranes. a) CGO-LCF mix membrane. b) CGCO-LCF mix membrane. c) CGO-LCF one-pot membrane. d) CGCO-LCF one-pot membrane. The light grains are the CGO or CGCO phase, and the dark grains are the LCF phase. Scale bars: 3 μm.

mixing membranes (Figure 2a,b), the membranes prepared by the one-pot method exhibit a much higher homogenization of the two phases (Figure 2c,d). The grains could be distinguished in the back-scattered electron (BSE) micrographs. The BSE micrographs also indicate that Cu-doped CGO has a much larger grain size than CGO. Therefore, we think that copper acts as a sintering aid and significantly lowers the densification temperature. The information about the elemental distribution is confirmed by the energy-dispersive X-ray spectroscopy (EDXS) images of the CGCO-LCF one-pot dual-phase membrane (Supporting Information, Figure S8,S9).

Figure 3 displays the investigation by transmission electron microscopy (TEM) of the CGCO-LCF one-pot dual-phase membrane. An intergranular film between two CGCO grains with the thickness from 2 to 10 nm can be seen by bright contrast in the TEM dark-field micrograph of Figure 3a and by dark contrast in the STEM annular dark-field micrograph of Figure 3b. Electron energy-loss (EEL) spectra as shown in Figure 3c reveal the chemical nature of the CGCO grains and the intergranular film. The three background-subtracted EEL spectra were obtained from linescan across the grain boundary between two CGCO grains (Supporting Information, Figure S11). The diameter of the electron beam was 1.5 nm. The spectra for CGCO were taken in ca. 6–8 nm distance to the grain boundary from both sides. The spectra for the two CGCO grains are almost identical and

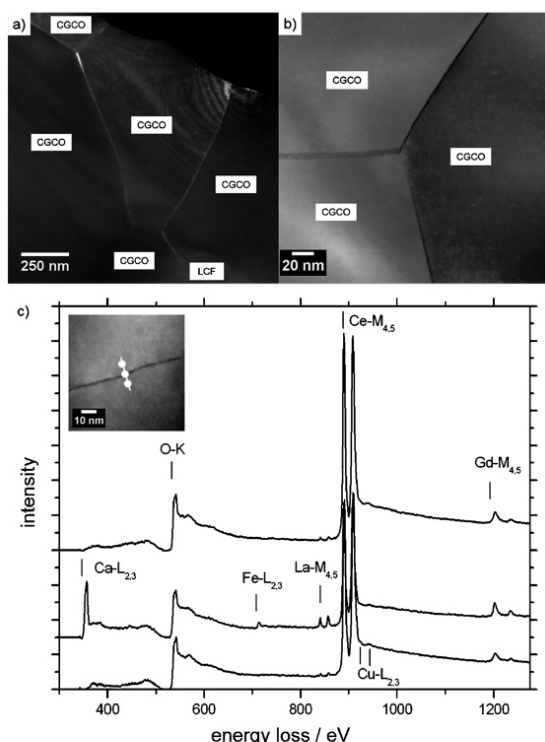


Figure 3. CGCO-LCF one-pot dual-phase membrane. a) TEM dark-field, b) STEM annular dark-field, c) EEL spectra across the grain boundary between two CGCO grains (see inset). Background was subtracted according to power law with supporting points in front of Ca-L_{2,3} edge and in front of the O-K edge. For the full line profile, see the Supporting Information, Figure S11.

show a O-K ionization edge at 534 eV as well as intense Ce-M_{4,5} white lines at 884 eV and weaker Gd-M_{4,5} white lines at 1186 eV. Note the weak white lines of Cu-L_{2,3} at 931 eV can be found, at the right of Ce-M_{4,5} white lines at 884 eV, and La-M_{4,5} white lines at 832 eV. In the spectrum taken from the grain boundary region, these features of the adjacent CGCO grains are present as well, but it also shows a Ca-L_{2,3} ionization edge at 347 eV and a Fe-L_{2,3} ionization edge at 710 eV. It is also observed that at the grain boundary the La-M_{4,5} white line at 832 eV is more intense, but the Cu-L_{2,3} white lines at 931 eV are hard to observe. Therefore, we can conclude that most of Cu is incorporated into the ceria lattice, and no significant segregation of Cu could be found at the grain boundary. One possible explanation for the formation of the intergranular film is that during the one-pot synthesis,^[24] a small amount of Ca, La, and Fe can easily segregate at the grain boundary between CGCO grains. A similar effect of CaO addition to CGO was also reported, which had been proved to bring out a positive influence on the grain-boundary conduction.^[25] Furthermore, an interdiffusion zone at the interface between the CGCO and LCF grains has been observed by the EEL spectra technique (Supporting Information, Figure S12).

Figure 4 presents the oxygen permeation fluxes of CeO₂-based dual-phase membranes and LCF single-phase mem-

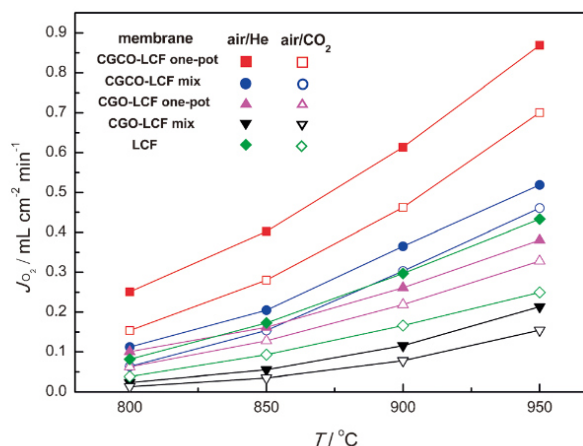


Figure 4. Oxygen permeation fluxes of CeO₂-based dual-phase membranes and the LCF single-phase membrane as a function of temperature. Condition: 100 mL min⁻¹ air as the feed gas, 30 mL min⁻¹ He or CO₂ as the sweep gas; membrane thickness: 0.5 mm.

brane as a function of temperature using pure He or CO₂ as the sweep gas. The dual-phase membranes prepared by the one-pot method have better performances than those prepared by powder mixing. This result clearly indicates that the uniformity of grain distribution for the dual-phase membrane is beneficial to improve the oxygen fluxes.^[5] Moreover, with our novel MIEC-MIEC composite strategy, the CGCO-LCF one-pot dual-phase membrane exhibits the highest oxygen permeability, while for the traditional CGO-LCF dual-phase membranes, the oxygen permeation fluxes are even slightly lower than that of the LCF single-phase membrane. The highest oxygen permeation fluxes of 0.87 and 0.70 mL min⁻¹ cm⁻² were obtained at 950 °C with pure He and CO₂ as the sweep gases, respectively. When pure CO₂ was taken as the sweep gas, the oxygen permeation fluxes were slightly decreased because of the inhibiting effect of CO₂ on the OSER.^[5]

Figure 5 shows the long-term oxygen permeation operation of CGCO-LCF one-pot dual-phase membrane at 800 °C and 900 °C. No decrease of the oxygen permeation fluxes was found during the test, thus indicating that the membrane is CO₂-stable.

In conclusion, for the first time we report an approach to obtain high and stable oxygen permeability of a novel dual-phase membrane. We also demonstrated stable oxygen permeation fluxes of the membrane in a CO₂ atmosphere even at lower-temperature (800 °C) operation. As the oxygen permeability of the membrane can be further improved by reducing the membrane thickness, such as fabricating hollow fibers,^[26] or coating MIEC materials on the membrane surface for the enlargement of OSER,^[21] it is therefore reasonable to foresee that our CGCO-LCF dual-phase membrane provides promising potential for practical applications.

Keywords: carbon dioxide · electronic conductors · ionic conductors · membranes · oxygen transport

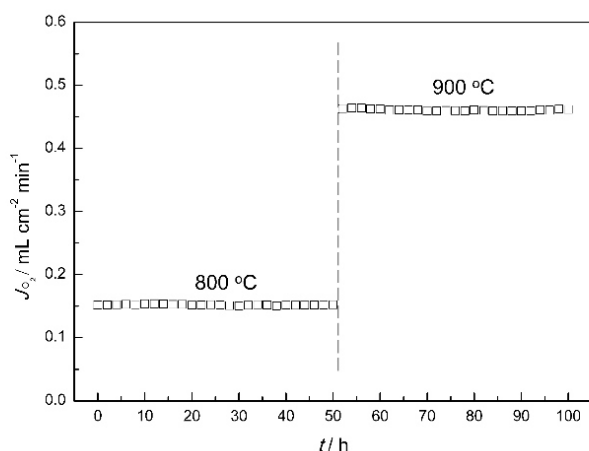


Figure 5. Long-term oxygen permeation operation through the CGCO-LCF one-pot dual-phase membrane. Conditions: 100 mL min^{-1} air as the feed gas, $30 \text{ mL min}^{-1} \text{ CO}_2$ as the sweep gas, membrane thickness: 0.5 mm .

How to cite: *Angew. Chem. Int. Ed.* **2015**, *54*, 4847–4850
Angew. Chem. **2015**, *127*, 4929–4932

- [1] A. Agüero, H. Falcon, J. M. C. Martín, S. M. A. Zahrani, J. L. G. Fierro, J. A. Alonso, *Angew. Chem. Int. Ed.* **2011**, *50*, 6557–6561; *Angew. Chem.* **2011**, *123*, 6687–6691.
- [2] J. Suntivich, H. A. Gasteiger, N. Yabuuchi, H. Nakanishi, J. B. Goodenough, Y. S. Horn, *Nat. Chem.* **2011**, *3*, 546–550.
- [3] Y. Liu, X. F. Zhu, M. R. Li, H. Y. Liu, Y. Cong, W. S. Yang, *Angew. Chem. Int. Ed.* **2013**, *52*, 3232–3236; *Angew. Chem.* **2013**, *125*, 3314–3318.
- [4] H. H. Wang, S. Werth, T. Schiestel, J. Caro, *Angew. Chem. Int. Ed.* **2005**, *44*, 6906–6909; *Angew. Chem.* **2005**, *117*, 7066–7069.
- [5] H. X. Luo, K. Efimov, H. Q. Jiang, A. Feldhoff, H. H. Wang, J. Caro, *Angew. Chem. Int. Ed.* **2011**, *50*, 759–763; *Angew. Chem.* **2011**, *123*, 785–789.
- [6] Z. W. Cao, H. Q. Jiang, H. X. Luo, S. Baumann, W. A. Meulenberg, J. Assmann, L. Mleczko, Y. Liu, J. Caro, *Angew. Chem. Int. Ed.* **2013**, *52*, 13794–13797; *Angew. Chem.* **2013**, *125*, 14039–14042.
- [7] Z. P. Shao, W. S. Yang, Y. Cong, H. Dong, J. H. Tong, G. X. Xiong, *J. Membr. Sci.* **2000**, *172*, 177–183.
- [8] Y. Teraoka, Y. Honbe, J. Ishii, H. Furukawa, I. Moriguchi, *Solid State Ionics* **2002**, *152–153*, 681–687.
- [9] Y. J. X. Yi, S. J. Feng, Y. B. Zuo, W. Liu, C. S. Chen, *Chem. Mater.* **2005**, *17*, 5856–5861.
- [10] K. Efimov, T. Klande, N. Juditzki, A. Feldhoff, *J. Membr. Sci.* **2012**, *389*, 205–215.
- [11] K. Schmale, M. Grünebaum, M. Janssen, S. Baumann, F. S. Küppers, H. D. Wiemhöfer, *Phys. Status Solidi B* **2011**, *248*, 314–322.
- [12] M. Mogensen, N. M. Sammes, G. A. Tompsett, *Solid State Ionics* **2000**, *129*, 63–94.
- [13] S. Banerjee, P. S. Devi, D. Topwal, S. Mandal, K. Menon, *Adv. Funct. Mater.* **2007**, *17*, 2847–2854.
- [14] C. Kleinlogel, L. J. Gauckler, *Adv. Mater.* **2001**, *13*, 1081–1085.
- [15] G. S. Lewis, A. Atkinson, B. C. H. Steele, J. Drennan, *Solid State Ionics* **2002**, *152–153*, 567–573.
- [16] S. Lübke, H. D. Wiemhöfer, *Solid State Ionics* **1999**, *117*, 229–243.
- [17] M. Balaguer, C. Solís, J. M. Serra, *Chem. Mater.* **2011**, *23*, 2333–2343.
- [18] V. V. Kharton, A. V. Kovalevsky, A. P. Viskup, F. M. Figueiredo, A. A. Yaremchenko, E. N. Naumovich, F. M. B. Marques, *J. Electrochem. Soc.* **2000**, *147*, 2814–2821.
- [19] V. V. Kharton, A. V. Kovalevsky, A. P. Viskup, A. L. Shaula, F. M. Figueiredo, E. N. Naumovich, F. M. B. Marques, *Solid State Ionics* **2003**, *160*, 247–258.
- [20] S. B. Adler, *Chem. Rev.* **2004**, *104*, 4791–4843.
- [21] J. H. Joo, K. S. Yun, Y. Lee, J. Jung, C. Y. Yoo, J. H. Yu, *Chem. Mater.* **2014**, *26*, 4387–4394.
- [22] M. Balaguer, J. G. Fayos, C. Solís, J. M. Serra, *Chem. Mater.* **2013**, *25*, 4986–4993.
- [23] R. D. Shannon, *Acta Crystallogr.* **1976**, *32*, 751–767.
- [24] X. F. Zhu, H. H. Wang, W. S. Yang, *J. Membr. Sci.* **2008**, *309*, 120–127.
- [25] P. S. Cho, S. B. Lee, Y. H. Cho, D. Y. Kim, H. M. Park, J. H. Lee, *J. Power Sources* **2008**, *183*, 518–523.
- [26] S. M. Liu, G. R. Gavalas, *J. Membr. Sci.* **2005**, *246*, 103–108.

Received: December 12, 2014

Published online: February 23, 2015



Supporting Information

A Mixed Ionic and Electronic Conducting Dual-Phase Membrane with High Oxygen Permeability**

Wei Fang, Fangyi Liang, Zhengwen Cao, Frank Steinbach, and Armin Feldhoff*

anie_201411963_sm_miscellaneous_information.pdf

1. Experimental details

1.1 Synthesis of powders and membranes

The $\text{Ce}_{0.9}\text{Gd}_{0.1}\text{O}_{2-\delta}$ (CGO), $\text{Ce}_{0.85}\text{Gd}_{0.1}\text{Cu}_{0.05}\text{O}_{2-\delta}$ (CGCO) and $\text{La}_{0.6}\text{Ca}_{0.4}\text{FeO}_{3-\delta}$ (LCF) single-phase powders were synthesized by the citric acid complexation-combustion method. The detailed description of the synthetic process can be found elsewhere.^[1] The CGO-LCF and CGCO-LCF dual-phase powders were prepared via a one-pot method.^[2] Briefly, the appropriate amounts of the metallic salts and citrate were dissolved in water and mixed in a beaker. After the water was evaporated, the resultant gel was combusted to remove the organic compounds, and then calcined in air at various temperatures. The CGO, CGCO and LCF powders were calcined at 950 °C for 10 h, and the CGO-LCF and CGCO-LCF one-pot powders at 1050 °C for 10 h. The CGO (CGCO) and LCF powders were also mixed in ethanol by magnetic stirring for 12 h, then dried overnight at 90 °C to form the mixed powders. All the powders were pressed into disks under a pressure of ~20 MPa. The dual-phase disks consist of 75 wt % CGO (CGCO) and 25 wt % LCF. The details of sintering temperatures for these disks are listed in Table S1. All the samples were heat treated for 10 h.

Table S1 Sintering conditions for CeO_2 -based and LCF disks.

disk	CGO-LCF one-pot	CGO-LCF mix	CGCO-LCF one-pot	CGCO-LCF mix	LCF	CGCO	CGO
sintering temperature (°C)	1350	1250	1150	1100	1250	1250	1550

All the sintered dual-phase membranes and the LCF single-phase membrane were polished by sandpapers to achieve a 0.5 mm thickness for oxygen permeation test. The sintered CGCO and CGO membranes were polished to 1 mm thickness, then cut into rectangular pieces for total conductivity test.

1.2 Measurements of total conductivity and impedance spectroscopy

Total conductivity measurements were conducted by standard four-point direct current (DC) technique.^[3] The measurements were carried out in a temperature range from 1000 °C to 600 °C by cooling down (1 °C/min) in ambient air. The constant current was

2.2 A novel concept of dual-phase membrane

supplied by a programmable current source (Keithley 2100) and the voltage drop through the sample was detected by a multimeter (another Keithley 2100). Two-point alternating-current impedance spectroscopy measurements were performed using a frequency response analyzer (Novocontrol Concept 41, Novocontrol, Germany) with an applied voltage of 0.1 V over a frequency range from 10^{-2} Hz to 10 MHz. Gold electrodes were used for all measurements. The measurements were made at the temperatures of 120 °C and 240 °C in N₂ atmosphere. The activation energy E_a for the conductivity was calculated by the following equation

$$\sigma T = A \exp(-E_a/kT) \quad (\text{Equation S1})$$

where A is a pre-exponential factor and k is the Boltzmann constant, σ and T denote the conductivity and temperature.

1.3 Characterization of membrane materials

The phase structures of the membrane materials were determined by X-ray diffraction (XRD, D8 Advance, Bruker-AXS, with Cu K α radiation) in the 2θ range 20-80° with a step width of 0.02°. For the in situ XRD tests in air and pure CO₂ atmospheres from 30°C to 1000°C, the samples were hold 30 min at each temperature before collecting the patterns, and the heating rate amounted to 12°C/min. The refinement of XRD data was performed by using TOPAS 4.2 software (Bruker AXS). Surface morphologies of the membranes were observed by back-scattered electron contrast (BSE, JEOL JSM-6700F) operated at 20 kV. The elemental distribution of the membrane surface was studied on the same electron microscope by energy dispersive X-ray spectroscopy (EDXS, Oxford INCA 300) at 20 kV. The CGCO-LCF one-pot dual-phase membrane was also investigated by transmission electron microscopy (TEM). Specimen was prepared by cutting, mechanical polishing and final Ar-ion sputtering. Investigations took place at incident electron energy of 200 kV in a JEOL JEM-2100F field-emission instrument. The microscope was equipped with a light-element energy-dispersive x-ray spectrometer (EDXS) of the type Oxford Instrument INCA 200 TEM. The microscope was operated as scanning TEM (STEM) and high-resolution TEM (HRTEM).

1.4 Measurements of oxygen permeation

The oxygen permeation was conducted in a home-made high-temperature oxygen permeation device,^[4] and a permeation cell was formed by sealing the disk membrane onto an alumina tube using a glass ring. The effective surface areas of the membranes were around 1.1 cm². Synthetic air (100 ml min⁻¹; 21 vol% O₂ and 79 vol% N₂) was applied as the feeding gas, and high purity helium (30 ml min⁻¹) or CO₂ (30 ml min⁻¹) as the sweep gas, respectively. The flow rates of the gases were controlled by mass flow controllers (Bronkhorst, Germany). The effluents on the sweep side were analyzed by an online-coupled gas chromatograph (Agilent 6890A). The flow rate of the effluents was measured by a bubble flow meter. The leakages of oxygen were no more than 5% for all the oxygen permeation tests and were subtracted when calculating the oxygen permeation fluxes.

2. Supporting figures and tables

2.1 XRD analysis of powders

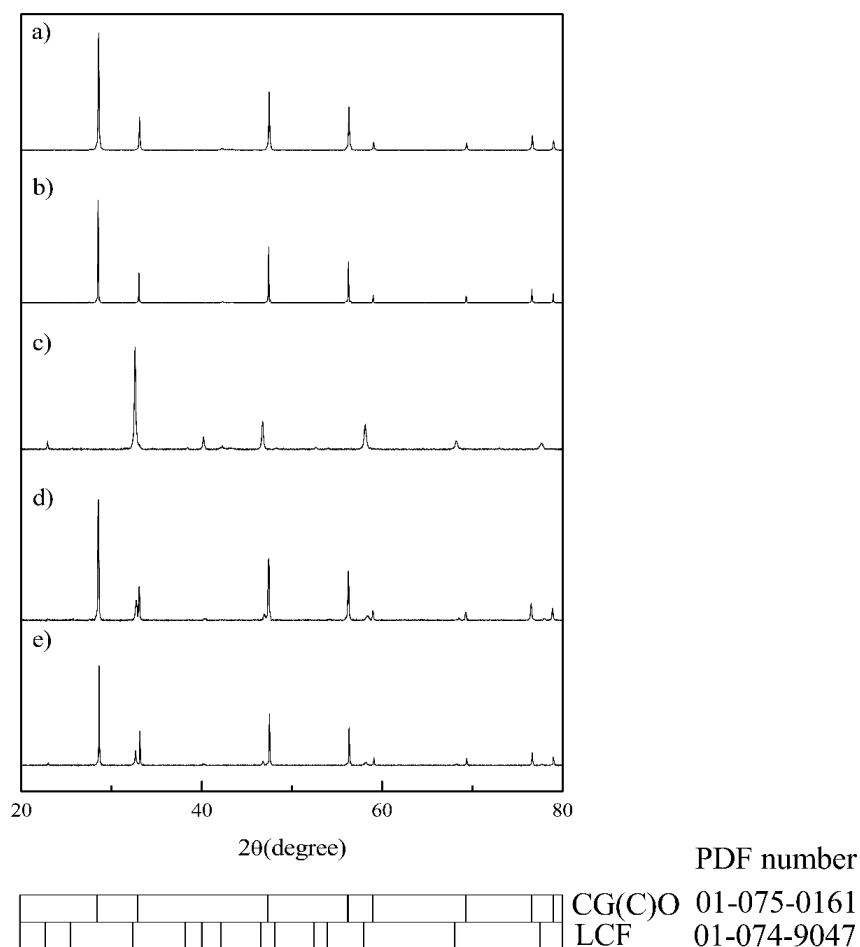
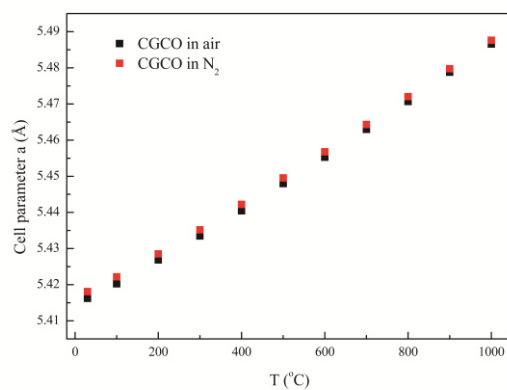


Figure S1 XRD pattern of single-phase and one-pot powders. a) CGO powder. b) CGCO powder. c) LCF powder. d) CGO-LCF one-pot powder. e) CGCO-LCF one-pot powder. Indication of PDF number at Bragg positions refers to the powders diffraction file database.

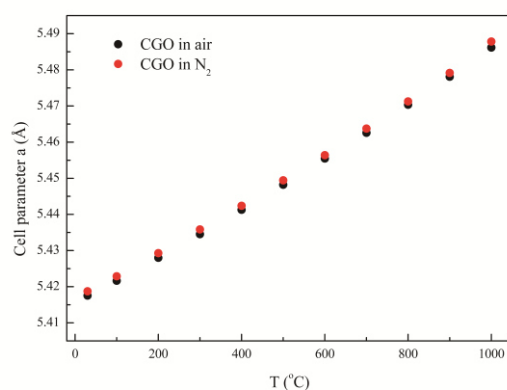
As shown in Figure S1, the X-ray diffraction patterns obtained for CGO (CGCO) and LCF can be indexed as a cubic fluorite structure and an orthorhombic perovskite structure respectively, and no impurity phases are detected for the one-pot dual-phase powders, which indicates that the two phases have good structural compatibility with each other.

2 Carbon dioxide tolerant dual-phase membranes

2.2 Thermal expansion coefficients of cell parameters for CGCO and CGO



(a)



(b)

Figure S2 Cubic cell parameters of a) CGCO and b) CGO as a function of temperature upon heating up in air and pure N₂ atmospheres.

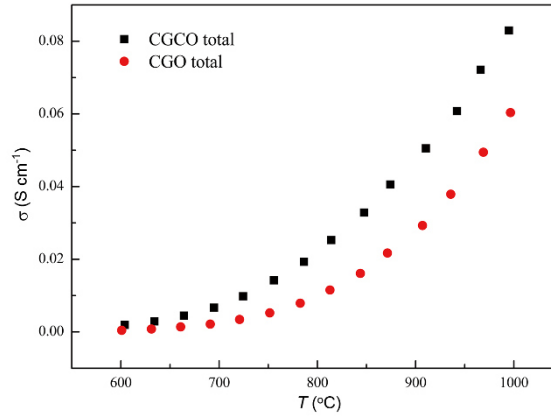
Both CGCO and CGO exhibit larger cell parameters in pure N₂ atmosphere compared with in air, which is due to the change of ionic radius of Ce and/or Cu (Figure S2).^[5]

The thermal expansion coefficients (TEC) of CGCO and CGO over the whole temperature range (30-1000°C) are summarized in Table S2.

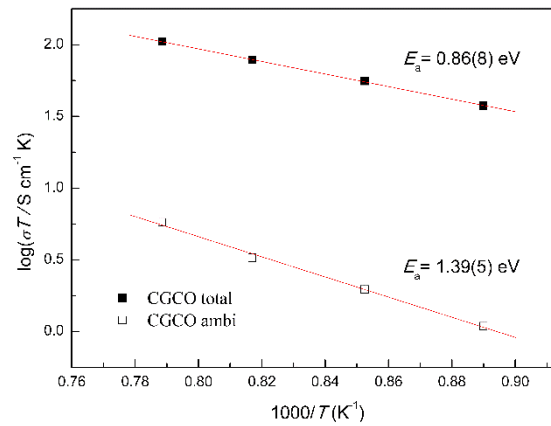
Table S2 TEC as estimated from cell parameters a and cell volume $V = a^3$ for CGCO and CGO.

	Atmosphere	TEC _a (10 ⁻⁶ K ⁻¹)	TEC _{volume} (10 ⁻⁶ K ⁻¹)
CGCO	air	13.5	40.7
	N ₂	13.3	40.2
CGO	air	12.9	39.7
	N ₂	13.1	39.9

2.3 Investigation of conductivity for CGCO and CGO



(a)



(b)

Figure S3 (a) The total conductivity in ambient air of CGO and CGCO as a function of temperature. (b) Arrhenius plots of the total conductivity and ambipolar conductivity for CGCO with indication of apparent activation energy (see Equation S1).

As depicted in Figure S3a, copper doping in CGO oxide has made a substantial improvement for the total conductivity.

The ambipolar conductivity is measured across a 1 mm thick membrane under a nominal oxygen partial pressure gradient of P_{O_2} $0.21/1 \times 10^{-3}$ atm (air/He), and calculated by the following equation (the oxygen bulk diffusion is the rate limiting

2 Carbon dioxide tolerant dual-phase membranes

step),^[6]

$$\sigma_{ambi} = \frac{16F^2 L J_{O_2}}{RT \ln \frac{P_i^{O_2}}{P_o^{O_2}}} \quad (\text{Equation S2})$$

where F as Faraday constant, R as the gas constant, L and T denote the membrane thickness and temperature respectively, and J_{O_2} is measured using gas chromatography analytical data. (e.g. for CGCO, at 1000°C, $J_{O_2} = 0.025 \text{ ml min}^{-1} \text{ cm}^{-2}$, $\sigma_{ambi} = 0.0046 \text{ S cm}^{-1}$.)

Usually, we conduct the thickness-dependent experiment to investigate the characteristic thickness (L_c), which is used for distinguishing the rate-limiting step of bulk diffusion and surface exchange.^[7] For pure CGCO membrane, with increasing

membrane thickness ($L \geq 1.5 \text{ mm}$), the leakage ($\text{Leakage} = \frac{C_{O_2, \text{leakage}}}{C_{O_2, \text{permeated}} + C_{O_2, \text{leakage}}}$)

increased rapidly due to the extremely low oxygen permeation fluxes, therefore the obtained data was somewhat unreliable. Hence, we also measured the CGCO membrane (1 mm thickness) coated with a porous CGCO layer, and no significant change for oxygen permeation fluxes was found, which indicates that the membrane is mainly controlled by bulk diffusion. For pure CGO membrane, oxygen permeability can be ignored.

Due to
$$\sigma_{total} = \sigma_i + \sigma_e \quad (\text{Equation S3}),^{[7]}$$

and
$$\sigma_{ambi} = \frac{\sigma_i \sigma_e}{\sigma_i + \sigma_e} \quad (\text{Equation S4}),^{[7]}$$

where i , e and $ambi$ denote the ionic, electronic and ambipolar, respectively.

For CGO, since the oxygen permeation fluxes can be neglected, it can be concluded that $\sigma_{ambi} \approx \sigma_e \approx 0$ and $\sigma_{total} \approx \sigma_i$; for CGCO, the ambipolar conductivity is one order of magnitude lower than the total conductivity, therefore $\sigma_{ambi} \approx \sigma_e > 0$ and $\sigma_{total} \approx \sigma_i$. The difference in the value of apparent activation energy for conductivity indicates different dominant mechanism of conduction (Figure S3b).

In conclusion, doping copper into CGO results in an improvement for the ionic and electronic conductivity.

2.4 Grain size distribution of CGCO and CGO

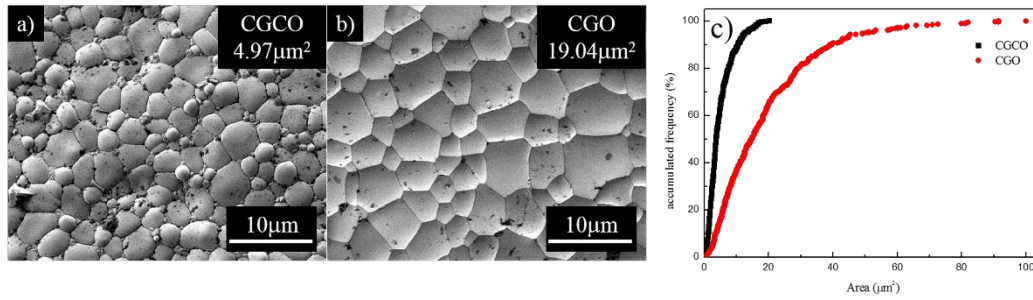


Figure S4 SE micrographs of sintered membranes with grain size distribution. a) CGCO surface (10h at 1250°C), b) CGO surface (10h at 1550°C), c) grain size distribution of CGCO and CGO.

Besides the concentration of the dopants, the microstructures of the doped-ceria ceramics also have a great influence on the conductivity.^[8] Adobe Photoshop CS3 and Image J were used as the image analysis software for the determination of the grain size distribution. The average grain size (total 500 grains) is about 4.97 μm^2 for CGCO, and 19.04 μm^2 for CGO (see Figure S4).

2.5 Impedance spectroscopy for CGCO and CGO

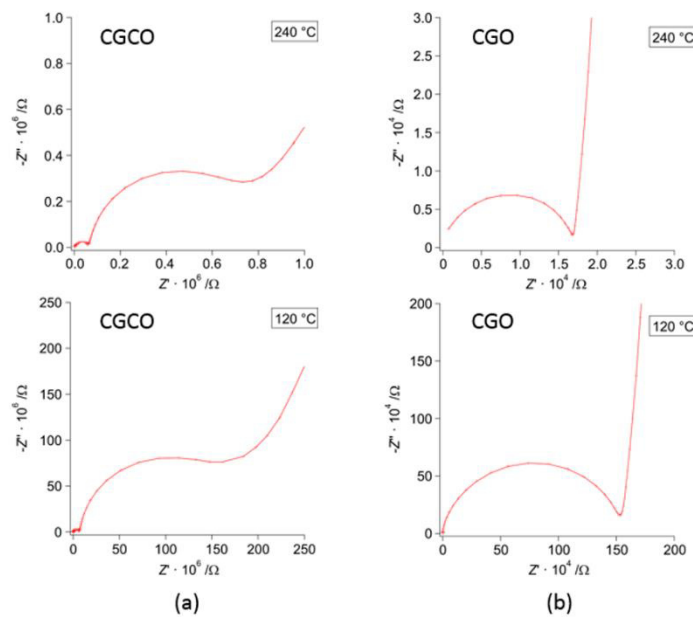


Figure S5 Complex impedance data obtained from CGCO and CGO samples at the temperatures of 120 °C and 240 °C in N_2 atmosphere.

2 Carbon dioxide tolerant dual-phase membranes

The impedance spectroscopy technique can be used to separate the relative contributions of the grain interior and grain boundary to the total resistance for doped-ceria ceramics.^[8,9] Figure S5 shows complex impedance plots obtained from CGCO and CGO samples at the temperature of 120 °C and 240 °C in N₂ atmosphere. For the CGCO sample, there are two arcs can be seen and well resolved in the complex impedance plots, which probably can be ascribed to the resistance of the grain interior and grain boundary, respectively (Figure S5a). For the CGO sample, only one arc can be observed which probably can be ascribed to the resistance of the grain interior (Figure S5b). One possible explanation is that for the CGO sample, the resistance of the grain boundary can be neglected due to the larger grain size (reducing the density of grain boundaries greatly, see Figure S4).^[8] It is also noticed that with increasing the measurement temperatures, the resistances of both grain interior and grain boundary decrease significantly. Unfortunately, we cannot conduct this impedance measurement at high temperature in air due to the limit of our equipment.

2.6 Phase structural stability of CGCO and LCF

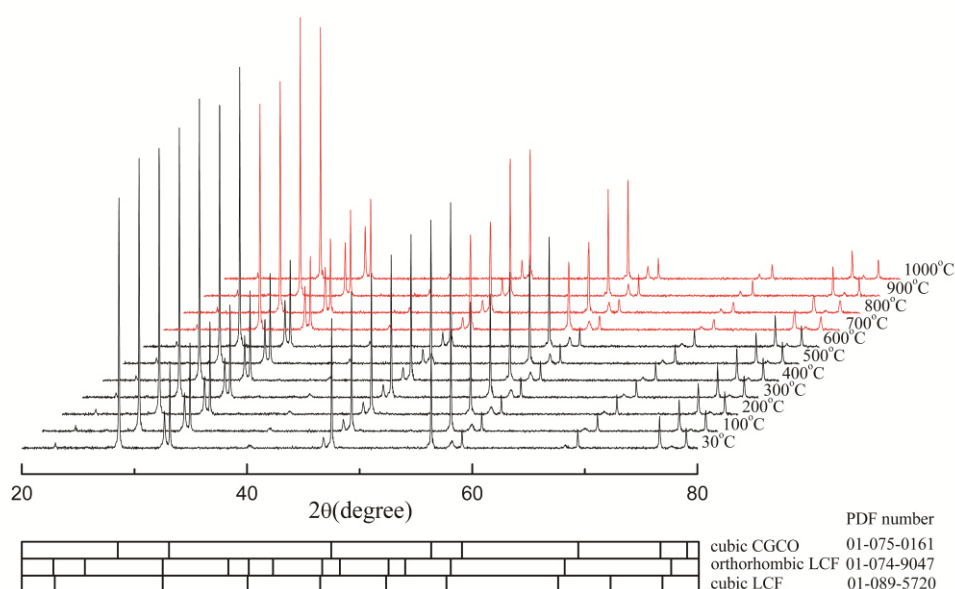


Figure S6 In situ XRD patterns of CGCO-LCF one-pot powder in air.

As shown in Figure S6, CGCO exhibits only cubic fluorite phase over the entire

9

2.2 A novel concept of dual-phase membrane

temperature range (cell parameters: see Figure S2a), while the symmetry of LCF perovskite phase changes from orthorhombic (30°C-600°C) to cubic (700°C-1000°C). The details of phase transition for LCF are listed in Table S3.

Table S3 Temperature-dependent lattice parameters of LCF. Z=number of formula units per unit cell, R_{exp} =expected reliability factor, R_{wp} =weighted profile reliability factor.

	T/°C	a/Å	b/Å	c/Å	V/Å ³	VZ ⁻¹ /Å ³	$R_{\text{exp}}/\%$	$R_{\text{wp}}/\%$
Orthorhombic phase Pnma Z=4	30	5.506	7.779	5.492	235.23	58.81	3.87	4.29
	100	5.510	7.785	5.495	235.74	58.93	3.83	4.32
	200	5.518	7.794	5.501	236.62	59.15	3.8	4.19
	300	5.527	7.804	5.508	237.55	59.39	3.79	4.18
	400	5.515	7.813	5.535	238.49	59.62	3.78	4.22
	500	5.522	7.823	5.542	239.40	59.85	3.77	4.22
Cubic phase Pm $\bar{3}$ m Z=1	600	5.528	7.830	5.553	240.36	60.09	3.77	4.22
	700	3.924			60.44		3.77	5.10
	800	3.930			60.72		3.77	5.02
	900	3.938			61.05		3.77	4.78
	1000	3.945			61.40		3.77	4.53

The volume thermal expansion coefficient (TEC) of LCF is $38.3 \times 10^{-6} \text{ K}^{-1}$ (30-600°C) and $52.9 \times 10^{-6} \text{ K}^{-1}$ (700-1000°C).

2.7 CO₂ stability of CGCO-LCF one-pot powder

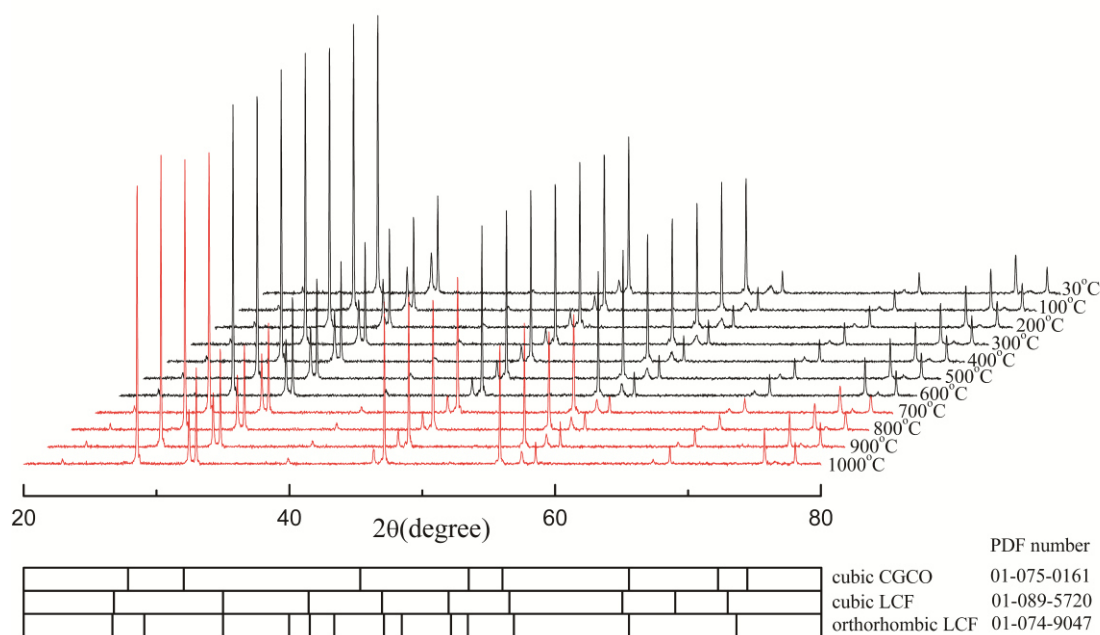


Figure S7 In situ XRD patterns of CGCO-LCF one-pot powder in pure CO₂.

2 Carbon dioxide tolerant dual-phase membranes

As shown in Figure S7, the one-pot powder retains its dual phases over the whole temperature range, and no carbonate formation could be detected.

In general, compared to rare-earth cations and transition-metal cations, alkaline-earth (AE) cations disfavor the CO₂ stability due to the high tendency of carbonate formation. The stability of AE cation-containing materials in the presence of CO₂ can be evaluated by using the Ellingham diagram.^[10] According to the Ellingham diagram, Ca-containing perovskites show better CO₂ tolerance because of the lower decomposition temperature (>900°C) for pure CaCO₃ under an atmospheric pressure of CO₂ (For SrCO₃: >1100°C).^[10] Moreover, the stabilization of the perovskite structure should be taken into consideration as well.^[11] The large negative stabilization energy of the Ca-containing perovskite leads to higher CO₂ stability. In addition, the reactivity of CO₂ over the surface of the perovskites would be slower at lower temperature.^[12] Therefore, the CGCO-LCF dual-phase materials show great tolerance toward CO₂.

2.8 SEM-EDXS analysis of the CGCO-LCF one-pot dual-phase membrane

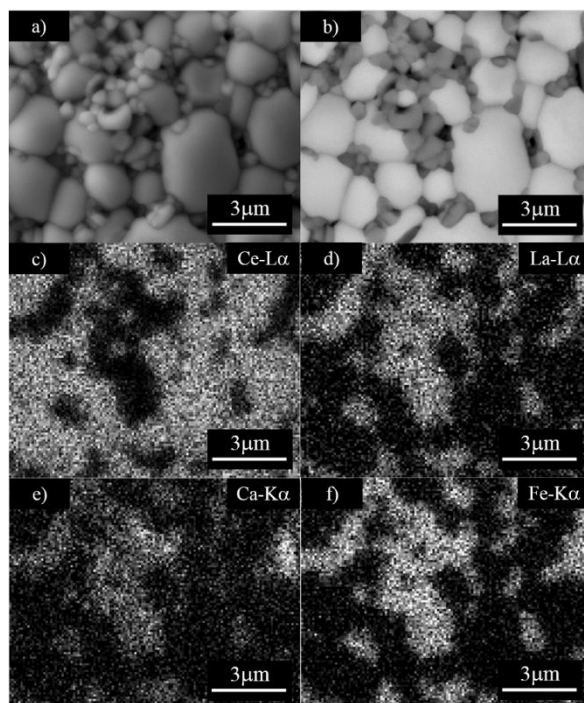


Figure S8 a) SE and b) BSE micrograph of the surface of CGCO-LCF one-pot dual-phase membrane. EDXS elemental distributions of c) Ce, d) La, e) Ca and f) Fe.

2.2 A novel concept of dual-phase membrane

As shown in Figure S8, SEM-EDXS results do not prove the presence of Cu and Gd in any preferential location.

2.9 STEM-EDXS analysis of the CGCO-LCF one-pot dual-phase membrane

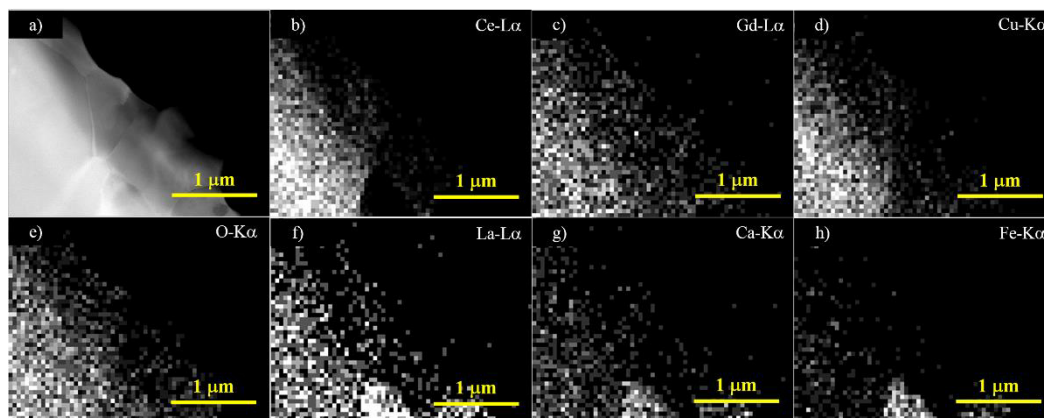


Figure S9 CGCO-LCF one-pot dual-phase membrane. a) STEM annular dark-field, EDXS elemental distributions of b) Ce, c) Gd, d) Cu, e) O, f) La, g) Ca and h) Fe.

As shown in Figure S9, STEM-EDXS results reveal that the presence of Cu and Gd in the sample, and the signals seem to be uniformly distributed, no obvious segregation could be found. Note that the copper signal may contain contributions from fluorescence due to narrow TEM pole piece and thus gives not the very true distribution in the material. Besides, EDXS is not a conclusive technique for elemental interdiffusion. Further investigations were done by EELS technique.

2.10 TEM analysis of the intergranular film between the CGCO grains in the CGCO-LCF one-pot dual-phase membrane

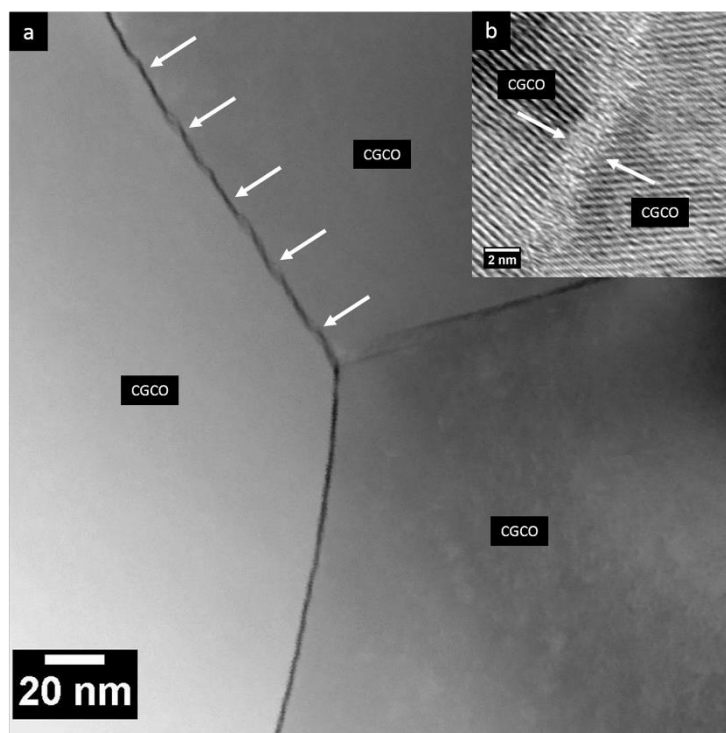


Figure S10 CGCO grains and grain boundaries. a) STEM annular dark-field, b) HRTEM of grain boundary between two CGCO grains.

The HRTEM micrograph shows the intergranular film with thickness of ca. 2 nm between two CGCO grains. Arrows in Figure S10b indicate locations of crystalline precipitates in intergranular film.

2.11 EELS analysis across the interface of CGCO-CGCO grains in the CGCO-LCF one-pot dual-phase membrane

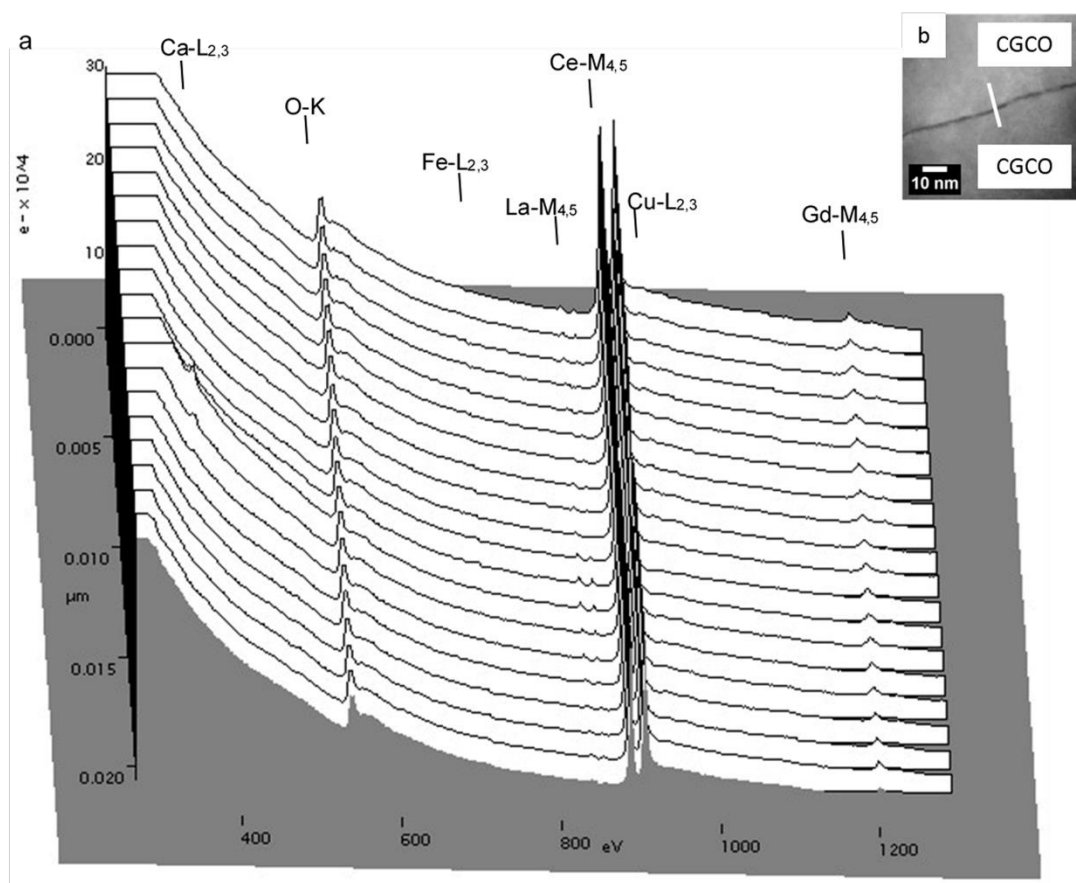


Figure S11 CGCO-LCF one-pot dual-phase membrane. a) Set of 20 EEL spectra acquired across grain boundary between two CGCO grains with point-to-point distance of 1.1 nm. The diameter of the electron beam was 1.5 nm. b) STEM annular dark-field with indication of scanned line of 22 nm in length.

Figure S11 shows the Ca-L_{2,3} ionization edge at 347 eV only in 4 spectra (4.4 nm spatial range) at grain boundary location. Note that these spectra exhibit also the Fe-L_{2,3} ionization edge at 710 eV as well as a pronounced La-M_{4,5} white line at 832 eV. These details can be seen clearly in the exemplary spectra, which are shown in Figure 3c. Away from the grain boundary no Ca or Fe could be detected by EELS. Note a small amount of La can be found in CGCO due to the interdiffusion by the one-pot synthesis.

2.12 EELS analysis across the interface of CGCO-LCF grains in the CGCO-LCF one-pot dual-phase membrane

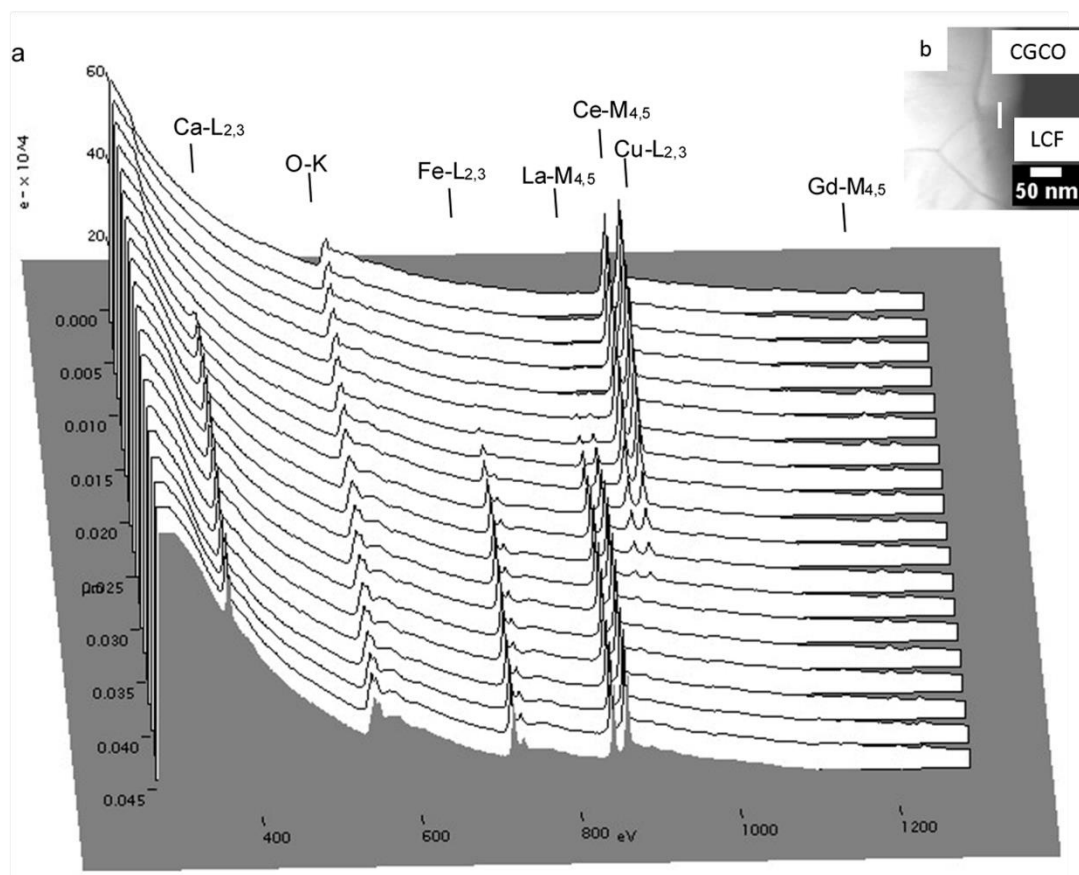


Figure S12 CGCO-LCF one-pot dual-phase membrane. a) Set of 20 EEL spectra acquired across grain boundary between the CGCO and LCF grains with point-to-point distance of 2.4 nm. The diameter of the electron beam was 1.5 nm. b) STEM annular dark-field with indication of scanned line of 48 nm in length.

Figure S12 shows the interdiffusion zone (about 8 spectra x 2.4 nm = 19.2 nm) at grain boundary (La extends into CGCO and Ce extend to LCF in nanometers depth, but Gd extends much more widely into the LCF).

2.13 The influence of sweep rate on the oxygen permeation fluxes

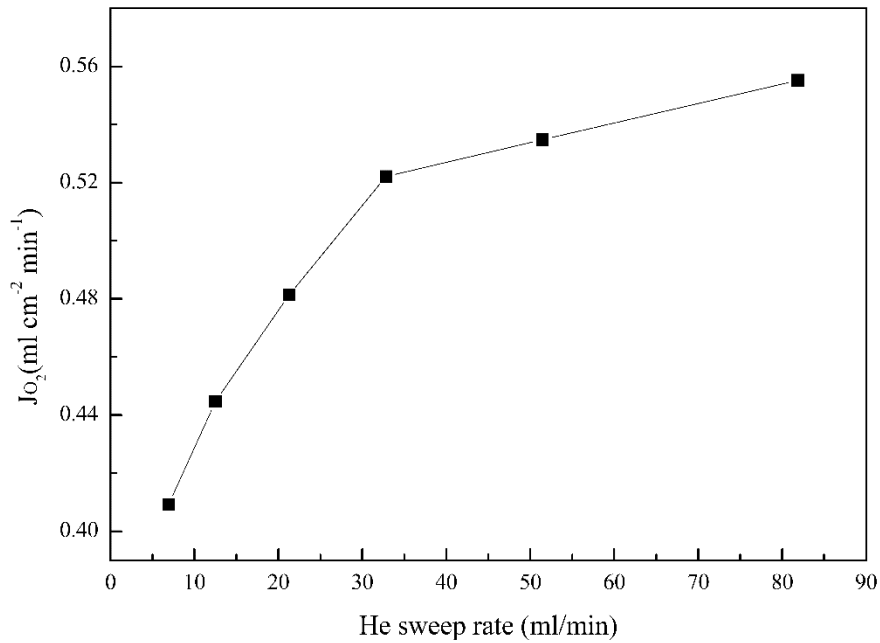


Figure S13 The influence of the He sweep rate on the oxygen permeation fluxes at 900°C . Feed side: 100 ml min^{-1} air.

The oxygen permeation fluxes increase with increasing the sweep rate of He due to larger oxygen partial pressure.

2.14 XRD analysis of tested membrane

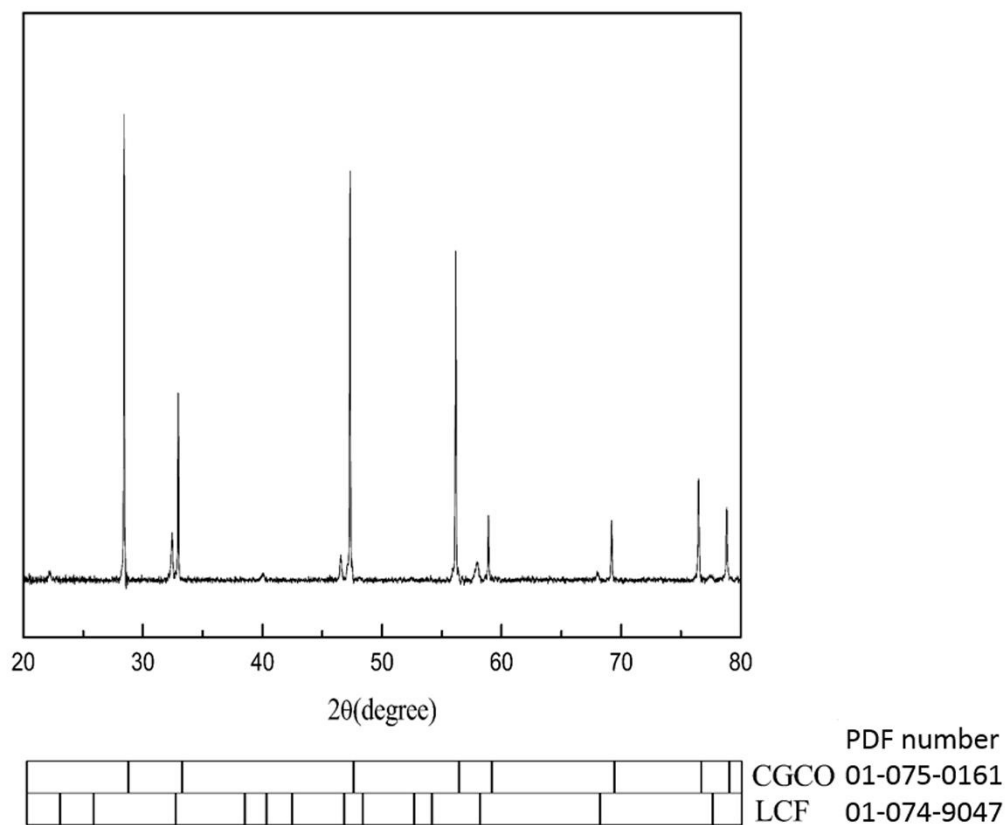


Figure S14 XRD pattern of the permeation-side surface of CGCO-LCF one-pot membrane after long-term oxygen permeation test using pure CO₂ as the sweep gas.

After the long-term oxygen permeation operation (more than 150 h), no carbonate formation was observed in the XRD pattern (Figure S14). The result is in agreement with in situ XRD and our previous study about LCF.^[10] The CGCO-LCF one-pot dual-phase membrane is stable in CO₂ atmosphere.

2.15 Summary of oxygen permeation fluxes of several OTMs

Table S4 Comparison of the oxygen permeation fluxes of several oxygen-transporting membranes (OTMs).

Membrane materials	Thickness (mm)	T (°C)	Oxygen flux (ml min ⁻¹ cm ⁻²)		Reference
			air/He	air/CO ₂	
Ba _{0.5} Sr _{0.5} Co _{0.8} Fe _{0.2} O _{3-δ} ^a	1	875	1.90	0	[13]
La _{0.4} Sr _{0.4} Co _{0.8} Fe _{0.2} O _{3-δ} ^a	1	900	/	0.10	[14]
60wt%Ce _{0.9} Gd _{0.1} O _{2-δ} - 40wt%NiFe ₂ O ₄ ^b	0.5	950	0.18	0.16	[15]
50vol%Ce _{0.9} Gd _{0.1} O _{2-δ} - 50vol%	1	950	0.20	/	[16]
La _{0.6} Sr _{0.4} Co _{0.2} Fe _{0.8} O _{3-δ} ^b					
60wt%Ce _{0.9} Nd _{0.1} O _{2-δ} - 40wt%Nd _{0.6} Sr _{0.4} FeO _{3-δ} ^a	0.6	950	0.26	0.21	[17]
60wt%Ce _{0.9} Nd _{0.1} O _{2-δ} - 40wt%Nd _{0.6} Sr _{0.4} FeO _{3-δ} ^b	0.6	950	/	0.48	[17]
75wt%Ce _{0.8} Sm _{0.2} O _{2-δ} - 25wt%	0.5	940	0.61	0.51	[18]
Sm _{0.8} Ca _{0.2} Mn _{0.5} Co _{0.5} O _{2-δ} ^b					
75wt%CGCO-25wt%LCF ^a	0.5	950	0.87	0.70	This work

^a The membrane uncoated with any porous layers.

^b The membrane coated with porous layers.

As described in Table S4, the conventional dual-phase membranes exhibit better CO₂ stability but low oxygen permeability compared to single-phase membranes. In order to obtain higher oxygen permeation fluxes, dual-phase membranes were commonly coated with mixed ionic-electronic conducting (MIEC) materials to improve the oxygen surface-exchange rate. In the present work, we successfully propose a novel MIEC-MIEC composite dual-phase membrane (CGCO-LCF) with considerable high oxygen permeation fluxes and excellent stability in the presence of CO₂, making it promising for practical applications. At last, let us summarize: There are mainly four reasons for the high permeability of our CGCO-LCF one-pot dual-phase membrane. Firstly, by Cu doping into CGO, it results in a significant improvement of ionic conductivity and electronic conductivity. Secondly, the special large grain size of CGCO in the dual-phase membrane leads to a great decrease of (ionic) grain boundary resistance (due to

reducing the density of grain boundaries). Thirdly, the new observed intergranular films (containing Ce, Ca, Gd, La and Fe) between the CGCO grains bring out a positive influence on the grain-boundary conduction. Fourth, the well percolation of two phases benefits the transport of oxygen-ions and electrons.

References

- [1] W. J. Shan, W. J. Shen, C. Li, *Chem. Mater.* **2003**, *15*, 4761-4767.
- [2] X. F. Zhu, H. H. Wang, W. S. Yang, *J. Membr. Sci.* **2008**, *309*, 120-127.
- [3] X. T. Wei, Y. S. Lin, *Solid State Ionics* **2008**, *178*, 1804-1810.
- [4] F. Y. Liang, H. X. Luo, K. Partovi, O. Ravkina, Z. W. Cao, Y. Liu, J. Caro, *Chem. Commun.* **2014**, *50*, 2451-2454.
- [5] R. D. Shannon, *Acta. Cryst.* **1976**, *32*, 751-767.
- [6] C. Wagner, *Prog. Solid State Chem.* **1975**, *10*, 3-16.
- [7] H. J. M. Bouwmeester, A. J. Burggraaf, Dense ceramic membranes for oxygen separation, A. J. Burggraaf, L. Cot (Eds.), *Fundamentals of Inorganic Membrane Science and Technology*, Elsevier Science B.V., Amsterdam, **1996**, pp. 435-528.
- [8] G. M. Christie, F.P.F. V. Berkel, *Solid State Ionics* **1996**, *83*, 17-27.
- [9] X. D. Zhou, W. Huebner, I. Kosacki, H. U. Anderson, *J. Am. Ceram. Soc.* **2002**, *85*, 1757-1762.
- [10] K. Efimov, T. Klande, N. Juditzki, A. Feldhoff, *J. Membr. Sci.* **2012**, *389*, 205-215.
- [11] H. Yokokawa, N. Sakai, T. Kawada, M. Dokiya, *Solid State Ionics* **1992**, *52*, 43-56.
- [12] A. Y. Yan, B. Liu, Y. L. Dong, Z. J. Tian, D. Z. Wang, M. J. Cheng, *Appl. Catal. B.* **2008**, *80*, 24-31.
- [13] M. Arnold, T. M. Gesing, J. Martynczuk, A. Feldhoff, *Chem. Mater.* **2008**, *20*, 5851-5858.
- [14] T. Klande, O. Ravkina, A. Feldhoff, *J. Membr. Sci.* **2013**, *437*, 122-130.
- [15] H. X. Luo, K. Efimov, H. Q. Jiang, A. Feldhoff, H. H. Wang, J. Caro, *Angew. Chem., Int. Ed.* **2011**, *50*, 759-763.
- [16] J. H. Joo, G. S. Park, C. Y. Yoo, J. H. Yu, *Solid State Ionics* **2013**, *253*, 64-69.
- [17] H. X. Luo, T. Klande, Z. W. Cao, F. Y. Liang, H. H. Wang, J. Caro, *J. Mater. Chem. A* **2014**, *2*, 7780-7787.
- [18] X. F. Zhu, H. Y. Liu, Y. Cong and W. S. Yang, *Chem. Commun.*, **2012**, *48*, 251-253.

2.3 An approach to enhance the CO₂ tolerance of fluorite-perovskite dual-phase oxygen-transporting membrane

Wei Fang,* Frank Steinbach, Chusheng Chen* and Armin Feldhoff

Chemistry of Materials 2015, 27, 7820-7826.

Reprinted (adapted) with permission from (Chemistry of Materials).

Copyright (2015) American Chemical Society.

An Approach To Enhance the CO₂ Tolerance of Fluorite–Perovskite Dual-Phase Oxygen-Transporting Membrane

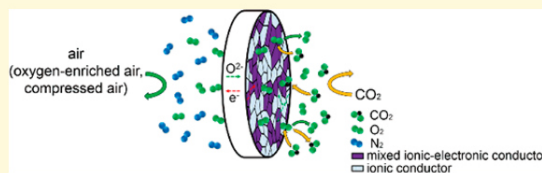
Wei Fang,^{*,†} Frank Steinbach,[†] Chusheng Chen,^{*,‡} and Armin Feldhoff[†]

[†]Institute of Physical Chemistry and Electrochemistry, Leibniz University Hannover, Callinstrasse 22, D-30167 Hannover, Germany

[‡]CAS Key Laboratory of Advanced Materials for Energy Conversion and Department of Materials Science and Engineering, University of Science and Technology of China, Hefei, Anhui 230026, PR China

Supporting Information

ABSTRACT: Most of the alkaline earth-containing perovskite-based oxygen-transporting membranes (OTMs) have insufficient tolerance toward CO₂ that potentially limits their commercial applications, for example, oxy-fuel combustion processes with CO₂ capture. One concern regarding the chemical potential of oxygen that may influence the CO₂ tolerance of perovskites, however, is lacking effective investigations. In the present work, we demonstrate that the approach to increase the chemical potential of oxygen at the feed side contributes to stabilize the oxygen permeation fluxes of the fluorite–perovskite dual-phase OTM under CO₂-rich atmosphere, and we further verify that oxygen can effectively act as a “buffer” to prevent the carbonate formation. Remarkably, we achieve high and stable oxygen permeation fluxes over 0.84 mL cm⁻² min⁻¹ during long-term operation at 900 °C with a 0.5 mm thickness 80 wt % Ce_{0.8}Gd_{0.15}Cu_{0.05}O_{2-δ}-20 wt % SrFeO_{3-δ} (CGCO-SFO, nominal composition) dual-phase membrane using oxygen-enriched air as the feed gas and pure CO₂ as the sweep gas.



INTRODUCTION

Complex perovskite oxides are promising candidates as catalysts,¹ fuel-cell electrodes,² and oxygen-transporting membranes (OTMs).³ Among the applications, perovskite membranes with fast transport of oxygen-ions at high temperatures have attracted increasing attention because these membranes can potentially be used for the production of pure oxygen,⁴ CO₂ capture integrated with oxy-fuel combustion,⁵ and catalytic membrane reactors.⁶ However, most perovskite materials for OTMs, such as SrCo_{0.8}Fe_{0.2}O_{3-δ} (SCF), suffer from large and irreversible performance losses in the presence of reactive gases (for example, CO₂) that limit their use.^{7,8} Another class of materials that offers high chemical stability and high ionic conductivity at elevated temperatures is doped ceria-based oxides with fluorite structure, such as Ce_{0.9}Gd_{0.1}O_{2-δ} (CGO).⁹ Unfortunately, the oxygen permeability of these membranes is very low due to the lack of electronic conductivity under oxidizing atmospheres.¹⁰ Therefore, dual-phase membranes made of a fluorite oxide (for example, CGO) for oxygen-ionic transport and a perovskite oxide (for example, La_{0.8}Sr_{0.2}Fe_{0.8}Co_{0.2}O_{3-δ}) for both oxygen-ionic and electronic transport have been extensively investigated.^{11–15} Compared to perovskite membranes,¹⁶ dual-phase membranes exhibit great chemical stability (for example, higher CO₂ tolerance and better reduction tolerance),^{17–19} which could enable them to be applicable as a promising candidate for industrial application.

In general, the stability of alkaline earth-containing materials in the presence of CO₂ can be evaluated by using the Ellingham diagram.²⁰ Although Ca-containing perovskites exhibit good tolerance toward CO₂, the main problem may be the formation

of secondary phases (for example, brownmillerite) during the materials preparation.²⁰ Therefore, a large amount of researchers still have focused much attention on Sr-containing perovskites. Besides, according to the Lewis base–acid theory, since CO₂ is an acidic gas, the basicity of the metal-containing perovskites (ABO₃ type) can also play an important role.²¹ Up to now, to develop the CO₂-tolerant OTMs, two main methods have been proposed. One way is to partially substitute the cations, such as replacing the A-site alkaline earth cations (for example, Sr²⁺) by lanthanide cations (for example, La³⁺),⁷ or the B-site elements (for example, Co/Fe) by the transition metal cations with high valence state and low basicity (for example, Ta⁵⁺ or Ti⁴⁺).^{21,22} However, these improvements are at the expense of a decrease in oxygen permeation fluxes.^{7,21} Another way, which is considered to be more favorable probably, is to fabricate the fluorite–perovskite dual-phase composite membranes.^{5,11–15,17–19} Unfortunately, for dual-phase OTMs, the observation of microstructure is quite insufficient, and the analysis of CO₂-tolerant mechanism is not clear. Recently, an interesting investigation has demonstrated that both CO₂ and O₂ can competitively adsorb on the perovskite surface.²³ Herein, we propose another possible factor related to the chemical potential of oxygen that appears to dramatically impact the CO₂ tolerance of perovskites. On the basis of these findings, we utilize a novel but remarkably effective approach that enables the stabilization of oxygen

Received: September 28, 2015

Revised: October 28, 2015

Published: October 28, 2015

Table 1. Comparison of the Oxygen Permeation Fluxes of Several Fluorite–Perovskite Dual-Phase OTMs under Air/He Gradient at 900 °C

nominal composition		thickness (mm)	oxygen flux (mL min ⁻¹ cm ⁻²)	reference
fluorite	perovskite			
60 vol % Ce _{0.8} Sm _{0.2} O _{2-δ}	40 vol % La _{0.8} Sr _{0.2} CrO _{3-δ} ^a	1	0.09	17
70 vol % Ce _{0.8} Sm _{0.2} O _{2-δ}	30 vol % La _{0.9} Sr _{0.1} FeO _{3-δ} ^a	1.1	0.15	18
60 wt % Ce _{0.9} Pr _{0.1} O _{2-δ}	40 wt % Pr _{0.6} Sr _{0.4} FeO _{3-δ} ^a	0.6	0.16	19
50 vol % Ce _{0.9} Gd _{0.1} O _{2-δ}	50 vol % La _{0.6} Sr _{0.4} Co _{0.2} Fe _{0.8} O _{3-δ} ^b	1	0.15	14
75 wt % Ce _{0.8} Sm _{0.2} O _{2-δ}	25 wt % Sm _{0.8} Ca _{0.2} Mn _{0.5} Co _{0.5} O _{3-δ} ^b	0.5	0.39	15
75 wt % Ce _{0.85} Gd _{0.15} Cu _{0.05} O _{2-δ}	25 wt % La _{0.6} Ca _{0.4} FeO _{3-δ} ^a	0.5	0.61	5
80 wt % Ce _{0.8} Gd _{0.15} Cu _{0.05} O _{2-δ}	20 wt % SrFeO _{3-δ} ^a	0.5	0.56	this work

^aThe membrane uncoated with any porous layers. ^bThe membrane coated with porous layers.

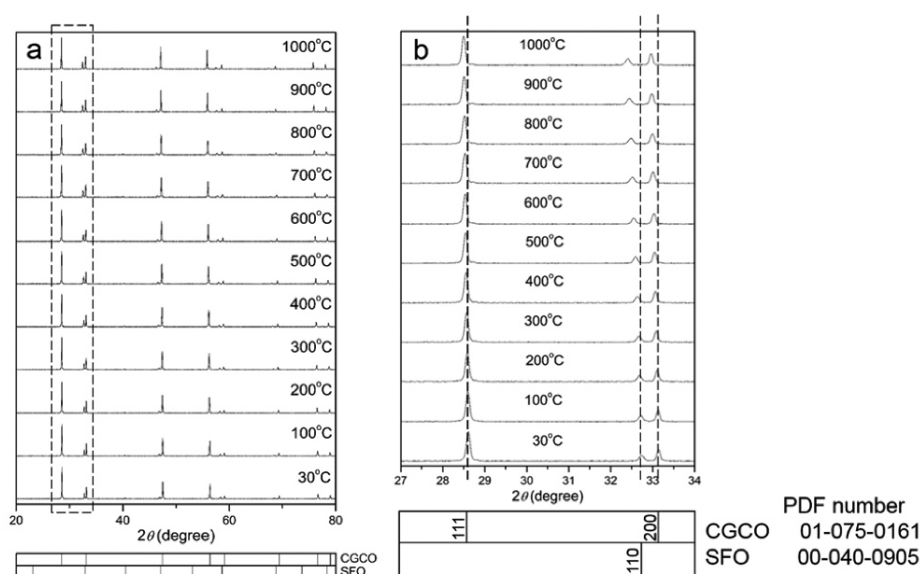


Figure 1. (a) In situ XRD patterns of CGCO-SFO one-pot dual-phase powder in air. (b) Close-up of the XRD patterns at $27^\circ \leq 2\theta \leq 34^\circ$.

permeation fluxes of a recently developed high-performance dual-phase membrane (Table 1) with nominal composition of 80 wt % Ce_{0.8}Gd_{0.15}Cu_{0.05}O_{2-δ} (CGCO)-20 wt % SrFeO_{3-δ} (SFO) in the presence of CO₂.

EXPERIMENTAL SECTION

Synthesis of Powders and Membranes. The Ce_{0.8}Gd_{0.15}Cu_{0.05}O_{2-δ}-SrFeO_{3-δ} (CGCO-SFO, nominal composition) dual-phase powder with a weight ratio of 80:20 (corresponding to a volume ratio of 76:24) was synthesized via a one-pot method.¹⁵ All the powders were calcined at 1100 °C for 10 h and then pressed into disks under a pressure of ~20 MPa. The disks were sintered at 1150 °C for 10 h and later slightly polished by sandpapers to achieve a 0.5 mm thickness for oxygen permeation test.

Characterization of Membrane Materials. The phase structures of the membrane materials were determined by X-ray diffraction (XRD, D8 Advance, Bruker-AXS, with Cu K α radiation) in the 2θ range 20–80° with a step width of 0.01°. For the in situ XRD tests in air from 30–1000 °C, the samples were hold 30 min at each temperature before the patterns were collected, and the heating rate amounted to 12 °C/min. The refinement of XRD data were performed by using TOPAS 4.2 software (Bruker AXS). Surface and cross-section morphologies of the membranes were observed by scanning electron microscopy (SEM, JEOL JSM-6700F) operated at 2–20 kV. The elemental distribution was studied on the same electron microscope by energy dispersive X-ray spectroscopy (EDXS, Oxford

INCA 300) at 15 kV. The CGCO-SFO dual-phase membrane was also investigated by transmission electron microscopy (TEM). Specimen was prepared by cutting, mechanical polishing, and final Ar-ion sputtering. Investigations took place at incident electron energy of 200 kV in a JEOL JEM-2100F field-emission instrument. The microscope was equipped with a light-element energy-dispersive X-ray spectrometer of the type Oxford Instrument INCA 200 TEM. The microscope was operated as scanning TEM (STEM) in high-angle annular dark-field (HAADF) mode including electron energy-loss (EEL) spectroscopy.

Measurements of Oxygen Permeation. The oxygen permeation was conducted in a homemade high-temperature oxygen permeation device,²⁴ and a permeation cell was formed by sealing the disk membrane onto an alumina tube using a commercial ceramic sealant (Huitian, Hubei, China). The effective surface areas of the membranes were around 0.45 cm². Synthetic air (100 mL min⁻¹; 21 vol % O₂ and 79 vol % N₂) or oxygen-enriched air (100 mL min⁻¹; 90 vol % O₂ and 10 vol % N₂) was applied as the feed gas, and high-purity helium (35 mL min⁻¹) or CO₂ (35 mL min⁻¹) as the sweep gas, respectively. The flow rates of the gases were controlled by mass flow controllers (Bronkhorst, Germany). The effluents on the sweep side were analyzed by an online-coupled gas chromatograph (Agilent 6890A). The absolute flow rates of the effluents were calculated using high-purity neon (1 mL min⁻¹) as an internal standardization. The leakages of oxygen were no more than 5% for all the oxygen permeation tests and were subtracted when calculating the oxygen permeation fluxes.

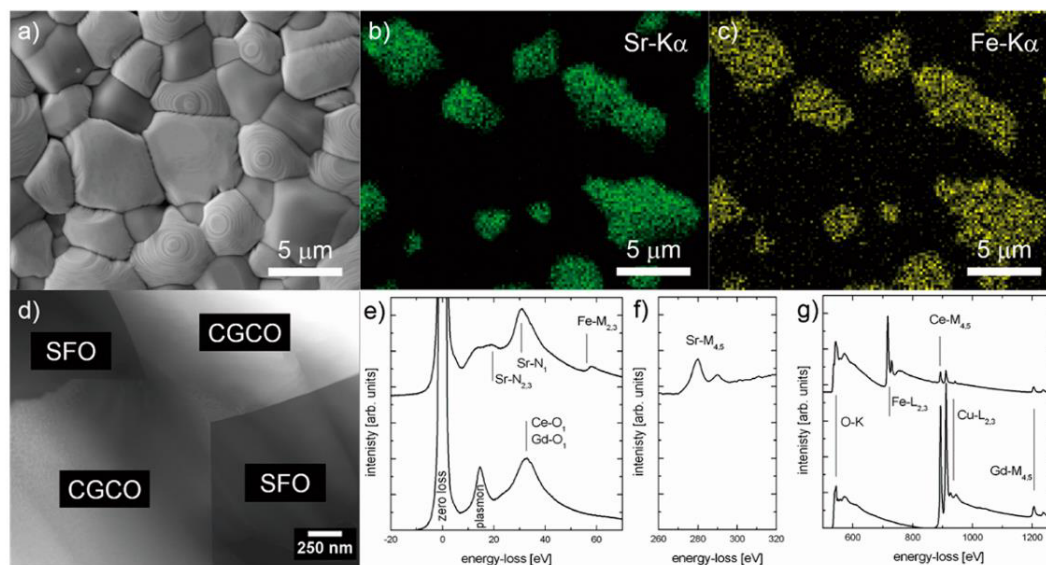


Figure 2. (a) Secondary electron micrograph of the surface of the sintered CGCO-SFO membrane. EDXS elemental distributions of (b) Sr and (c) Fe. (d) STEM-HAADF micrograph of CGCO/CGCO grain contact with two adjacent SFO grains. (e–g) EEL spectra of SFO (top) and CGCO (bottom) of different energy-loss regions: (e) low-loss, (f,g) core-loss.

RESULTS AND DISCUSSION

As-Sintered Ceramic. In situ XRD was used to characterize the crystalline structures and phase stability of the CGCO-SFO dual-phase materials in air. As shown in Figure 1, CGCO consists of a cubic fluorite phase with space group $Fm\bar{3}m$ ($a = 542.2$ pm), while SFO exhibits a cubic perovskite structure with space group $Pm\bar{3}m$ ($a = 387.9$ pm) at room temperature. Both phases remain unchanged with an increase in the temperature range from 30 to 1000 °C, and these results also suggest a good compatibility between the two phases.

Figure 2 displays the detailed investigation by SEM and STEM of the sintered CGCO-SFO dual-phase membrane. The information about the elemental distribution of the two phases is confirmed by EDXS images (Figures 2b,c and S2). Moreover, EEL spectra analysis of the sample demonstrates clearly the chemical nature of the perovskite phase and the fluorite phase, respectively (Figure 2e–g). The spectra for the CGCO grain show an O–K ionization edge at 534 eV as well as Ce- $M_{4,5}$ white lines at 884 eV and Gd- $M_{4,5}$ white lines at 1186 eV. It is also noticed that the white lines of Cu- $L_{2,3}$ at 931 eV can be observed, at the right of Ce- $M_{4,5}$ white lines at 884 eV. Meanwhile, the spectra for the SFO grain show Fe- $L_{2,3}$ white lines at 710 eV and a Sr- $M_{4,5}$ ionization edge at 269/280 eV. Note that the weaker white lines of Ce- $M_{4,5}$ at 884 eV, Cu- $L_{2,3}$ at 931 eV, and Gd- $M_{4,5}$ at 1186 eV can be found in the spectra for SFO as well, which indicates that a strong interdiffusion of metal cations from fluorite to perovskite phase took place during the one-pot synthesis process. In other words, most of Cu incorporates into the fluorite phase, while a minor amount of Ce, Gd, and Cu cations enter into the lattice of the perovskite phase, which can be expected from the ionic radii to some degree (Table 2). The interdiffused cations (Ce, Gd, Cu) can partially substitute the cations (Sr, Fe) in the SFO perovskite, and thus the configurational entropy of the perovskite will be increased. This is beneficial to the free enthalpy of formation for cubic perovskite, implying that it is

Table 2. Some Effective Ionic Radii According to Crystallographic Sites (X in an XO_2 Fluorite with Eight-Fold Coordination, while A and B in an ABO_3 Perovskite with 12-Fold and Six-Fold Coordination, Respectively).²⁵ For Fe^{3+} , the Electronic Spin Is Taken into Consideration by Giving Values for Low-Spin/High-Spin

phase	site	cation	coordination number	effective ionic radius (pm)
fluorite	X	Ce ⁴⁺	8	97
		Ce ³⁺	8	114.3
		Gd ³⁺	8	105.3
		Cu ²⁺	6	73
perovskite	A	Sr ²⁺	12	144
		Ce ³⁺	12	134
		Gd ³⁺	9	110.7
	B	Fe ⁴⁺	6	58.5
		Fe ³⁺	6	55/64.5

entropy-stabilized. A similar effect of the stabilization of the cubic structure by substitutions has been also observed in other perovskites.^{26,27} For our dual-phase OTM materials, to emphasize the main function of the each phase, that is, there is one (fluorite phase) for oxygen-ionic transport and another (perovskite phase) for electronic transport. Therefore, it is regarded that this interdiffusion of cations has probably no significant negative influence on the performance of the membrane.

Materials Resistance toward CO₂. To gain more insight into the CO₂ tolerance of OTMs, CGCO-SFO dual-phase ceramics were annealed at 900 °C under different atmospheres and studied by XRD (Figures 3 and S3). After annealing for 100 h in pure CO₂, formation of SrCO₃ can be detected at the surface of the ceramic. Besides, the main peak of cubic perovskite is found to be split as well, which could be attributed to the distortion of the perovskite structure in the sample.

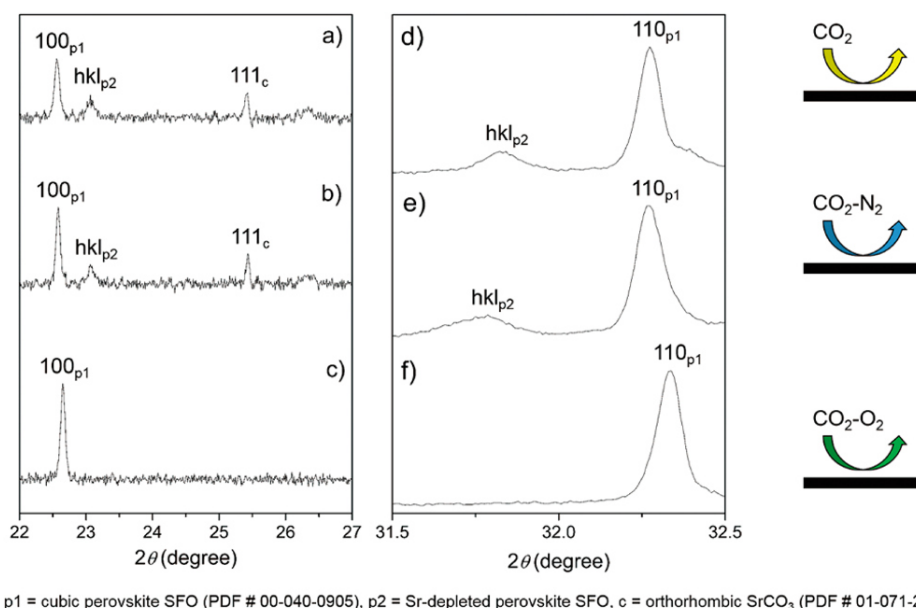


Figure 3. XRD patterns of CGCO-SFO ceramics annealed at 900 °C for 100 h under different atmospheres. (a,d) Pure CO₂, (b,e) 50 vol % CO₂-50 vol % N₂, (c,f) 50 vol % CO₂-50 vol % O₂. Close-up of the XRD patterns at (a–c) 22° ≤ 2θ ≤ 27° and (d–f) 31.5° ≤ 2θ ≤ 32.5°, respectively. Reflections of the whole angular range (20° ≤ 2θ ≤ 80°) of the XRD patterns can be found in Figure S3.

Combined with the appearance of new reflections at small angles, it suggests that a Sr-depleted perovskite phase with altered composition was formed during the annealing. Additionally, the residual reflections indexed as the fluorite phase remain unchanged, which exhibits great tolerance toward CO₂ (Figure S3). In the case of OTMs, it is also important to understand the interaction of perovskites with CO₂ and O₂. Therefore, we investigate another possible factor: O₂ partial pressure (p_{O_2}), which has not been paid much attention so far. We kept the p_{CO_2} at the same value 0.5 atm (balanced with N₂ or O₂ respectively) and increased the p_{O_2} from nearly zero to 0.5 atm. It is noticed that compared to annealing at the atmosphere of 50 vol % CO₂-50 vol % N₂, the cubic perovskite reflections remain unchanged in the presence of 50 vol % CO₂-50 vol % O₂, which may be due to the competitive adsorption of CO₂ and O₂ on the surface of perovskites.²³ Furthermore, the existence of O₂ reduces the oxygen vacancy concentration on the surface of perovskites, helps to stabilize the perovskite structure, and hinders the adsorption of CO₂ as well as the formation of carbonates.^{23,28}

On the basis of the above findings, oxygen permeation measurements were carried out to further investigate the chemical potential of oxygen as a potentially new factor for the CO₂ tolerance of the CGCO-SFO dual-phase membrane. In the present work, to obtain higher chemical potential of oxygen at the CO₂ sweep side, we applied the oxygen-enriched air instead of the synthetic air as the feed gas, which will be explained later. Figure 4 compares oxygen permeation behaviors of CGCO-SFO dual-phase membrane under different operation conditions at 900 °C. It can be seen that the oxygen permeation fluxes increase quickly with time at the initial stage, then much slower, and finally reach a relatively steady state (usually, He as the sweep gas). Similar phenomena were noticed in other dual-phase membranes, which can be explained as the readjusting of lattice structure from the as-prepared state

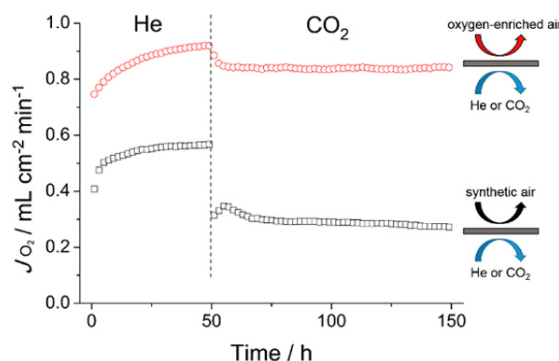


Figure 4. Oxygen permeation fluxes of CGCO-SFO membrane at 900 °C. Condition: 100 mL min⁻¹ synthetic air (21 vol % O₂-79 vol % N₂) or oxygen-enriched air (90 vol % O₂-10 vol % N₂) as the feed gas, respectively, 35 mL min⁻¹ He or CO₂ and 1 mL min⁻¹ Ne as the sweep gas, respectively; membrane thickness: 0.5 mm.

to the operated state.²⁹ It is more interesting to be noted that when using the synthetic air as the feed gas, after switching the sweep gas from He to CO₂, the oxygen permeation flux decreases sharply from 0.57 to 0.29 mL min⁻¹ cm⁻² (about 49% loss) at the beginning, then increases a little to 0.35 mL min⁻¹ cm⁻² after 5 h of operation, and finally drops gradually to 0.27 mL min⁻¹ cm⁻² during 95 h of operation. As a contrast, if using the oxygen-enriched air as the feed gas, after changing the sweep gas from He to CO₂, the oxygen permeation flux decreases slightly from 0.92 to 0.88 mL min⁻¹ cm⁻² (about only 4% loss) first, then drops a little to 0.84 mL min⁻¹ cm⁻² in the next 5 h of operation, but afterward maintains a stable performance (around 0.84 mL min⁻¹ cm⁻²) over more than 90 h of operation. Generally, it is thought that the adsorption of CO₂ can obviously degrade the oxygen surface-exchange rate, which leads to a significant drop of oxygen permeation fluxes at

the moment of altering the sweep gas,¹⁵ and later the continuous drop of oxygen fluxes may be ascribed to the formation of carbonates on the membrane surface. To further verify that carbonates were indeed responsible for the behaviors, the microstructures of both spent membranes were carefully investigated.

The surface morphologies of two spent CGCO-SFO dual-phase membranes are presented in Figure 5. For the membrane

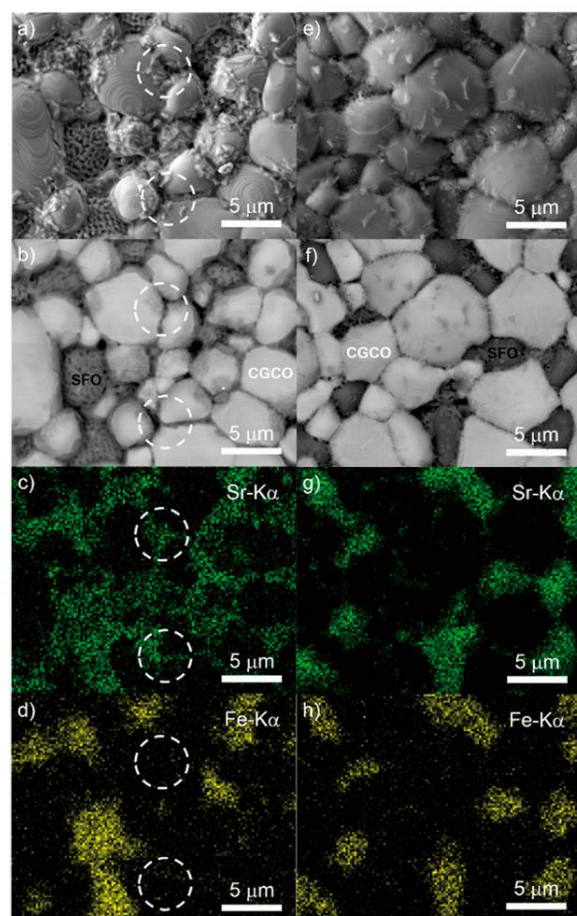


Figure 5. (a,e) Secondary electron and (b,f) backscattered electron micrographs of CO_2 -side surface of the spent CGCO-SFO membranes under different permeation conditions. EDXS elemental distributions of (c,g) Sr and (d,h) Fe. Condition: (a–d) synthetic air and (e–h) oxygen-enriched air as the feed gas, respectively.

fed by the synthetic air, after 100 h of operation at 900 °C, there are some remarkable changes on the morphology at the CO_2 side (Figure 5a,b) with the appearance of porous SFO grains and the segregation of SrCO_3 at all the grain boundaries (composition verified by EDXS, Figure 5c,d). In contrast, the morphology of the membrane fed by the oxygen-enriched air changes slightly with the detection of sparsely distributed small carbonate particles (Figure 5e,f). It is noted that the SFO grains are found to be nearly intact, and no obvious enrichment of SrCO_3 at the grain boundaries can be observed (Figure 5f–h). On the other hand, analysis of the fractured cross-sections of the spent dual-phase membranes enables an accurate estimation of the carbonate layer thickness (Figures 6 and S4). As

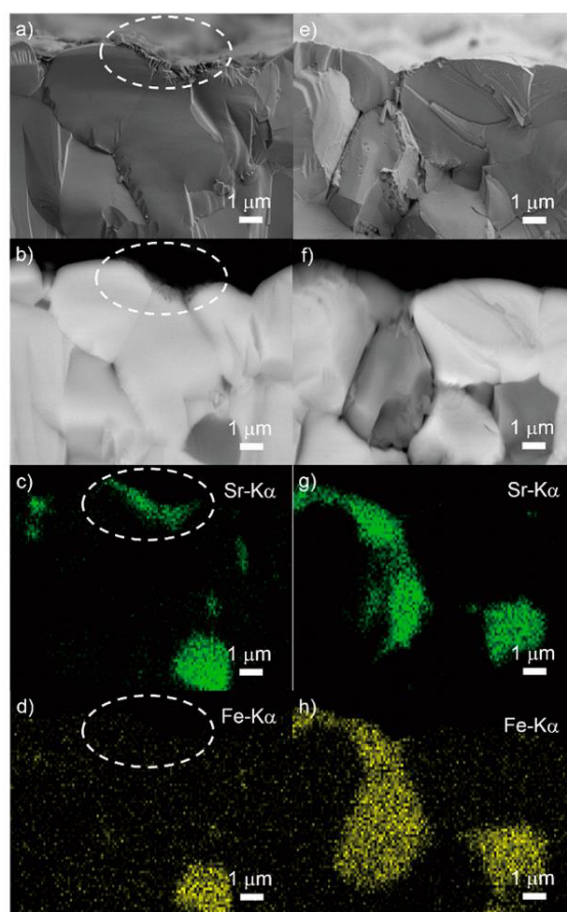


Figure 6. (a,e) Secondary electron and (b,f) backscattered electron micrographs of the fractured cross-section near CO_2 -side of the spent CGCO-SFO membranes under different permeation conditions. EDXS elemental distributions of (c,g) Sr and (d,h) Fe. Condition: (a–d) synthetic air and (e–h) oxygen-enriched air as the feed gas, respectively.

demonstrated in Figure 6, around hundreds of nanometers thick carbonate layers only can be observed at the grain boundaries for the membrane subjected to the synthetic air compared to the case of the oxygen-enriched air.

Since carbonates can easily block the transport of oxygen ions and electrons,³⁰ it is sufficient to cause a large decrease of the oxygen surface-exchange rate, followed by a rapid degradation of the permeation flux of the membrane during long-term operation. Furthermore, the location of SrCO_3 (around grain boundaries) indicates that CO_2 adsorbed easily at the grain boundary cores owing to the enrichment of oxygen vacancies.³¹ It is also reported that oxygen vacancies in the perovskite structure can contribute to the carbonate formation.²⁸ The formation of carbonates can be presumably divided into two stages: (1) the gradual adsorption of CO_2 depends on the collisions of CO_2 molecules with oxygen vacancies at the oxide surface; (2) the absorbed CO_2 reacts with oxygen lattice to form CO_3^{2-} ions, then it combines with mobile Sr^{2+} cations, and finally it transforms into thermodynamically stable SrCO_3 .²⁸ These findings, coupled with the fact that using the oxygen-enriched air instead of the synthetic air as

the feed gas can dramatically alleviate the formation of carbonates, strongly suggest that when the membrane is swept by CO₂, the migration of Sr²⁺ from SFO perovskite to the grain boundaries is driven by the chemical potential gradient of Sr²⁺; however, higher chemical potential of oxygen may effectively relieve this undesired migration due to the resistance to CO₂ adsorption. The probable mechanism is visualized in Figure 7.

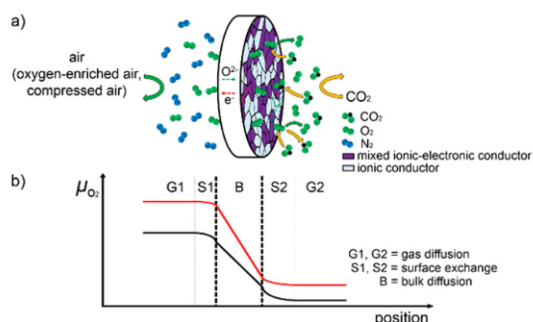


Figure 7. Schematic diagrams of (a) the competitive effect between oxygen desorption and CO₂ adsorption in the dual-phase OTM, and (b) variation of the chemical potential of oxygen as a function of the distance. The thick full lines represent the chemical potential profile (red, oxygen-enriched air; black, synthetic air). More details about the chemical potential of oxygen in the bulk of dual-phase OTM are discussed in Figure S5.

As illustrated in Figure 7, panel a, both releasing of oxygen and adsorbing of CO₂ take place at the gas–solid interface of the sweep side, and the gaseous molecule collision near the interface can be severe due to the reverse direction of gas diffusion. It is also noticed that only oxygen adsorption happens at the feed side. Hence, if the volume concentration of oxygen increases (using oxygen-enriched air to produce bigger oxygen concentration gradient across the membrane), more oxygen molecules can be inserted into the oxide lattice, then be transported through the OTM, and finally be released at the sweep side.³² Figure 7, panel b reveals that a drop in the chemical potential of oxygen (referred to as μ_{O_2}) occurs during the whole permeation process of the dual-phase OTM.³² Beside thermodynamics, the formation of carbonates is kinetically limited, thereby explaining why the membrane with higher chemical potential of oxygen possesses a lower carbonate content at the surface. At low μ_{O_2} , the adsorption of CO₂ at the sweep side is the dominant reaction of the surface exchange;²³ as a result, oxygen-impermeable carbonates are easy to generate at the membrane surface leading to the degradation of the permeation flux. At higher μ_{O_2} , the adsorption of CO₂ can be suppressed significantly due to the faster releasing of O₂ and lower oxygen vacancy concentration on the membrane surface;²³ consequently, fewer carbonates can be found, and no degradation of the permeation flux is observed. It is likely that the mechanism proposed above could be widely spread to other alkaline-earth containing OTMs.

CONCLUSIONS

In summary, for the first time, we report a novel approach to obtain high and stable oxygen permeation fluxes under CO₂-rich atmosphere for fluorite–perovskite dual-phase OTM. This achievement identifies that higher chemical potential of oxygen

is more beneficial to the CO₂ tolerance of OTMs. It is therefore reasonable to foresee that commercially significant fluxes (>5 mL cm⁻² min⁻¹) might be achieved by applying the compressed air (to gain higher chemical potential of oxygen) to the dual-phase membranes with asymmetric structure,^{33–37} and the success in stabilization of oxygen fluxes in the presence of CO₂ will boost many industrial applications of OTMs.

ASSOCIATED CONTENT

Supporting Information

The Supporting Information is available free of charge on the ACS Publications website at DOI: 10.1021/acs.chemmater.5b03823.

XRD patterns, SEM images, STEM images, EDXS images, cell parameters, theoretical data of local oxygen chemical potential (PDF)

AUTHOR INFORMATION

Corresponding Authors

*E-mail: wei.fang@pci.uni-hannover.de.

*E-mail: ccsm@ustc.edu.cn.

Notes

The authors declare no competing financial interest.

ACKNOWLEDGMENTS

This work has been supported by German Research Foundation (DFG) (No. FE928/7-1). The authors thank Prof. F. Y. Liang and Prof. J. X. Yi for productive discussions. We also acknowledge Y. L. Wang, Y. Y. Wei, and A. Schulz for technical support.

REFERENCES

- Suntivich, J.; May, K. J.; Gasteiger, H. A.; Goodenough, J. B.; Shao-Horn, Y. A Perovskite Oxide Optimized for Oxygen Evolution Catalysis from Molecular Orbital Principles. *Science* **2011**, *334*, 1383–1385.
- Sengodan, S.; Choi, S.; Jun, A.; Shin, T. H.; Ju, Y. W.; Jeong, H. Y.; Shin, J.; Irvine, J. T. S.; Kim, G. Layered oxygen-deficient double perovskite as an efficient and stable anode for direct hydrocarbon solid oxide fuel cells. *Nat. Mater.* **2014**, *14*, 205–209.
- Kharton, V. V.; Yaremchenko, A. A.; Kovalevsky, A. V.; Viskup, A. P.; Naumovich, E. N.; Kerko, P. F. Perovskite-type oxides for high-temperature oxygen separation membranes. *J. Membr. Sci.* **1999**, *163*, 307–317.
- Schlehuber, D.; Wessel, E.; Singheiser, L.; Markus, T. Long-term operation of a La_{0.58}Sr_{0.4}Co_{0.2}Fe_{0.8}O_{3-δ} membrane for oxygen separation. *J. Membr. Sci.* **2010**, *351*, 16–20.
- Fang, W.; Liang, F. Y.; Cao, Z. W.; Steinbach, F.; Feldhoff, A. A Mixed Ionic and Electronic Conducting Dual-Phase Membrane with High Oxygen Permeability. *Angew. Chem., Int. Ed.* **2015**, *54*, 4847–4850.
- Balachandran, U.; Dusek, J. T.; Mievil, R. L.; Poeppel, R. B.; Kleefisch, M. S.; Pei, S.; Kobylinski, T. P.; Udovich, C. A.; Bose, A. C. Dense ceramic membranes for partial oxidation of methane to syngas. *Appl. Catal., A* **1995**, *133*, 19–29.
- Klande, T.; Ravkina, O.; Feldhoff, A. Effect of A-site lanthanum doping on the CO₂ tolerance of SrCo_{0.8}Fe_{0.2}O_{3-δ} oxygen-transporting membranes. *J. Membr. Sci.* **2013**, *437*, 122–130.
- Kaus, I.; Wiik, K.; et al. Stability of SrFeO₃-Based Materials in H₂O/CO₂-Containing Atmospheres at High Temperatures and Pressures. *J. Am. Ceram. Soc.* **2007**, *90*, 2226–2230.
- Balaguer, M.; Solís, C.; Serra, J. M. Structural-Transport Properties Relationships on Ce_{1-x}Ln_xO_{2-δ} System (Ln = Gd, La, Tb, Pr, Eu, Er, Yb, Nd) and Effect of Cobalt Addition. *J. Phys. Chem. C* **2012**, *116*, 7975–7982.

- (10) Balaguer, M.; Solís, C.; Serra, J. M. Study of the Transport Properties of the Mixed Ionic Electronic Conductor $Ce_{1-x}Tb_xO_{2-\delta} + Co$ ($x = 0.1, 0.2$) and Evaluation As Oxygen-Transport Membrane. *Chem. Mater.* **2011**, *23*, 2333–2343.
- (11) Kharton, V. V.; Kovalevsky, A. V.; Viskup, A. P.; Shaula, A. L.; Figueiredo, F. M.; Naumovich, E. N.; Marques, F. M. B. Oxygen transport in $Ce_{0.8}Gd_{0.2}O_{2-\delta}$ -based composite membranes. *Solid State Ionics* **2003**, *160*, 247–258.
- (12) Samson, A. J.; Søgaard, M.; Vang Hendriksen, P. (Ce,Gd) $O_{2-\delta}$ -based dual phase membranes for oxygen separation. *J. Membr. Sci.* **2014**, *470*, 178–188.
- (13) Zhang, Z. B.; Zhou, W.; Chen, Y. B.; Chen, D. J.; Chen, J. W.; Liu, S. M.; Jin, W. Q.; Shao, Z. P. Novel Approach for Developing Dual-Phase Ceramic Membranes for Oxygen Separation through Beneficial Phase Reaction. *ACS Appl. Mater. Interfaces* **2015**, *7*, 22918–22926.
- (14) Joo, J. H.; Park, G. S.; Yoo, C. Y.; Yu, J. H. Contribution of the surface exchange kinetics to the oxygen transport properties in $Gd_{0.1}Ce_{0.9}O_{2-\delta}$ - $La_{0.6}Sr_{0.4}Co_{0.2}Fe_{0.8}O_{3-\delta}$ dual-phase membrane. *Solid State Ionics* **2013**, *253*, 64–69.
- (15) Zhu, X. F.; Liu, H. Y.; Cong, Y.; Yang, W. S. Novel dual-phase membranes for CO_2 capture via an oxyfuel route. *Chem. Commun.* **2012**, *48*, 251–253.
- (16) Švarcová, S.; Wiik, K.; Tolchard, J.; Bouwmeester, H. J. M.; Grande, T. Structural instability of cubic perovskite $Ba_xSr_{1-x}Co_{1-y}Fe_yO_{3-\delta}$. *Solid State Ionics* **2008**, *178*, 1787–1791.
- (17) Yi, J. X.; Zuo, Y. B.; Liu, W.; Winnubst, L.; Chen, C. S. Oxygen permeation through a $Ce_{0.8}Sm_{0.2}O_{2-\delta}$ - $La_{0.8}Sr_{0.2}CrO_{3-\delta}$ dual-phase composite membrane. *J. Membr. Sci.* **2006**, *280*, 849–855.
- (18) Wang, Z. T.; Sun, W. P.; Zhu, Z. W.; Liu, T.; Liu, W. A Novel Cobalt-Free, CO_2 -Stable, and Reduction-Tolerant Dual-Phase Oxygen-Permeable Membrane. *ACS Appl. Mater. Interfaces* **2013**, *5*, 11038–11043.
- (19) Luo, H. X.; Jiang, H. Q.; Klande, T.; Cao, Z. W.; Liang, F. Y.; Wang, H. H.; Caro, J. Novel Cobalt-Free, Noble Metal-Free Oxygen-Permeable $40Pr_{0.6}Sr_{0.4}FeO_{3-\delta}$ - $60Ce_{0.9}Pr_{0.1}O_{2-\delta}$ Dual-Phase Membrane. *Chem. Mater.* **2012**, *24*, 2148–2154.
- (20) Efimov, K.; Klande, T.; Juditzki, N.; Feldhoff, A. Ca-containing CO_2 -tolerant perovskite materials for oxygen separation. *J. Membr. Sci.* **2012**, *389*, 205–215.
- (21) Chen, W.; Chen, C. S.; Winnubst, L. Ta-doped $SrCo_{0.8}Fe_{0.2}O_{3-\delta}$ membranes: Phase stability and oxygen permeation in CO_2 atmosphere. *Solid State Ionics* **2011**, *196*, 30–33.
- (22) Schulz, M.; Kriegel, R.; Kämpfer, A. Assessment of CO_2 stability and oxygen flux of oxygen permeable membranes. *J. Membr. Sci.* **2011**, *378*, 10–17.
- (23) Yan, A. Y.; Liu, B.; Dong, Y. L.; Tian, Z. J.; Wang, D. Z.; Cheng, M. J. A temperature programmed desorption investigation on the interaction of $Ba_{0.5}Sr_{0.5}Co_{0.8}Fe_{0.2}O_{3-\delta}$ perovskite oxides with CO_2 in the absence and presence of H_2O and O_2 . *Appl. Catal., B* **2008**, *80*, 24–31.
- (24) Wang, H. H.; Tablet, C.; Feldhoff, A.; Caro, J. Investigation of phase structure, sintering, and permeability of perovskite-type $Ba_{0.5}Sr_{0.5}Co_{0.8}Fe_{0.2}O_{3-\delta}$ membranes. *J. Membr. Sci.* **2005**, *262*, 20–26.
- (25) Shannon, R. D. Revised Effective Ionic Radii and Systematic Studies of Interatomic Distances in Halides and Chalcogenides. *Acta Crystallogr., Sect. A: Cryst. Phys., Diffraction, Theor. Gen. Crystallogr.* **1976**, *32*, 751–767.
- (26) Tanasescu, S.; Yang, Z.; Martynczuk, J.; Varazashvili, V.; Maxim, F.; Teodorescu, F.; Botea, A.; Totir, N.; Gauckler, L. J. Effects of A-site composition and oxygen nonstoichiometry on the thermodynamic stability of compounds in the Ba-Sr-Co-Fe-O system. *J. Solid State Chem.* **2013**, *200*, 354–362.
- (27) Navrotsky, A. Thermochemistry of Perovskite-related oxides with high oxidation states: Superconductors, sensors, fuel cell materials. *Pure Appl. Chem.* **1994**, *66*, 1759–1764.
- (28) Nomura, K.; Ujihira, Y.; Hayakawa, T.; Takehira, K. CO_2 absorption properties and characterization of perovskite oxides, (Ba,Ca) (Co,Fe) $O_{3-\delta}$. *Appl. Catal., A* **1996**, *137*, 25–36.
- (29) Zhu, X. F.; Yang, W. S. Composite membrane based on ionic conductor and mixed conductor for oxygen permeation. *AIChE J.* **2008**, *54*, 665–672.
- (30) Yi, J. X.; Schroeder, M.; Weirich, T.; Mayer, J. Behavior of $Ba(Co, Fe, Nb)O_{3-\delta}$ Perovskite in CO_2 -Containing Atmospheres: Degradation Mechanism and Materials Design. *Chem. Mater.* **2010**, *22*, 6246–6253.
- (31) Guo, X.; Waser, R. Electrical properties of the grain boundaries of oxygen ion conductors: Acceptor-doped zirconia and ceria. *Prog. Mater. Sci.* **2006**, *51*, 151–210.
- (32) Bouwmeester, H. J. M.; Burggraaf, A. J. Dense ceramic membranes for oxygen separation. *Membr. Sci. Technol. Ser.* **1996**, *4*, 435–528.
- (33) Baumann, S.; Serra, J. M.; Lobera, M. P.; Escolástico, S.; Schulze-Küppers, F.; Meulenberg, W. A. Ultrahigh oxygen permeation flux through supported $Ba_{0.5}Sr_{0.5}Co_{0.8}Fe_{0.2}O_{3-\delta}$ membranes. *J. Membr. Sci.* **2011**, *377*, 198–205.
- (34) Wu, Z. T.; Othman, N. H.; Zhang, G. R.; Liu, Z. K.; Jin, W. Q.; Li, K. Effects of fabrication processes on oxygen permeation of Nb_2O_5 -doped $SrCo_{0.8}Fe_{0.2}O_{3-\delta}$ micro-tubular membranes. *J. Membr. Sci.* **2013**, *442*, 1–7.
- (35) Etchegoyen, G.; Chartier, T.; Del-Gallo, P. An architectural approach to the oxygen permeability of a $La_{0.6}Sr_{0.4}Fe_{0.5}Ga_{0.1}O_{3-\delta}$ perovskite membrane. *J. Eur. Ceram. Soc.* **2006**, *26*, 2807–2815.
- (36) Vente, J. F.; Haije, W. G.; Rak, Z. S. Performance of functional perovskite membranes for oxygen production. *J. Membr. Sci.* **2006**, *276*, 178–184.
- (37) Huang, H.; Cheng, S. Y.; Gao, J. F.; Chen, C. S.; Yi, J. X. Phase-inversion tape-casting preparation and significant performance enhancement of $Ce_{0.9}Gd_{0.1}O_{1.95}$ - $La_{0.6}Sr_{0.4}Co_{0.2}Fe_{0.8}O_{3-\delta}$ dual-phase asymmetric membrane for oxygen separation. *Mater. Lett.* **2014**, *137*, 245–248.

Supporting information

An Approach to Enhance the CO₂ Tolerance of Fluorite-Perovskite Dual-Phase Oxygen-Transporting Membrane

Wei Fang,^{*a} Frank Steinbach,^a Chusheng Chen^{*b} and Armin Feldhoff^a

^a Institute of Physical Chemistry and Electrochemistry, Leibniz University Hannover, Callinstrasse 22, D-30167 Hannover, Germany. E-mail: wei.fang@pci.uni-hannover.de

^b CAS Key Laboratory of Advanced Materials for Energy Conversion and Department of Materials Science and Engineering, University of Science and Technology of China, Hefei, Anhui 230026, PR China. E-mail: ccsm@ustc.edu.cn

2 Carbon dioxide tolerant dual-phase membranes

As-sintered ceramic

As shown in Fig. S1, both $\text{Ce}_{0.8}\text{Gd}_{0.15}\text{Cu}_{0.05}\text{O}_{2-\delta}$ (CGCO) and $\text{SrFeO}_{3-\delta}$ (SFO) exhibit larger cell parameters with increasing the temperature. The lattice thermal expansion coefficients (TEC) of CGCO and SFO are $13.3 \times 10^{-6} \text{ K}^{-1}$ and $18.9 \times 10^{-6} \text{ K}^{-1}$ (30-1000 °C), respectively.

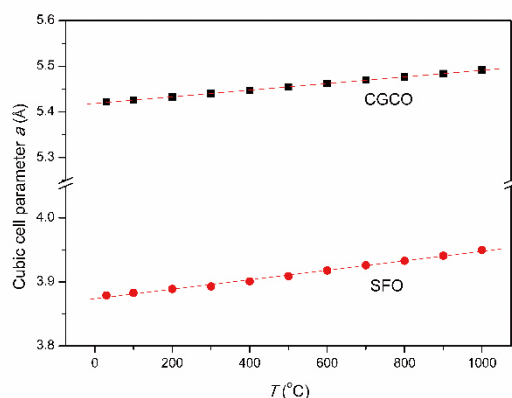


Fig. S1 Cubic cell parameters of CGCO and SFO in one-pot powders as a function of temperature upon heating up in air.

As shown in Fig. S2, STEM-EDXS results reveal the distribution of all the metal elements in the sample. It seems that Sr has the same distribution as Fe, while Ce, Gd and Cu exhibit another preferential distribution. Since EDXS is not a conclusive technique for elemental interdiffusion. Further investigations were done by EELS technique (Fig. 2). Note that no Sr-containing impurity phase was found at the grain boundary between two CGCO grains.

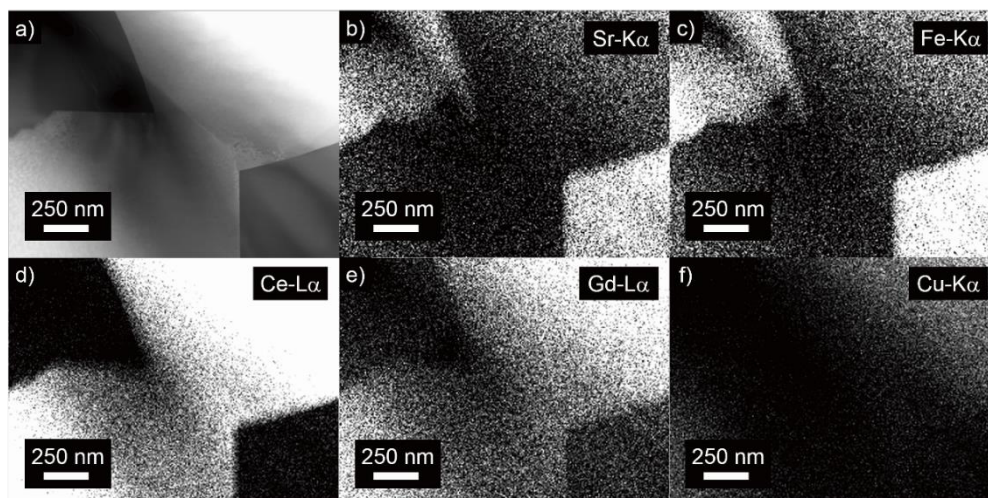


Fig. S2 The sintered CGCO-SFO dual-phase membrane. a) STEM annular dark-field, b-f) EDXS elemental distributions of b) Sr, c) Fe, d) Ce, e) Gd and f) Cu.

Materials resistance towards CO₂

As shown in Fig. S3, the weak X-ray reflection from the Sr-depleted perovskite SFO cannot be observed anymore under the oxidizing atmosphere. And the reflections from CGCO remain unchanged in all cases.

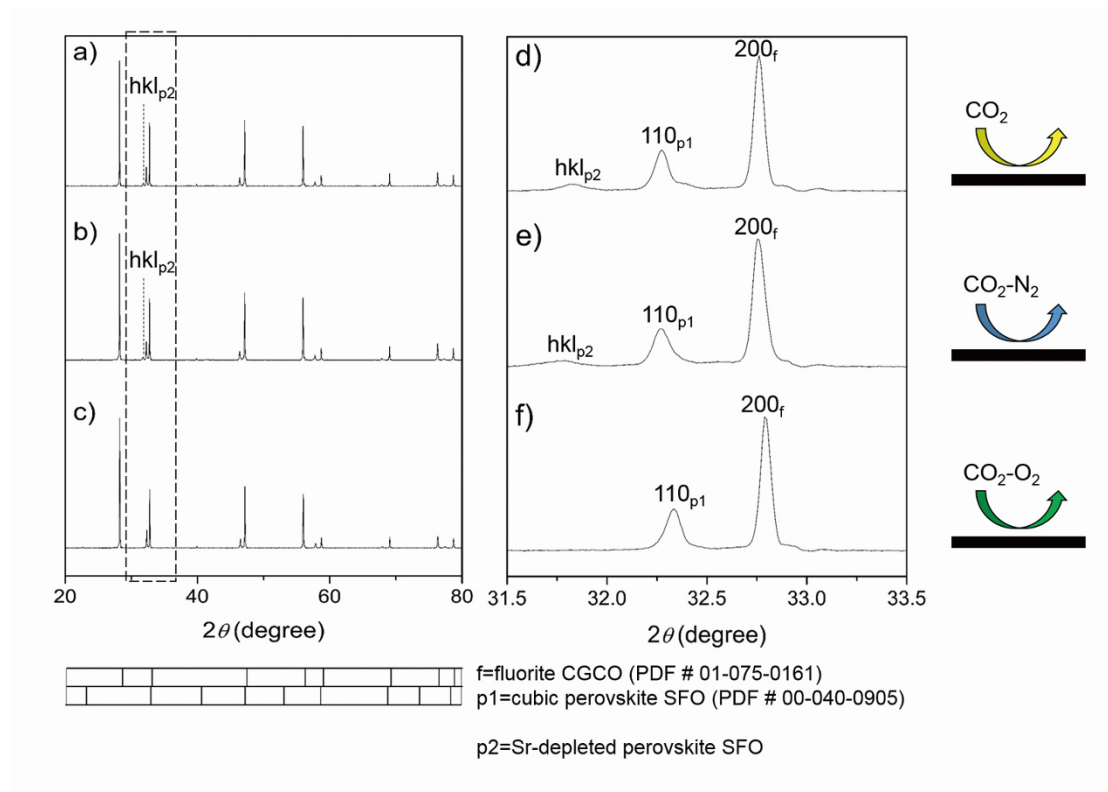


Fig. S3 XRD patterns for CGCO-SFO ceramics annealed at 900 °C for 100 h under different atmospheres. a,d) Pure CO₂. b,e) 50 vol.% CO₂-50 vol.% N₂. c,f) 50 vol.% CO₂-50 vol.% O₂. d-f) Close-up of the XRD patterns at 31.5° ≤ 2θ ≤ 33.5°.

2 Carbon dioxide tolerant dual-phase membranes

As shown in Fig. S4, it is noticed that carbonates (SrCO_3) segregated at the grain boundary of membrane surface which can be convinced by the distinguishing elemental distribution of Sr, Fe, C and O. In addition, the fluorite phase is confirmed by the distribution of Ce and O.

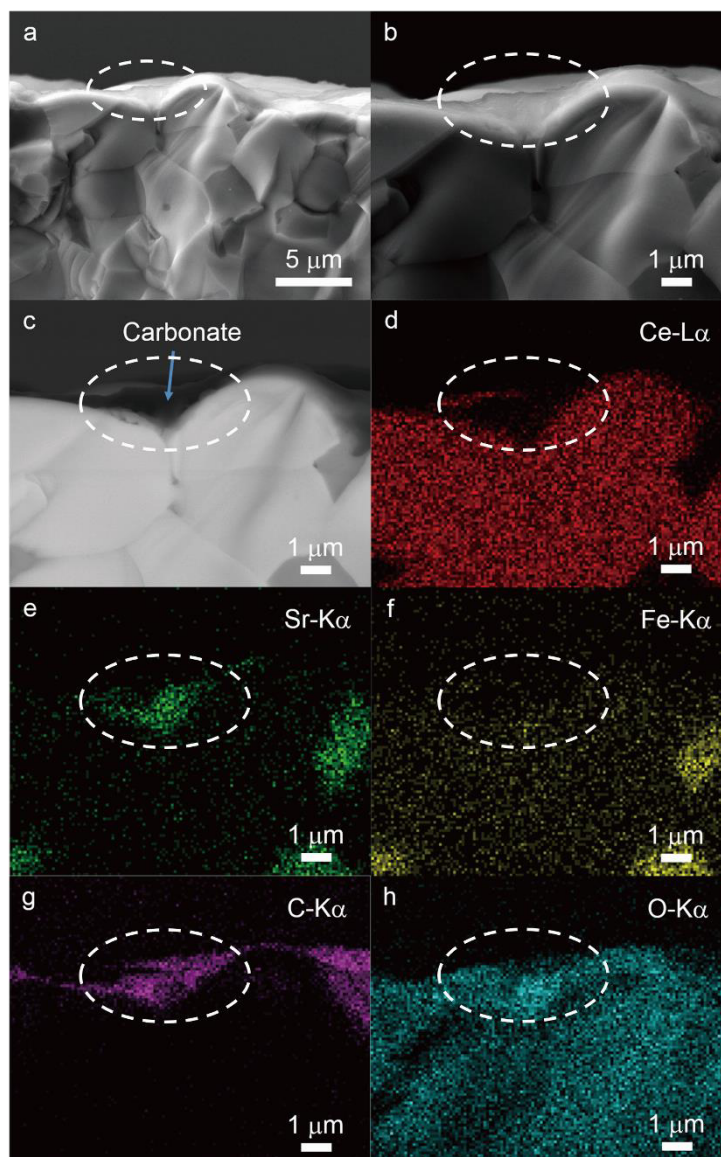


Fig. S4 a,b) Secondary electron and c) back-scattered electron micrographs of the fractured cross-section close to the sweep side of the spent CGCO-SFO dual-phase membrane after 100 h of operation at 900 °C. Condition: 100 mL min⁻¹ air as the feed gas, 35 mL min⁻¹ CO₂ and 1 mL min⁻¹ Ne as the sweep gas. EDXS elemental distributions of d) Ce, e) Sr, f) Fe, g) C and h) O.

2.3 A new approach for carbon dioxide tolerance

Estimation of local oxygen chemical potential

In the bulk of a mixed ionic and electronic conducting dual-phase oxygen-transporting membrane (OTM) with an oxygen partial pressure (p_{O_2}) gradient across it, oxygen ions and electrons (electron holes) move at the same time. The fluxes of oxygen ions, electrons and electron holes ($J_{O^{2-}}$, J_{e^-} and J_{h^+} , respectively) can be described as:^[S1]

$$J_{O^{2-}} = -\frac{\sigma_{O^{2-}}}{4F^2} \frac{\partial \mu_{O^{2-}}}{\partial x} + \frac{\sigma_{O^{2-}}}{2F} \frac{\partial \phi}{\partial x} \quad (\text{Equation S1})$$

$$J_{e^-} = -\frac{\sigma_{e^-}}{F^2} \frac{\partial \mu_{e^-}}{\partial x} + \frac{\sigma_{e^-}}{F} \frac{\partial \phi}{\partial x} \quad (\text{Equation S2})$$

$$J_{h^+} = -\frac{\sigma_{h^+}}{F^2} \frac{\partial \mu_{h^+}}{\partial x} - \frac{\sigma_{h^+}}{F} \frac{\partial \phi}{\partial x} \quad (\text{Equation S3})$$

$$\sigma_e = \sigma_{e^-} + \sigma_{h^+} \quad (\text{Equation S4})$$

where ϕ is the electrical potential, $\mu_{O^{2-}}$, μ_{e^-} and μ_{h^+} are the chemical potentials of oxygen ions, electrons and electron holes, respectively, and $\sigma_{O^{2-}}$ and σ_e are the oxygen-ionic and electronic conductivity, respectively. Besides at steady state, the following relations hold at equilibrium:^[S1]

$$2J_{O^{2-}} = J_{e^-} - J_{h^+} \quad (\text{Equation S5})$$

$$\frac{1}{2} \frac{\partial \mu_{O_2}}{\partial x} = \frac{\partial \mu_{O^{2-}}}{\partial x} - 2 \frac{\partial \mu_{e^-}}{\partial x} \quad (\text{Equation S6})$$

$$\frac{\partial \mu_{e^-}}{\partial x} = -\frac{\partial \mu_{h^+}}{\partial x} \quad (\text{Equation S7})$$

by combining Equation S1 to S7, the following equation is established:

$$J_{O^{2-}} = -\frac{1}{8F^2} \frac{\sigma_{O^{2-}} - \sigma_e}{\sigma_{O^{2-}} + \sigma_e} \frac{\partial \mu_{O_2}}{\partial x} \quad (\text{Equation S8})$$

This is the Wagner equation in another form.^[S1]

When the ionic and electronic conductivities can be assumed as:

$$\sigma_{O^{2-}} = \text{const} \quad (\text{Equation S9})$$

$$\sigma_e = \sigma_{el} p_{O_2}^n \quad (\text{Equation S10})$$

then oxygen partial pressure at a given position $p_{O_2}(x)$ in the bulk of OTM can be determined from the following equation:

$$\frac{x}{L} = \frac{\int_{\ln p_1}^{\ln p_{O_2}(x)} \frac{p_{O_2}^n}{\sigma_{O^{2-}} + \sigma_{el} p_{O_2}^n} d \ln p_{O_2}}{\int_{\ln p_1}^{\ln p_2} \frac{p_{O_2}^n}{\sigma_{O^{2-}} + \sigma_{el} p_{O_2}^n} d \ln p_{O_2}} \quad (\text{Equation S11})$$

where L is the thickness of OTM, n is index number, p_1 and p_2 are the oxygen

2 Carbon dioxide tolerant dual-phase membranes

partial pressures at the feed and sweep side respectively.

Usually, fluorite-type ionic conductors with negligible electronic conductivity exhibit pure ionic conductivity in a wide oxygen partial pressure range, for example $Zr_{0.84}Y_{0.16}O_{1.92}$ (YSZ) in the p_{O_2} region from 1 to 10^{-17} atm,^[S2] and $Ce_{0.9}Gd_{0.1}O_{1.95}$ (CGO) in the p_{O_2} region from 1 to 10^{-5} atm.^[S3] In addition, perovskites are widely used as the electronic conductor of the dual-phase OTM. For example, $SrFeO_{3-\delta}$ (SFO) shows p-type conductivity in the p_{O_2} range from 1 to 10^{-5} atm,^[S4] while $La_{0.7}Ca_{0.3}CrO_{3-\delta}$ (LCC) exhibits p-type conductivity in the p_{O_2} range from 1 to 10^{-21} atm.^[S5] In general, for OTMs, the electronic conductivity is at least 10 times higher than the ionic conductivity.^[S1] Therefore, we substituted $\sigma_{O^{2-}} = 0.1 \text{ S cm}^{-1}$, $\sigma_{el} = 1$ or 10 S cm^{-1} atm⁻¹, $n = 0.167, 0.25$ or 0.5 , $p_1 = 0.2$ or 0.9 atm , $p_2 = 0.005, 5 \times 10^{-9}$ or $5 \times 10^{-15} \text{ atm}$ into Equation S11, and finally obtained theoretical p_{O_2} profiles shown in Figure S5-S7.

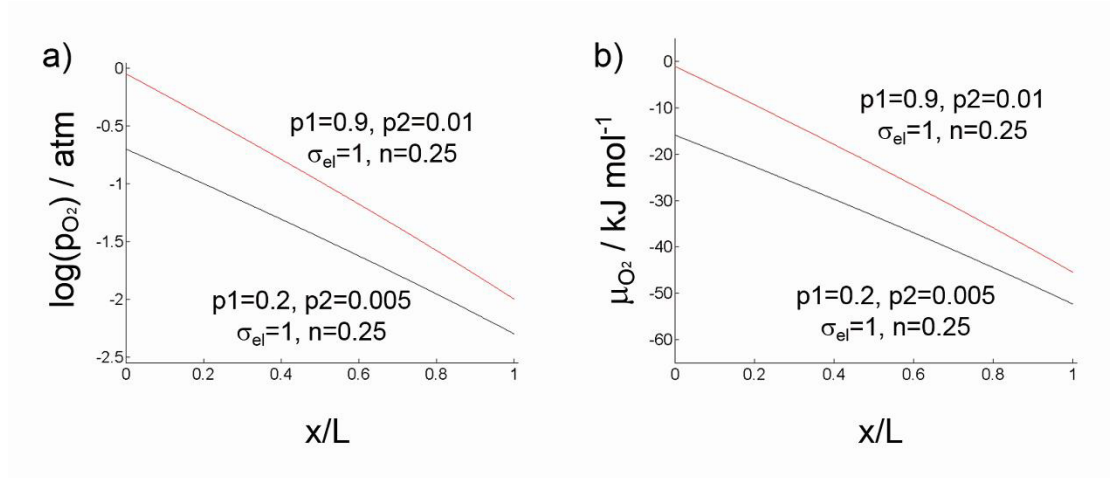


Fig. S5 Theoretical a) p_{O_2} and b) μ_{O_2} (1173 K) profiles in the dual-phase OTM located between synthetic air or oxygen-enriched air ($p_1 = 0.2$ or 0.9 atm) and inert gas ($p_2 = 0.005 \text{ atm}$).

The chemical potential of oxygen (μ_{O_2}) at 1173 K is calculated by the following equation:^[S6]

$$\mu_{O_2}(T, p) = \mu_{O_2}^\theta(T, p^\theta) + RT \ln \frac{p_{O_2}}{p_{O_2}^\theta} \quad (\text{Equation S12})$$

2.3 A new approach for carbon dioxide tolerance

Where $\mu_{O_2}^\theta$ and p^θ refer to standard conditions.

As shown in Fig. S6, it can be concluded that the electronic conductivity has little influence on the drop of p_{O_2} across the membrane with small p_{O_2} gradient (0.2~0.005 atm). The drop lines are nearly linear in all cases. This finding may indicate that whether coating porous layer on the feed or sweep side will benefit to oxygen permeation under small p_{O_2} gradient to the same degree, which is in agreement with the experiment results of $Ce_{0.85}Gd_{0.15}O_{1.925}-Sm_{0.6}Sr_{0.4}FeO_{3-\delta}$ dual-phase membranes coating with porous layers.^[S7]

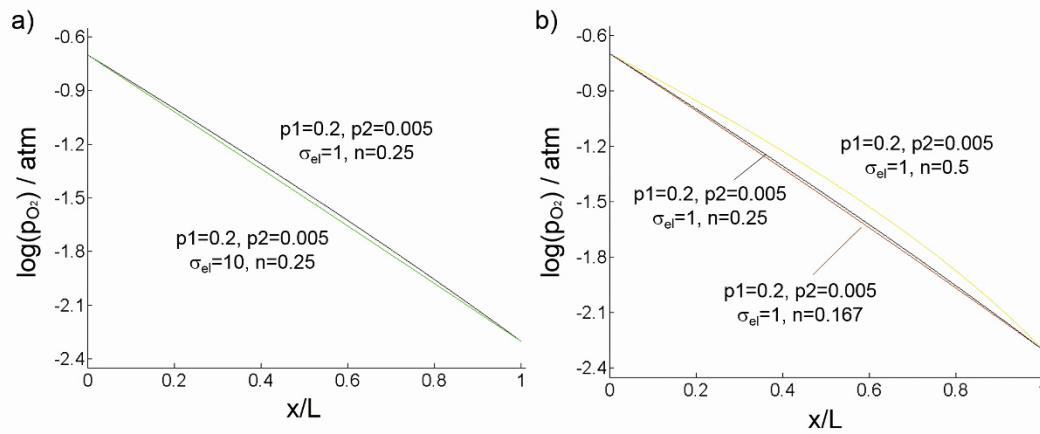


Fig. S6 Theoretical p_{O_2} profiles with different a) σ_{el} and b) n values in the dual-phase OTM located between synthetic air ($p_1 = 0.2$ atm) and inert gas ($p_2 = 0.005$ atm).

As shown in Fig. S7, it can be seen that the electronic conductivity has great effect on the drop of p_{O_2} across the membrane with big p_{O_2} gradient ($0.2 \sim 5 \times 10^{-15}$ atm). The drop lines are nonlinear in all cases. The slope of the tangent line changes significantly near the solid-gas interface at the sweep side (the slope equals to minus infinity at the interface). In other words, the big drop of p_{O_2} is mostly limited to the region near the interface at the sweep side. This finding may indicate that the porous layer at the sweep side will have more benefit than the feed side to the oxygen permeation with big p_{O_2} gradient, which is partly proved by the experiment results of ammonia oxidation

2 Carbon dioxide tolerant dual-phase membranes

through an asymmetric OTM.^[S8]

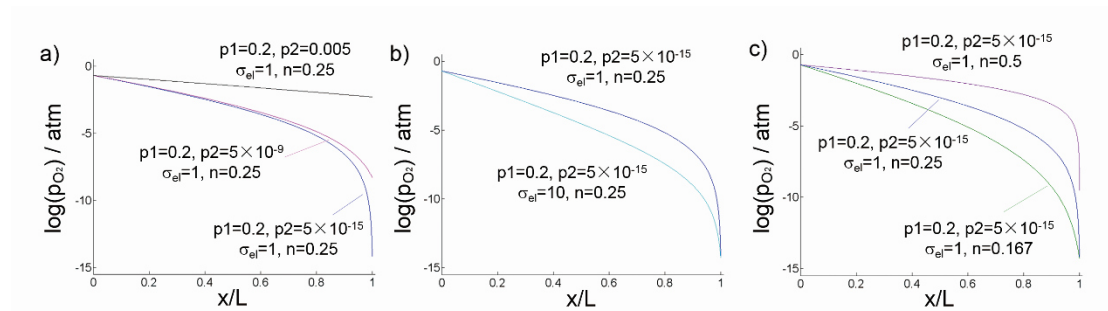


Fig. S7 Theoretical p_{O_2} profiles with different a) p_2 , b) σ_{el} and c) n values in the dual-phase OTM located between synthetic air ($p_1 = 0.2$ atm) and reducing gas ($p_2 = 5 \times 10^{-15}$, 5×10^{-9} or 0.005 atm).

Refinement of XRD pattern

As shown in Fig. S8, CGCO with a cubic fluorite structure ($Fm\bar{3}m$, $a = 542.2$ pm) and SFO with a cubic perovskite structure ($Pm\bar{3}m$, $a = 387.9$ pm) are well refined with sufficiently low reliability parameters.

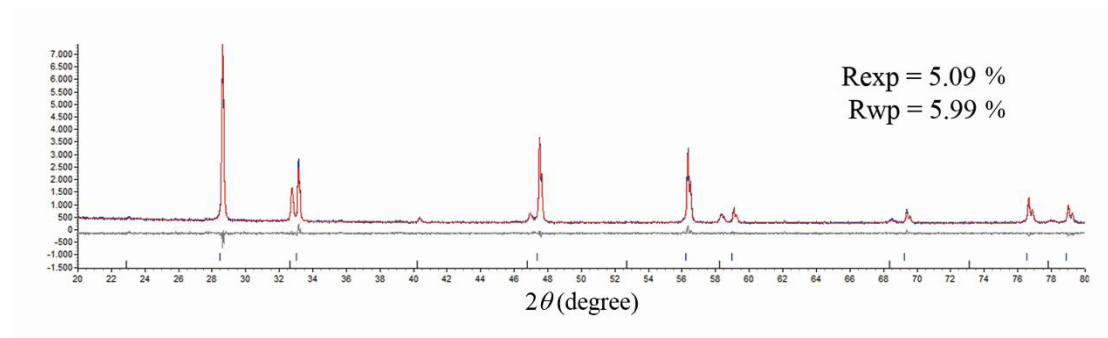


Fig. S8 Refined X-ray diffraction pattern of CGCO-SFO in air at room temperature.

References

[S1] Bouwmeester, H. J. M.; Burggraaf, A. J. Dense ceramic membranes for oxygen separation. *Membr. Sci. Technol.* **1996**, *4*, 435-528.

2.3 A new approach for carbon dioxide tolerance

- [S2] Park, J. H. Electronic Transport in 8 Mole Percent $\text{Y}_2\text{O}_3\text{-ZrO}_2$. *J. Electrochem. Soc.* **1989**, *136*, 2867-2876.
- [S3] Wang, S. R.; Kobayashi, T.; Dokiya, M.; Hashimoto, T. Electrical and Ionic Conductivity of Gd-Doped Ceria. *J. Electrochem. Soc.* **2000**, *147*, 3606-3609.
- [S4] Vashuk, V. V.; Kokhanovskii, L. V.; Yushkevich, I. I. Electrical Conductivity and Oxygen Stoichiometry of $\text{SrFeO}_{3-\delta}$. *Inorg. Mater.* **2000**, *36*, 90-96.
- [S5] Yasuda, I.; Hikita, T. Electrical Conductivity and Defect Structure of Calcium-Doped Lanthanum Chromites. *J. Electrochem. Soc.* **1993**, *140*, 1699-1704.
- [S6] Barin, I.; Sauert, F.; Patzki, G. Thermochemical Data of Pure Substances, VCH, Weinheim, 1995.
- [S7] Zhu, X. F.; Liu, H. Y.; Li, Q. M.; Cong, Y.; Yang, W. S. Unsteady-state permeation and surface exchange of dual-phase membranes. *Solid State Ionics* **2011**, *185*, 27-31.
- [S8] Cao, Z. W.; Jiang, H. Q.; Luo, H. X.; Baumann, S.; Meulenbergh, W. A.; Voss, H.; Caro, J. An Efficient Oxygen Activation Route for Improved Ammonia Oxidation through an Oxygen-Permeable Catalytic Membrane. *ChemCatChem* **2014**, *6*, 1190-1194.

3 Development of dual-phase membrane reactors for hydrogen and syngas production

3.1 Summary

Hydrogen has attracted increasing attention as a clean and renewable energy carrier in a future economy. Nowadays, the majority of hydrogen supply comes from the reformation of fossil fuels. Recently, hydrogen production from water splitting or partial oxidation of methane (POM) via an oxygen-transporting membrane (OTM) has proven to be a promising alternative. Meanwhile, large amounts of syngas (chiefly for Fischer-Tropsch synthesis) can be obtained simultaneously during the POM process. However, for commercial applications, cheap metal catalysts (such as nickel) are vulnerable to deactivation by carbon buildup (coking) in hydrocarbon environment, leading to considerable performance losses of the OTM reactors. Moreover, the employment of the typical oxygen-deficient perovskites (for instance $\text{SrFeO}_{3-\delta}$ -based perovskites) has been seriously hindered by their poor phase/chemical stability, which may result in a possible phase-transition-induced performance degradation. Accordingly, much effort is underway to effectively address the above issues.

In section 3.2, hydrogen production from water splitting coupled with POM via an OTM has been preferentially conducted due to water is considered as the ideal source for hydrogen generation. Herein, a sandwich-like symmetrical $\text{Ce}_{0.85}\text{Sm}_{0.15}\text{O}_{1.925}\text{-Sm}_{0.6}\text{Sr}_{0.4}\text{Al}_{0.3}\text{Fe}_{0.7}\text{O}_{3-\delta}$ (SDC-SSAF) dual-phase OTM reactor is successfully fabricated, which provides a largescale production of hydrogen and syngas. Moreover, a simple but remarkably effective method based on simple valve switching is introduced to regenerate the coked Ni catalyst in one unit without stopping reactions. Specially, it is proved that water (steam) can not only serve as a hydrogen source, but also can act as a “coke cleaner” in a symmetric system, thus it effectively helps recover the performance of membrane reactor suffering from coking. This study demonstrates the Ni-infiltrated sandwich-like symmetrical SDC-SSAF dual-phase OTM reactor as one of the most competitive candidates, and expands the comprehension of knowledge on the concept of chemical process intensification.

In section 3.3, it is shown that the presence of fluorite phase in the composite materials can significantly influence the phase structure of the adjacent perovskite in a beneficial way. A novel phase stabilization approach based on interdiffusional tailoring via a one-pot composite strategy has been proposed. It has led to the construction of a 20 wt.% $\text{SrFeO}_{3-\delta}$ -80 wt.% $\text{Ce}_{0.84}\text{Gd}_{0.16}\text{O}_{2-\delta}$ (SFO20-CGO80, nominal composition) dual-phase OTM reactor, which exhibited both high permeability and excellent stability. This findings will be able to guide the design as well as accelerate the development of advanced composite materials for applications in energy and environmental fields.

3.2 A highly efficient sandwich-like symmetrical dual-phase oxygen-transporting membrane reactor for hydrogen production by water splitting

Wei Fang,* Frank Steinbach, Zhongwei Cao, Xuefeng Zhu* and Armin Feldhoff*

Angewandte Chemie International Edition 2016, 55, 8648-8651.

Reprinted (adapted) with permission from (Angewandte Chemie International Edition). Copyright (2016) Wiley-VCH Verlag GmbH & Co. KGaA, Weinheim.



Hydrogen Production Hot Paper

International Edition: DOI: 10.1002/anie.201603528
German Edition: DOI: 10.1002/ange.201603528

A Highly Efficient Sandwich-Like Symmetrical Dual-Phase Oxygen-Transporting Membrane Reactor for Hydrogen Production by Water Splitting

Wei Fang,* Frank Steinbach, Zhongwei Cao, Xuefeng Zhu,* and Armin Feldhoff*

Abstract: Water splitting coupled with partial oxidation of methane (POM) using an oxygen-transporting membrane (OTM) would be a potentially ideal way to produce high-purity hydrogen as well as syngas. Over the past decades, substantial efforts have been devoted to the development of supported membranes with appropriate configurations to achieve considerable performance improvements. Herein, we describe the design of a novel symmetrical membrane reactor with a sandwich-like structure, whereby a largescale production ($> 10 \text{ mL min}^{-1} \text{ cm}^{-2}$) of hydrogen and syngas can be obtained simultaneously on opposite sides of the OTM. Furthermore, this special membrane reactor could regenerate the coke-deactivated catalyst *in situ* by water steam in a single unit. These results represent an important first step in the development of membrane separation technologies for the integration of multiple chemical processes.

Hydrogen, as a clean energy carrier, can play a key role in major industrial processes.^[1] Generally, the world's hydrogen supply comes from the reformation of fossil fuels, which increases the concentration of atmospheric CO_2 .^[2] Thus, the generation of hydrogen through water splitting is becoming an especially attractive alternative because water is considered as the ideal source owing to its abundance.^[3] However, efficient hydrogen production from water is quite difficult as a result of the very low equilibrium constant ($K_p \approx 2.1 \times 10^{-6}$) even at a relatively high temperature of 900°C .^[4] Relatively recently, an oxygen-transporting membrane (OTM) reactor, consisting of mixed ionic and electronic conducting (MIEC) materials, was applied to the water splitting reaction.^[5] On the feed side of the OTM, water was dissociated into hydrogen and oxygen species. Afterwards, oxygen species were transported as oxygen ions through the OTM. To ensure rapid removal of oxygen, methane/biomethane was fed on the sweep side of the membrane to consume the permeated

oxygen by partial oxidation of methane (POM) to syngas. Consequently, a higher production rate of hydrogen was obtained. However, cheap Ni-based catalysts are prone to deactivation as a result of coke deposition (that is, carbon buildup) once pure methane has been used as the feedstock, similar to the effect observed in industrial processes for methane reforming.^[6] Although great efforts have been focused on the development of coke-resistant catalysts,^[7] coke-deposition-induced performance degradation is still difficult to avoid. To maximize the function of the OTM, it is crucial to balance the high chemical stability and the practical oxygen permeability. When cobalt/copper-containing perovskite oxides (for example, $\text{Ba}_{0.5}\text{Sr}_{0.5}\text{Co}_{0.8}\text{Fe}_{0.2}\text{O}_{3-\delta}$) are employed as membrane materials, the performance of the reactor may gradually degrade with time because of the easily reducible active cations.^[8] As compared to perovskites, fluorite-type ceria-based oxides exhibit fast oxygen-ion mobility and good redox catalytic properties.^[9] Unfortunately, the electronic conductivities of such ionic conducting (IC) ceria derivatives are found to be the major bottleneck for oxygen permeation.^[10] Thus, an MIEC-IC composite dual-phase membrane is believed to be a prospective candidate for application in chemical reactors (Figure 1).^[11]

To date, tremendous efforts have been made to improve the oxygen permeability by designing supported/thin membranes and modifying their surfaces.^[12] Herein, we present a dual-phase OTM reactor with a sandwich-like symmetrical configuration, whereby two porous backbones built up on both side of the dense functional layer may alleviate the

[*] W. Fang, F. Steinbach, Prof. Dr. A. Feldhoff
Institute of Physical Chemistry and Electrochemistry
Leibniz University Hannover
Callinstrasse 3A, 30167 Hannover (Germany)
E-mail: wei.fang@pci.uni-hannover.de
armin.feldhoff@pci.uni-hannover.de

Z. W. Cao, Prof. Dr. X. F. Zhu
State Key Laboratory of Catalysis
Dalian Institute of Chemical Physics
Chinese Academy of Sciences
457 Zhongshan Road, Dalian 116023 (China)
E-mail: zhuxf@dicp.ac.cn

Supporting information for this article can be found under:
<http://dx.doi.org/10.1002/anie.201603528>.

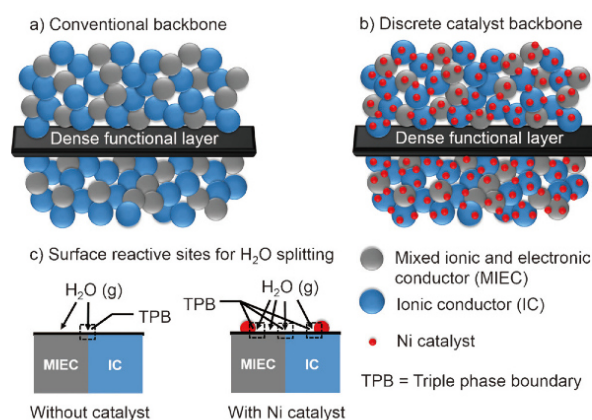


Figure 1. Schematic diagrams of a) the conventional blank backbone with a random mixture of an MIEC and an IC material; b) the Ni-catalyst-impregnated MIEC/IC composite backbone; and c) activity enhancement of the Ni-infiltrated backbone for H_2O splitting.

performance losses caused by slow surface-reaction kinetics (Figure 1 a),^[13] Additionally, the thinner dense layer obviously decreases the bulk diffusion resistance for the oxygen ionic transport.^[13] Remarkably, the amounts of possible reaction sites can be further increased by chemical infiltration processes.^[14] The backbones were impregnated with a Ni catalyst to increase the number of triple phase boundary (TPB) sites^[15] for water splitting reactions (Figure 1 b,c), as well as to catalyze the POM reaction. We also foresaw that coking could probably accompany the syngas production,^[6,7] which deactivates the catalyst and leads to a decrease of the hydrogen production rate from water. In this work, we propose that water (steam) can be used not only as a hydrogen source, but also as a “coke cleaner” to regenerate in situ the Ni catalyst in a sandwich-like symmetrical reactor by simply switching valves without stopping the reactions. As a result, three separate chemical reactions (water splitting, partial oxidation of methane, and carbon removal by steam) are integrated in one unit, which may contribute to the intensification of industrial processes.^[16]

A recently developed dual-phase OTM based on $\text{Ce}_{0.85}\text{Sm}_{0.15}\text{O}_{1.925}$ (75 wt.%) / $\text{Sm}_{0.6}\text{Sr}_{0.4}\text{Al}_{0.3}\text{Fe}_{0.7}\text{O}_{3-\delta}$ (25 wt.%), denoted SDC–SSAF, shows particularly promising and stable oxygen permeability under reducing conditions (see Figure S1 in the Supporting Information).^[17] Therefore, a novel SDC–SSAF sandwich-like symmetrical membrane was applied to the water splitting reaction. The cross-sectional morphologies of the sintered SDC–SSAF membrane with Ni infiltration are shown in Figure 2. It can be clearly seen that the sandwich-like symmetrical membrane comprises one thin dense layer with a thickness of about 30 μm and two thick porous backbones, each with a thickness of about 500 μm (Figure 2a–c). To better understand the nature of the Ni catalyst and its role in the reaction process, a magnified

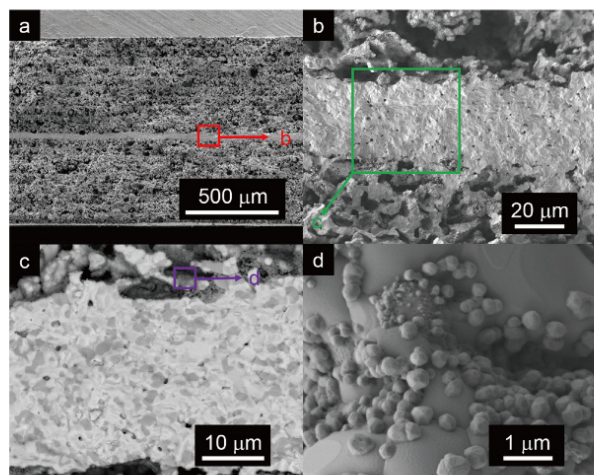


Figure 2. Cross-sectional microstructure of the Ni-infiltrated SDC–SSAF sandwich-like symmetrical dual-phase OTM. Secondary electron (SE) micrographs showing a) an overview and b) an expanded portion of the dense functional layer. c) Backscattered electron (BSE) micrograph of the dense layer. The light grains are the SDC phase, and the dark grains are the SSAF phase. d) Magnified SE micrograph of the impregnated Ni catalyst.

secondary electron (SE) micrograph was collected, which demonstrates that the Ni nanoparticles (diameter: approximately 100–700 nm) have tightly covered the surface of the backbone and are randomly distributed (Figure 2 d). Furthermore, the elemental distribution was identified by energy-dispersive X-ray spectroscopy (EDXS; Figure S2).

First, the oxygen permeability and stability of the non-infiltrated SDC–SSAF membrane was investigated. Figure 3 displays the long-term oxygen permeation of the membrane under three operational conditions. When helium was used as the sweep gas (with air as the feed gas), the permeation fluxes

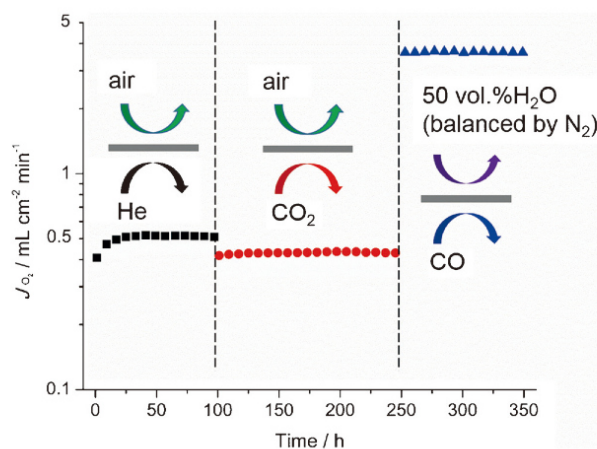


Figure 3. Long-term oxygen permeation rates (J_{O_2}) through the non-infiltrated SDC–SSAF symmetrical dual-phase membrane. Conditions: air = 100 mL min^{-1} or H_2O = 50 mL min^{-1} (balanced by 50 mL min^{-1} N_2) as the feed gas; He = 50 mL min^{-1} or CO_2 = 30 mL min^{-1} or CO = 30 mL min^{-1} as the sweep gas, respectively. 1 mL min^{-1} Ne as the internal standard gas. Temperature = 950 °C.

increased quickly with time for the initial 25 h, and then reached a relatively steady state. This phenomenon was also observed with other dual-phase membranes, and can be ascribed to the readjusting or reoxidation of the lattice structure from the as-prepared to the operational state.^[18] Subsequently, CO_2 was selected as reactive sweep gas. In this operation, a small decrease in the oxygen permeation rate (J_{O_2}) from 0.51 to 0.42 mL min^{-1} cm^{-2} was initially observed as a result of the decrease in the oxygen surface exchange rate resulting from CO_2 adsorption.^[19] However, no further degradation of oxygen flux was detected after 150 h of operation, indicating that the membrane is sufficiently tolerant towards CO_2 .

Finally, water splitting was conducted in the membrane reactor. Since hydrogen generation from water depends strongly on the oxygen permeability of the membrane, a larger driving force for oxygen transport can bring about a higher hydrogen production rate. Accordingly, a reducing gas (carbon monoxide) was employed as the sweep gas (with water steam as the feed gas). These changes led to a sevenfold increase in the oxygen permeation rate compared to that obtained with helium as the sweep gas (and air as the feed gas). Additionally, the membrane reactor

maintained a stable performance over 100 h of operation, which indicates good chemical stability under conditions suitable for water splitting. However, the oxidation of CO renders the method less useful. Therefore, it would be more attractive to combine the partial oxidation of methane (POM) to produce syngas (primarily for Fischer–Tropsch synthesis)^[20] in the reactor.

Along with the above-mentioned experiments, the production of hydrogen by water splitting coupled with POM was carried out in a Ni-infiltrated SDC–SSAF membrane reactor (Figure 4). As expected, a very high hydrogen production rate

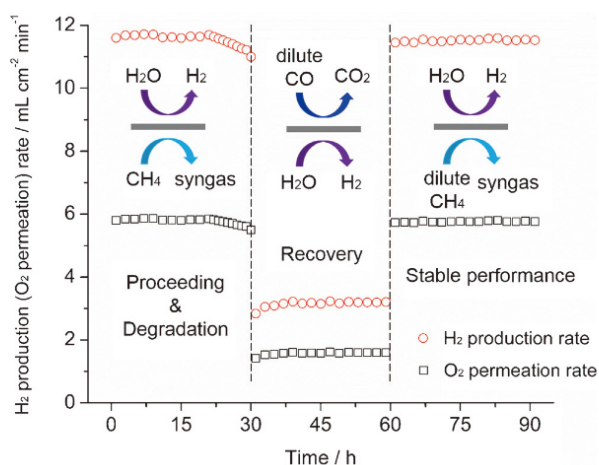


Figure 4. H₂ production and O₂ permeation rates as a function of time through the Ni-infiltrated SDC–SSAF symmetrical dual-phase membrane. Flow rate conditions: H₂O = 50 mL min⁻¹ (balanced by 50 mL min⁻¹ N₂); pure CH₄ = 5.84 mL min⁻¹; dilute CO = 3 mL min⁻¹ CO + 20 mL min⁻¹ He; dilute CH₄ = 5 mL min⁻¹ CH₄ + 5 mL min⁻¹ He. Ne = 1 mL min⁻¹ was used as the internal standard gas. Temperature = 900 °C.

of 11.7 mL min⁻¹ cm² was firstly achieved as a result of the increased oxygen permeability ascribed to fast surface exchange kinetics^[13] through Ni infiltration. It is worth noting that the hydrogen production rate declined after 20 h of operation, rapidly decreasing by 6% of its starting value within 10 h. It is likely that this deterioration can be attributed to undesirable coking of the catalyst. According to current knowledge in the field of Ni-based catalysts, water is considered to be the most effective inhibitor of carbon buildup.^[21] In an attempt to recover the performance of the membrane reactor, the water splitting reaction was conducted on the previous sweep side to simultaneously regenerate the catalyst in situ (dilute CO was used on the other side). The oxygen (hydrogen) fluxes were found to gradually increase over the next 8 h, then reaching a plateau. To make sure that coke has been successfully removed, dilute methane was applied to the sweep side afterwards. Generally, it is thought that lowering the concentration of methane decreases the oxygen permeation (hydrogen production) rate because of a smaller oxygen partial pressure gradient across the OTM.^[13] However, the dilute methane with a higher flow rate can overcome the diffusion resistance of the porous backbone

(Figure S5), resulting in a higher methane conversion rate compared with pure methane in principle. Note that a slightly lower but stable hydrogen (oxygen) flux was subsequently obtained during 30 h of operation for helium-diluted methane. This means that to some degree, coking can be avoided when dilute methane is used. A more reasonable explanation is that the ratio of O₂:CH₄ has a significant influence on coking,^[22] that is, a higher O₂:CH₄ ratio leads to a higher resistance to coking (coking occurs easily at a ratio of O₂:CH₄ ≈ 1:2 for pure methane, but hardly at O₂:CH₄ > 1:2 for helium-diluted methane).

Figure 5 shows the selectivity of CO₂ (or CO) and the conversion of methane with time in the membrane reactor (which also supports the above conclusion). Compared with the relatively stable values obtained under an atmosphere of dilute methane, the selectivity of CO₂ declined from 5.18% to

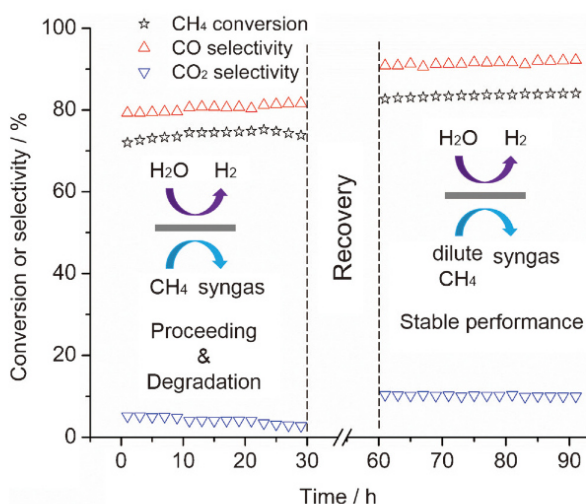


Figure 5. Conversion of methane and selectivity of CO or CO₂ as a function of time in the Ni-infiltrated SDC–SSAF symmetrical dual-phase membrane reactor. Flow rate conditions: H₂O = 50 mL min⁻¹ (balanced by 50 mL min⁻¹ N₂); pure CH₄ = 5.84 mL min⁻¹; dilute CH₄ = 5 mL min⁻¹ CH₄ + 5 mL min⁻¹ He. Ne = 1 mL min⁻¹ was used as the internal standard gas. Temperature = 900 °C.

2.82% within 30 h in the presence of pure methane. This result demonstrates that the partial oxidation of methane is more favorable than the total oxidation of methane. Moreover, the selectivity value of CO_x (the sum of CO₂ and CO) was far from 100% in pure methane, but was very close to 100% for the dilute case. This clearly suggests that coking occurred in the reactor when using pure methane as the sweep gas (Figure S3), as also indicated by the fact that the line denoting methane conversion became curved with time (another indication of catalyst deactivation). However, helium-diluted methane was used as part of a proof-of-principle study limited for laboratory use, as for widespread application in industry pure methane is used. Fortunately, the catalyst can be completely regenerated in our symmetrical membrane system, enabling the sustaining production of hydrogen from water.

In conclusion, this work presents an approach to obtain considerably high hydrogen production rates (Table S1) through water splitting coupled with POM by means of a dual-phase OTM with a sandwich-like symmetrical structure. However, the performance of the membrane reactor may degrade as a result of catalyst deactivation (coking). It is demonstrated first that the catalyst can be regenerated in situ in a single unit by conducting the water splitting reaction on the catalyst-deactivated side. This discovery will enable us to gain new insight into the interplay between catalysis (recovery) and separation in the OTM reactor, and accelerate the pace of development of next-generation practical OTM applications.

Acknowledgements

This work has been supported by the German Research Foundation (DFG; no. FE928/7-1) and the Natural Science Foundation of China (21271169 and 21476225). We also acknowledge A. Wollbrink and W. Y. Liang for technical support.

Keywords: catalyst regeneration · hydrogen production · membrane reactor · methane · water splitting

How to cite: *Angew. Chem. Int. Ed.* **2016**, *55*, 8648–8651
Angew. Chem. **2016**, *128*, 8790–8793

- [1] M. D. Symes, L. Cronin, *Nat. Chem.* **2013**, *5*, 403–409.
- [2] S. J. Davis, K. Caldeira, H. D. Matthews, *Science* **2010**, *329*, 1330–1333.
- [3] J. A. Turner, *Science* **2004**, *305*, 972–974.
- [4] S. Ihara, *Bull. Electrochem. Lab.* **1977**, *41*, 259–280.
- [5] a) H. Q. Jiang, H. H. Wang, S. Werth, T. Schiestel, J. Caro, *Angew. Chem. Int. Ed.* **2008**, *47*, 9341–9344; *Angew. Chem.* **2008**, *120*, 9481–9484; b) U. Balachandran, T. H. Lee, S. E. Dorris, *Int. J. Hydrogen Energy* **2007**, *32*, 451–456.
- [6] a) D. L. Trimm, *Catal. Today* **1999**, *49*, 3–10; b) Y. B. Lin, Z. L. Zhan, J. Liu, S. A. Barnett, *Solid State Ionics* **2005**, *176*, 1827–1835.
- [7] a) D. Neagu, T. S. Oh, D. N. Miller, H. Ménard, S. M. Bukhari, S. R. Gamble, R. J. Gorte, J. M. Vohs, J. T. S. Irvine, *Nat. Commun.* **2015**, *6*, 8120; b) Y. Chen, Y. X. Zhang, Y. Lin, Z. B. Yang, D. Su, M. F. Han, F. L. Chen, *Nano Energy* **2014**, *10*, 1–9.
- [8] a) Z. P. Shao, H. Dong, G. X. Xiong, Y. Cong, W. S. Yang, *J. Membr. Sci.* **2001**, *183*, 181–192; b) M. Harada, K. Domen, M. Hara, T. Tatsumi, *Chem. Lett.* **2006**, *35*, 968–969; c) W. Q. Jin, S. G. Li, P. Huang, N. P. Xu, J. Shi, Y. S. Lin, *J. Membr. Sci.* **2000**, *166*, 13–22.
- [9] M. Mogensen, N. M. Sammes, G. A. Tompsett, *Solid State Ionics* **2000**, *129*, 63–94.
- [10] M. Balaguer, C. Solís, J. M. Serra, *Chem. Mater.* **2011**, *23*, 2333–2343.
- [11] a) V. V. Kharton, A. V. Kovalevsky, A. P. Viskup, A. L. Shaula, F. M. Figueiredo, E. N. Naumovich, F. M. B. Marques, *Solid State Ionics* **2003**, *160*, 247–258; b) X. F. Zhu, Q. M. Li, Y. F. He, Y. Cong, W. S. Yang, *J. Membr. Sci.* **2010**, *360*, 454–460; c) S. Y. Cheng, H. Huang, S. Ovtar, S. B. Simonsen, M. Chen, W. Zhang, M. Sjøgaard, A. Kaiser, P. V. Hendriksen, C. S. Chen, *ACS Appl. Mater. Interfaces* **2016**, *8*, 4548–4560; d) W. Fang, F. Y. Liang, Z. W. Cao, F. Steinbach, A. Feldhoff, *Angew. Chem. Int. Ed.* **2015**, *54*, 4847–4850; *Angew. Chem.* **2015**, *127*, 4929–4932; e) Z. B. Zhang, W. Zhou, Y. B. Chen, D. J. Chen, J. W. Chen, S. M. Liu, W. Q. Jin, Z. P. Shao, *ACS Appl. Mater. Interfaces* **2015**, *7*, 22918–22926.
- [12] a) K. Watanabe, M. Yuasa, T. Kida, Y. Teraoka, N. Yamazoe, K. Shimano, *Adv. Mater.* **2010**, *22*, 2367–2370; b) X. Y. Tan, Y. T. Liu, K. Li, *AIChE J.* **2005**, *51*, 1991–2000; c) Y. Y. Wei, H. F. Liu, J. Xue, Z. Li, H. H. Wang, *AIChE J.* **2011**, *57*, 975–984; d) J. H. Joo, K. S. Yun, Y. Lee, J. Jung, C. Y. Yoo, J. H. Yu, *Chem. Mater.* **2014**, *26*, 4387–4394; e) S. Liu, X. Tan, Z. Shao, J. C. Diniz da Costa, *AIChE J.* **2006**, *52*, 3452–3461; f) S. Baumann, J. M. Serra, M. P. Lobera, S. Escolástico, F. Schulze-Küppers, W. A. Meulenbergh, *J. Membr. Sci.* **2011**, *377*, 198–205; g) J. W. Zhu, Z. Y. Dong, Z. K. Liu, K. Zhang, G. R. Zhang, W. Q. Jin, *AIChE J.* **2014**, *60*, 1969–1976.
- [13] *Fundamentals of Inorganic Membrane Science and Technology* (Eds.: H. J. M. Bouwmeester, A. J. Burggraaf, L. Cot), Elsevier, Amsterdam, **1996**, pp. 435–528.
- [14] a) J. M. Vohs, R. J. Gorte, *Adv. Mater.* **2009**, *21*, 943–956; b) D. Ding, M. F. Liu, Z. B. Liu, X. X. Li, K. Blinn, X. B. Zhu, M. L. Liu, *Adv. Energy Mater.* **2013**, *3*, 1149–1154; c) S. Kim, A. Jun, O. Kwon, J. Kim, S. Yoo, H. Y. Jeong, J. Shin, G. Kim, *ChemSusChem* **2015**, *8*, 3153–3158.
- [15] S. B. Adler, *Chem. Rev.* **2004**, *104*, 4791–4843.
- [16] K. K. Sirkar, A. G. Fane, R. Wang, S. R. Wickramasinghe, *Chem. Eng. Process.* **2015**, *87*, 16–25.
- [17] X. F. Zhu, Y. Liu, Y. Cong, W. S. Yang, *Solid State Ionics* **2013**, *253*, 57–63.
- [18] a) X. F. Zhu, W. S. Yang, *AIChE J.* **2008**, *54*, 665–672; b) J. Xue, A. Feldhoff, DOI: 10.1016/j.jeurceramsoc.2016.05.023.
- [19] W. Fang, F. Steinbach, C. S. Chen, A. Feldhoff, *Chem. Mater.* **2015**, *27*, 7820–7826.
- [20] H. Schulz, *Appl. Catal. A* **1999**, *186*, 3–12.
- [21] L. Yang, Y. M. Choi, W. T. Qin, H. Y. Chen, K. Blinn, M. F. Liu, P. Liu, J. M. Bai, T. A. Tyson, M. L. Liu, *Nat. Commun.* **2011**, *2*, 357.
- [22] Z. L. Zhan, Y. B. Lin, M. Pillai, I. Kim, S. A. Barnett, *J. Power Sources* **2006**, *161*, 460–465.

Received: April 11, 2016

Published online: May 31, 2016



Supporting Information

A Highly Efficient Sandwich-Like Symmetrical Dual-Phase Oxygen-Transporting Membrane Reactor for Hydrogen Production by Water Splitting

Wei Fang, Frank Steinbach, Zhongwei Cao, Xuefeng Zhu,* and Armin Feldhoff**

anie_201603528_sm_miscellaneous_information.pdf

1. Experimental details

1.1 Synthesis of powders and membranes

Both $\text{Ce}_{0.85}\text{Sm}_{0.15}\text{O}_{1.925}$ (SDC) and $\text{Sm}_{0.6}\text{Sr}_{0.4}\text{Al}_{0.3}\text{Fe}_{0.7}\text{O}_{3-\delta}$ (SSAF) powders were prepared by solid state reaction method with the required amounts of oxides and carbonates.^[1] Then the ball-milled SDC-SSAF dual-phase powders with a weight ratio of 75 wt.% SDC/25 wt.% SSAF were used for tape-casting to fabricate the dense functional layer and porous backbones. The detailed description of this process can be found elsewhere.^[2] The green sandwich-like symmetrical membranes were obtained by stacking 8 pieces of porous layer tapes for each backbone and 1 piece of dense layer tape under a lamination pressure of ~ 100 MPa for 10 min. After co-lamination, the green tapes were cut into discs, then sintered at 1450 °C for 3 h to get a dense functional layer, which is gas-tight. The catalyst particles formed on the backbones were produced by wet impregnation^[3] with a solution containing 1.5 mol L^{-1} nickel nitrate, followed by firing in air at 800 °C for 1 h to convert the nickel nitrate into nickel oxide. After 6 cycles of infiltration, ~ 20 wt.% NiO loading was achieved in the SDC-SSAF symmetrical membranes. Finally, these membranes were used for oxygen permeation tests. Note that the catalyst was reduced by dilute hydrogen ($5 \text{ mL min}^{-1} \text{ H}_2 + 20 \text{ mL min}^{-1} \text{ He}$) for 1 h before the partial oxidation of methane (POM) measurement.

1.2 Characterization of membrane materials

The phase structures of the membrane materials were determined by X-ray diffraction (XRD, D8 Advance, Bruker-AXS, with Cu $K\alpha$ radiation) in the 2θ range 20 - 80° with a step width of 0.01° . Microstructure of the symmetrical membranes were observed by secondary electron (SE) and back-scattered electron (BSE) contrast (JEOL JSM-6700F) operated at 2 - 20 kV. The elemental distribution was investigated on the same electron microscope by energy dispersive X-ray spectroscopy (EDXS, Oxford INCA 300) at 20 kV.

1.3 Measurements of oxygen permeation

The oxygen permeation was conducted in a home-made high-temperature oxygen permeation device,^[4] and a permeation cell was formed by sealing the disk membrane onto an alumina tube using commercial glass powders (Schott AG, Germany). The effective surface areas of the membranes were around 0.5 cm². Synthetic air (100 mL min⁻¹; 21 vol.% O₂ and 79 vol.% N₂) or water steam balanced by N₂ (100 mL min⁻¹; 50 vol.% H₂O and 50 vol.% N₂) was applied as the feed gas, and high purity He (50 mL min⁻¹), CO₂ (30 mL min⁻¹), CO (30 mL min⁻¹), dilute CO (3 mL min⁻¹ CO + 20 mL min⁻¹ He), CH₄ (5.84 ml min⁻¹), or dilute CH₄ (5 mL min⁻¹ CH₄ + 5 mL min⁻¹ He) as the sweep gas, respectively. The flow rates of the gases (CH₄, CO, CO₂, He, N₂ and air) were controlled by gas mass flow controllers (Bronkhorst, Germany). The flow of water steam was controlled by a liquid mass flow controller (Bronkhorst, Germany), and water was fully evaporated at 180 °C before being fed into the reactor. The effluents on the both side were analyzed by an online-coupled gas chromatograph (Agilent 6890A). The absolute flow rates of the effluents were calculated using high purity neon (1 ml min⁻¹) as an internal standardization. The leakages were no more than 1% for all the oxygen permeation tests and were subtracted when calculating the oxygen permeation fluxes. According to the equation of water splitting reaction (H₂O ↔ H₂ + 1/2O₂), the hydrogen production rate (J_{H_2}) is in a relationship with the oxygen permeation rate (J_{O_2}), which can be described as:

$$J_{H_2} = 2J_{O_2} \quad (\text{Equation S1})$$

In addition, the CH₄ conversion (X_{CH_4}), the CO or CO₂ selectivity (S_{CO} or S_{CO_2}) on the sweep side were calculated by Equation S2, S3 and S4, where $F(i)$ denotes the flow rate of species i :

$$X_{CH_4} = \left(1 - \frac{F(CH_4, out)}{F(CH_4, in)}\right) \times 100\% \quad (\text{Equation S2})$$

$$S(CO) = \frac{F(CO, out)}{F(CH_4, in) - F(CH_4, out)} \times 100\% \quad (\text{Equation S3})$$

$$S(CO_2) = \frac{F(CO_2, out)}{F(CH_4, in) - F(CH_4, out)} \times 100\% \quad (\text{Equation S4})$$

2. Supporting figures and tables

2.1 XRD analysis of membranes

The X-ray diffraction patterns obtained for SDC and SSAF can be indexed as a cubic fluorite structure and a rhombohedral perovskite structure respectively (Figure S1a), and no impurity phases (for example, SrCeO_3 and Sm_2NiO_4) can be detected in the dual-phase membrane (Figure S1a,b). Moreover, the obvious shift of perovskite reflections (e.g. the reflections at around 47° and 59° moved to lower angles) was observed after annealing under syngas atmosphere, which indicates the reduction of the perovskite (Figure S1c). However, this reduction was almost limited to the surface (Figure S1d).

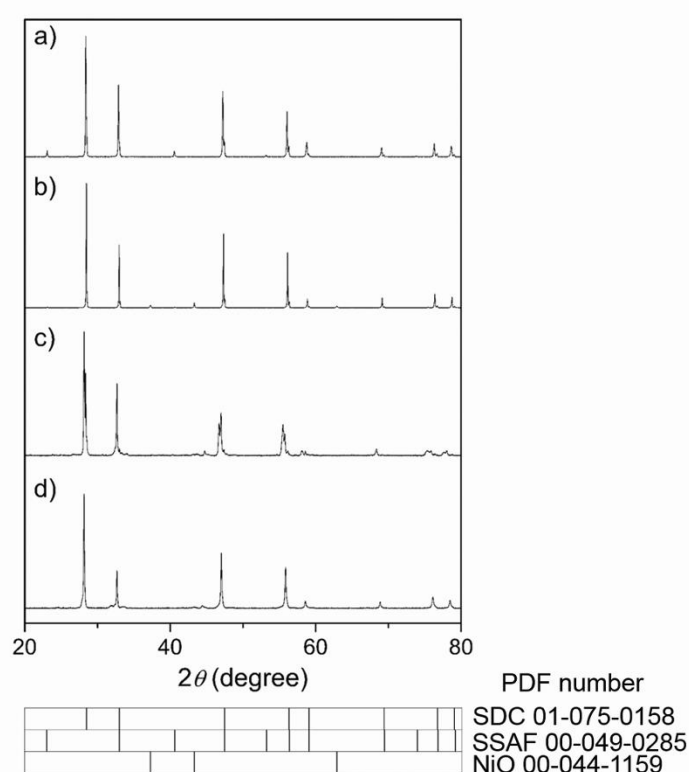


Figure S1 XRD patterns of SDC-SSAF symmetrical dual-phase membranes. a) As-prepared. b) Impregnated. Reflections from c) surface and d) bulk (surface was removed by polishing) of the as-prepared membrane after treatment at 900°C under syngas condition ($4\text{ mL min}^{-1}\text{ H}_2 + 2\text{ mL min}^{-1}\text{ CO} + 4\text{ mL min}^{-1}\text{ He}$) for 30 hours. Indication of PDF number at Bragg positions refers to the powders diffraction file database.

2.2 SEM-EDXS analysis of the infiltrated symmetrical membrane

As shown in Figure S2, EDXS results show that no obvious intermixing of Ce and Fe between the two phases took place (Figure S2d,e), and demonstrate the existence of nickel at the porous backbone (Figure S2f).

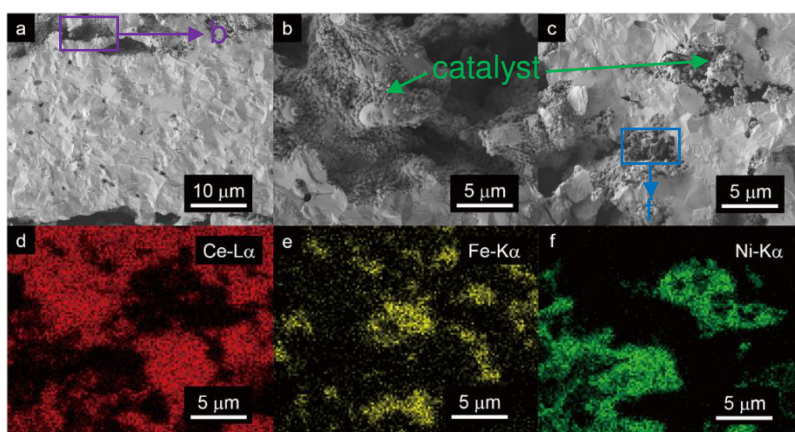


Figure S2 a-c) SE micrographs near the dense functional layer of the as-prepared infiltrated SDC-SSAF dual-phase symmetrical membrane. EDXS elemental distributions of d) Ce, e) Fe and f) Ni.

As depicted in Figure S3, BSE-EDXS results show that serious coking was detected in the porous backbone after exposure to pure methane for POM reaction, which is further verified by the elemental distribution of carbon.

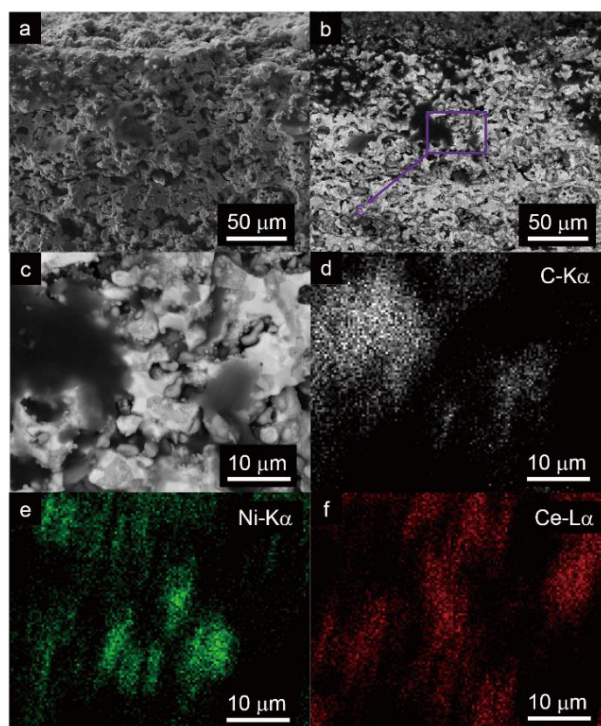


Figure S3 a) SE and b,c) BSE micrographs of the porous backbone of the spent

3 Dual-phase membrane reactors

(before recovery) SDC-SSAF dual-phase symmetrical membrane. EDXS elemental distributions of d) C, e) Ni and f) Ce.

As shown in Figure S4, coke was totally removed by water steam, and no obvious carbon enrichment can be found in the porous backbone, which can be easily concluded from the comparison between Figure S3c and Figure S4c.

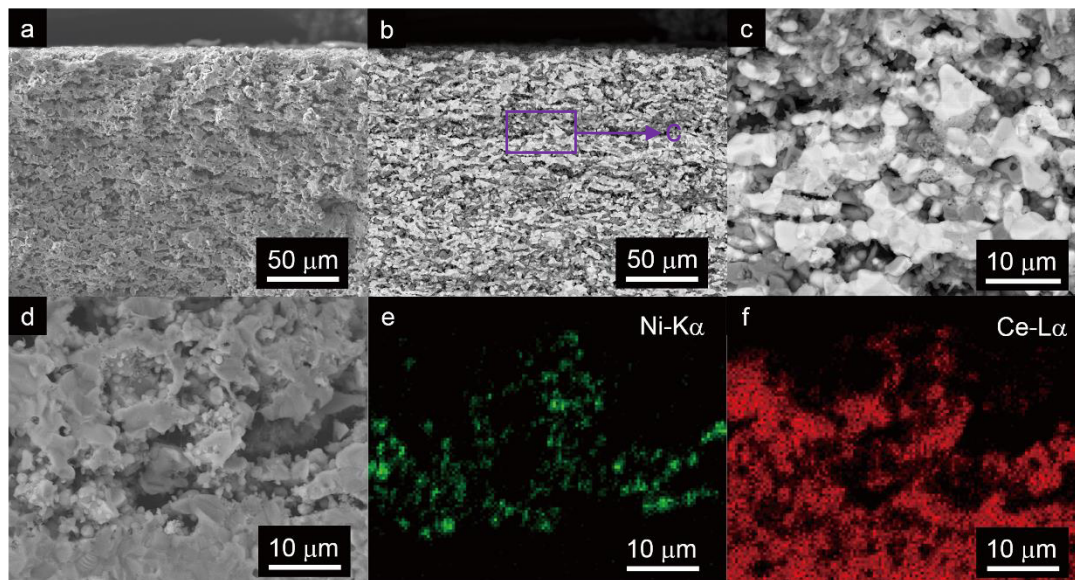


Figure S4 a,d) SE and b,c) BSE micrographs of the spent (after recovery) SDC-SSAF dual-phase symmetrical membrane. EDXS elemental distributions of e) Ni and f) Ce.

2.3 The influence of sweep rate on the oxygen permeation

As shown in Figure S5, the oxygen permeation flux increases significantly with increasing the sweep rate of He. One possible explanation is that larger flow rate is helpful to overcome the resistance of gas diffusion from porous backbone, simultaneously resulting in a larger oxygen partial pressure gradient across the membrane.^[5]

3.2 A sandwich-like membrane reactor for water splitting

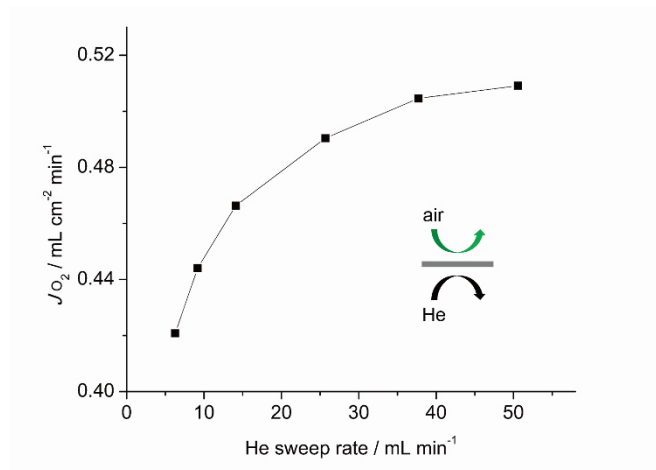


Figure S5 Oxygen permeation fluxes as a function of He sweep rate at 950 °C. Feed side: 100 mL min⁻¹ air.

2.4 Gas chromatograms of the product gases in the membrane reactor

As described in Figure S6, remarkable amounts of hydrogen as well as syngas have been formed by water splitting combined with POM via a sandwich-like symmetrical dual-phase oxygen-transporting membrane (OTM) reactor.

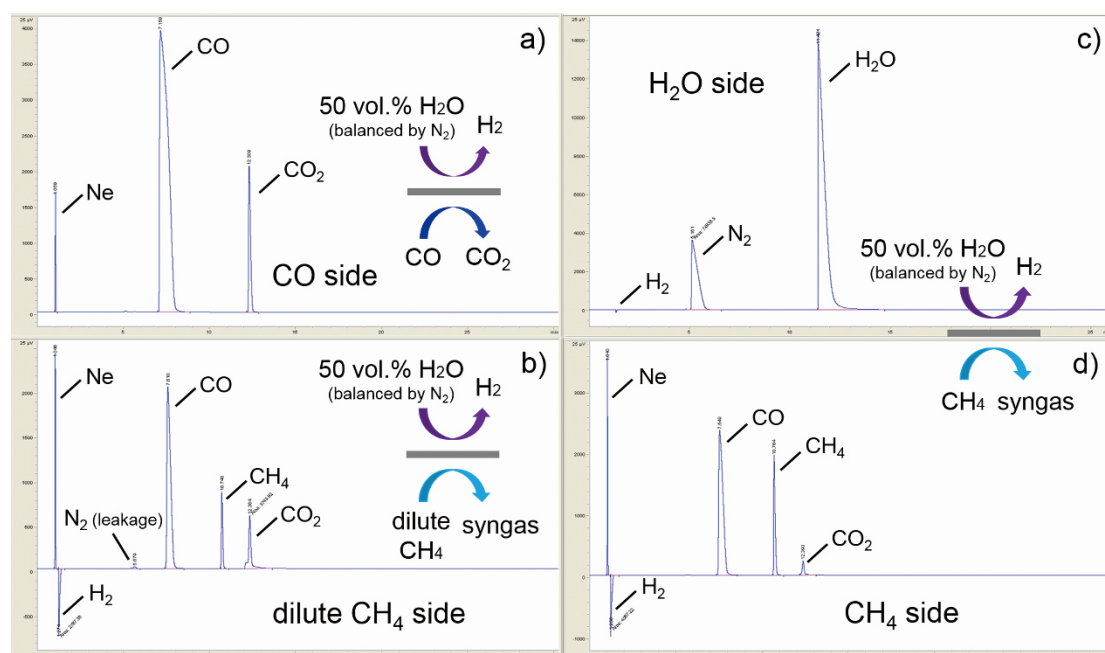


Figure S6 Gas chromatograms of the product gases for SDC-SSAF symmetrical membrane reactor under a) H₂O/CO, b) H₂O/dilute CH₄, c) H₂O/CH₄ (H₂O side) and d) H₂O/CH₄ (CH₄ side) gradients.

2.5 Summary of hydrogen production rate from water splitting for several OTMs

As shown in Table S1, it is concluded that supported membranes with ultrathin dense functional layer show a much better performance. In several previous work, a relatively high hydrogen generation rate only could be achieved by using hydrogen as the sweep gas, which makes little sense in industry. Herein, a significantly high hydrogen production flux ($>10 \text{ mL min}^{-1} \text{ cm}^{-2}$) has been firstly obtained by a novel sandwich-like symmetrical dual-phase membrane reactor using methane as the sweep gas, which is of technological importance with commercial applications.

Table S1 Comparison of hydrogen production rate of several OTMs via water splitting at 900 °C.

Note: Thickness denotes the thickness of the dense functional layer.

Membrane material	Shape	Thickness (μm)	Feed side	Sweep side	H ₂ production rate ($\text{mL min}^{-1} \text{ cm}^{-2}$)
BaFe _{0.9} Zr _{0.1} O _{3-δ} ^[6]	Disk	1560	150 mL min ⁻¹ 49% H ₂ O/N ₂	150 mL min ⁻¹ CO	3.2
La _{0.7} Sr _{0.3} Cu _{0.2} Fe _{0.8} O _{3-δ} ^[7]	Supported disk	22	150 mL min ⁻¹ 49% H ₂ O/N ₂	150 mL min ⁻¹ 80% H ₂ /He	9.0
BaCo _x Fe _y Zr _{1-x-y} O _{3-δ} ^[8]	Hollow fiber	100	40 mL min ⁻¹ 75% H ₂ O/He	50 mL min ⁻¹ 4% CH ₄ /He/Ne	2.15
60vol.%Ce _{0.8} Gd _{0.2} O _{1.9} -40vol.%Gd _{0.08} Sr _{0.88} Ti _{0.95} Al _{0.05} O _{3-δ} ^[9]	Supported disk	25	400 mL min ⁻¹ 25% H ₂ O/Ar- 0.2% H ₂	400 mL min ⁻¹ H ₂ /Ar/ H ₂ O(3%)	9.67
60vol.%CGO-40vol.%Ni ^[10]	Disk	130	49% H ₂ O/N ₂	80% H ₂ /He	6.0
75wt%Ce _{0.85} Sm _{0.15} O _{1.925} - 25wt%Sm _{0.6} Sr _{0.4} Al _{0.3} Fe _{0.7} O _{3-δ} (This work)	Supported disk	30	100 mL min ⁻¹ 50% H ₂ O/N ₂	11 mL min ⁻¹ 45% CH ₄ /He/Ne	11.5

References

- [1] X. F. Zhu, Y. Liu, Y. Cong, W. S. Yang, *Solid State Ionics* **2013**, *253*, 57-63.
- [2] Z. W. Cao, X. F. Zhu, W. P. Li, B. Xu, L. N. Yang, W. S. Yang, *Mater. Lett.*

3.2 A sandwich-like membrane reactor for water splitting

- 2015**, 147, 88-91.
- [3] S. P. Jiang, *Mater. Sci. Eng. A* **2006**, 418, 199-210.
- [4] F. Y. Liang, H. X. Luo, K. Partovi, O. Ravkina, Z. W. Cao, Y. Liu, J. Caro, *Chem. Commun.* **2014**, 50, 2451-2454.
- [5] J. M. Serra, J. G. Fayos, S. Baumann, F. S. Küppers, W. A. Meulenber, *J. Membr. Sci.* **2013**, 447, 297-305.
- [6] C. Y. Park, T. H. Lee, S. E. Dorris, U. Balachandran, *Int. J. Hydrogen Energy* **2013**, 38, 6450-6459.
- [7] C. Y. Park, T. H. Lee, S. E. Dorris, U. Balachandran, *Int. J. Hydrogen Energy* **2010**, 35, 4103-4110.
- [8] H. Q. Jiang, H. H. Wang, S. Werth, T. Schiestel, J. Caro, *Angew. Chem. Int. Ed.* **2008**, 47, 9341-9344.
- [9] H. B. Wang, S. Gopalan, U. B. Pal, *Electrochim. Acta* **2011**, 56, 6989-6996.
- [10] U. Balachandran, T. H. Lee, S. Wang, S. E. Dorris, *Int. J. Hydrogen Energy* **2004**, 29, 291-296.

3.3 A method of stabilizing perovskite structure via interdiffusional tailoring and its application in an oxygen-transporting membrane reactor

Wei Fang,* Chao Zhang, Frank Steinbach and Armin Feldhoff*

Submitted to *Angewandte Chemie International Edition*.

A method of stabilizing perovskite structure via interdiffusional tailoring and its application in an oxygen-transporting membrane reactor

Wei Fang,* Chao Zhang, Frank Steinbach and Armin Feldhoff*

Abstract: Perovskite oxides have been under intense investigation as promising candidates for devices in the field of energy conversion and storage. Unfortunately, these perovskites are subjected to a frequent performance loss caused by phase transition. Herein, except for commonly used doping method, a novel phase stabilization approach via interdiffusional tailoring is identified in perovskite-based composites. As an example, a phase-stabilized perovskite-fluorite material with both cubic symmetry was obtained by appropriate one-pot strategy. Accordingly, our findings make it possible to develop a high-performance and extremely stable oxygen-transporting membrane reactor, which also opens up numerous opportunities to overcome the phase-transition-induced performance degradation in other systems.

Perovskite oxides are of great interest in the field of energy materials because of their vitally important electronic, magnetic and chemical properties.^[1] Owing to the excellent mixed ionic and electronic conduction and fast oxygen exchange kinetics, oxygen-deficient perovskites with general formula of $ABO_{3-\delta}$ such as $SrFeO_{3-\delta}$ (SFO)-based oxides hold considerable promise for potential applications as high-active catalysts,^[2] cathodes of fuel cells and metal-air batteries,^[3,4] as well as oxygen-transporting membranes (OTMs).^[5] However, the commercial employment of these perovskites has been seriously impeded by their intrinsic poor phase stability, especially at intermediate and low temperatures ($<800\text{ }^{\circ}\text{C}$),^[6] for instance, depending on the oxygen non-stoichiometry, SFO possesses various crystal structures including brownmillerite, tetragonal, orthorhombic and cubic symmetries,^[7] which may result in a frequent phase-transformation-induced performance degradation. One possible route to harnessing the structural instability drawback would be to incorporate high valent cations into the A- or B-site of the perovskite lattices, probably leading to a sudden drop in the number of oxygen vacancies.^[8] Specifically, Ti-doped SFO materials exhibited a stabilized cubic perovskite structure, never-

theless at the expense of the electrochemical performances including oxygen-ionic conductivity.^[9,10] Not surprisingly, single-phase perovskites seldomly fulfill the desired requirements for diverse applications.

On the other hand, composite materials consisting of two or more distinct components clearly reveal desirable combinative or unique properties compared to the individuals,^[11] which offers a very promising option to the materials challenge. With regard to perovskite-based composite OTMs or air cathodes, fluorite-type doped-cerias are considered as a potential alternative due to a combination of superior oxygen-ion mobility, excellent redox catalytic property as well as good phase and chemical stability over a wide range of oxygen partial pressures and temperatures.^[12] In the past decade, perovskite-fluorite composite OTMs comprising of a mixed conductor and an ionic conductor were heralded as a robust paradigm for attractive OTM technology,^[13] emerging in the areas of pure oxygen production,^[14] oxy-fuel combustion with CO_2 capture^[15] and catalytic membrane reactors,^[16] for example the partial oxidation of methane (POM) to produce syngas.^[17] Very recently, the state-of-the-art one-pot method has proved to be applicable to fabricate the oxygen permeable dual-phase membranes with highly elaborate and complex morphology.^[18] Generally, the cation interdiffusion in polycrystalline composite materials could be easily observed in many cases,^[19] which will give rise to a critical reconsideration of the one-pot method. Therefore, it is crucial to understand and control the self-assembly of cations as well as phase separation in the one-pot systems, and further identify routes to optimize the performance of dual-phase OTMs.

Here, rather than using a traditional heavily doping route, a new phase stabilization approach is proposed to inhibit phase transitions of instable perovskites by deliberately interdiffusional tailoring in the dual-phase composites. In the present work, oxygen-deficient SFO is selected as a prototypical example of a high-performance perovskite that suffers from facile phase transformation (for instance, from cubic at high temperatures to orthorhombic/tetragonal at low temperatures in air atmosphere), and meanwhile 8 mol% gadolinia doped ceria ($\text{Ce}_{0.84}\text{Gd}_{0.16}\text{O}_{2-\delta}$, abbreviation as CGO) not only serves as an oxygen-ionic conductor for dual-phase OTM, but also functions as a “stabilizer” that provides the effective doping sources of high valent metal ions (such as Ce and Gd) to limit the phase change of adjacent perovskite via an interdiffusional process between the fluorite phase and perovskite phase.

All the SFO-CGO dual-phase powders were prepared by a popular one-pot citrate-nitrate combustion method.^[18] Besides, a trace of copper cations was introduced to the dual-phase precursors as sintering aids.^[20] Furthermore, the resulting dual-phase materials consisting of SFO and CGO oxides with nominal weight ratios of 80:20, 50:50 and 20:80 were denoted as SFO80-CGO20,

W. Fang, F. Steinbach, Prof. Dr. A. Feldhoff
Institute of Physical Chemistry and Electrochemistry
Leibniz University Hannover
Callinstrasse 3A, 30167 Hannover (Germany)
E-mail: wei.fang@pci.uni-hannover.de;
armin.feldhoff@pci.uni-hannover.de

Dr. C. Zhang
Institute for Mineralogy
Leibniz University Hannover
Callinstrasse 3, 30167 Hannover (Germany)

Supporting information for this article is given via a link at the end of the document.

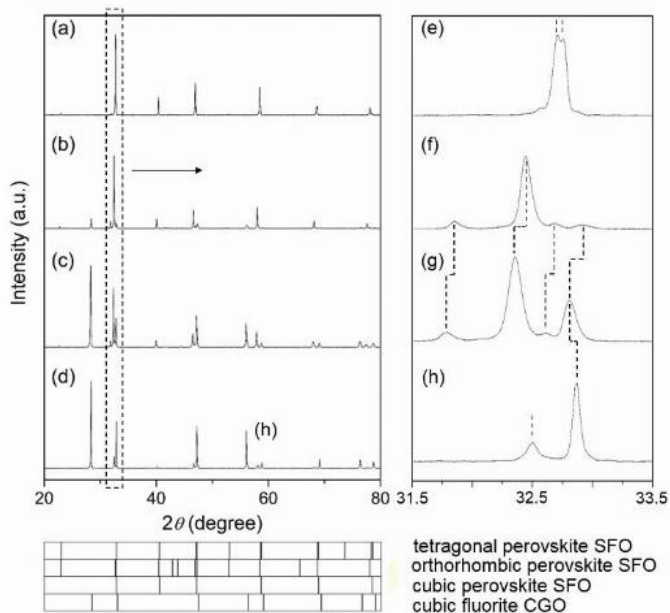


Figure 1. X-ray diffraction patterns of single-phase SFO and one-pot dual-phase SFO-CGO ceramics. a,e) SFO. b,f) SFO80-CGO20. c,g) SFO50-CGO50. d,h) SFO20-CGO80. e-h) Close-up of the XRD patterns at $31.5^\circ \leq 2\theta \leq 33.5^\circ$. More details can be found in Figure S1.

SFO50-CGO50 and SFO20-CGO80, respectively. In a first set of experiments, the phase structures of the as-prepared isolated SFO and composite SFO-CGO ceramics were investigated by room-temperature X-ray diffraction (XRD). As shown in Figure 1, the single-phase SFO has a complex perovskite structure (mainly tetragonal); moreover, both the SFO80-CGO20 and SFO50-CGO50 dual-phase materials exhibit a mixture of a major orthorhombic perovskite structure and a simple cubic fluorite structure, whereas the SFO20-CGO80 composite involves a cubic perovskite oxide and a cubic fluorite oxide. Clearly, increasing the content of the fluorite phase significantly influences the crystal structure of the neighboring perovskite. Accordingly, a possible cation interdiffusion ascribed to the formation of solid solutions during the synthesis and sintering processes would be supposed to take the responsibility for the certain deviations in the original lattice structure, which is due to the substantial difference in the cationic coordination numbers as well as ionic radii. Additionally, it is noticed that no impurity phase can be detected in the dual-phase composites, which reveals a good compatibility between the two phases.

Subsequently, the surface morphologies of all the dual-phase ceramics were closely examined (Figure 2). Obviously, the diverse grains could be distinguished in the back-scattered electron (BSE) micrographs by various grey levels owing to different atomic numbers. In all cases, the sintered composite ceramics consist of two different kinds of grains: the light grains and the dark ones. Note that the visual volume ratio of the light grains in these composites increases directly with an increase in the weight ratio of CGO, which corresponds to the greatly enhanced cubic fluorite reflections in the above XRD patterns. Therefore, it can be deduced that the light grains represent the CGO phase, whilst the dark ones correspond to the SFO phase. This is consistent with the information

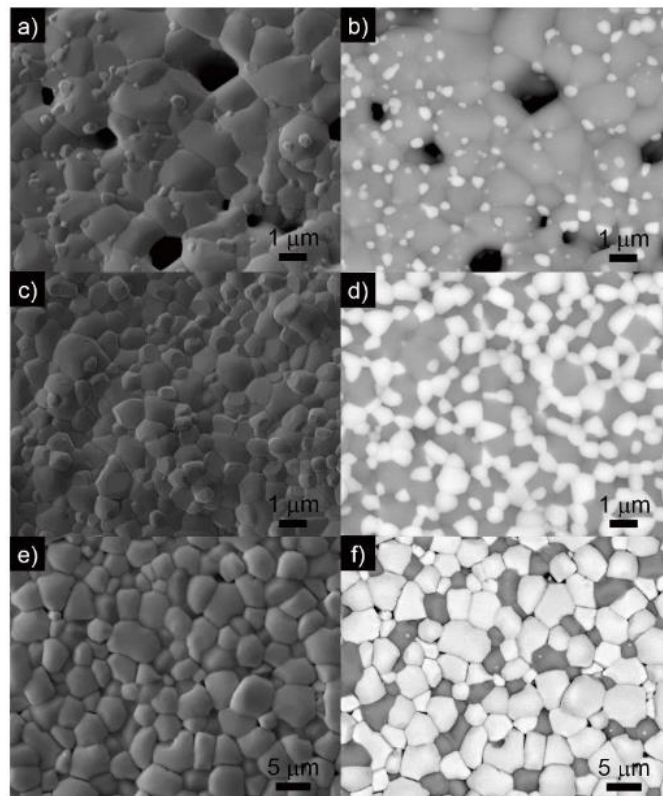


Figure 2. Secondary electron (a,c,e) and back-scattered electron (b,d,f) micrographs of the surface of the dual-phase SFO-CGO ceramics. a,b) SFO80-CGO20. c,d) SFO50-CGO50. e,f) SFO20-CGO80. The dark grains are the SFO perovskite phase, while the light grains are the CGO fluorite phase.

about the elemental distributions confirmed by the energy dispersive X-ray spectroscopy (EDXS) images of the composite ceramics (Supporting information, Figure S2 and S3).

To better understand the chemical nature of these perovskite and fluorite phases, the experiments of the electron probe microanalysis (EPMA) integrated with a wavelength dispersive X-ray spectroscopy (WDXS) were performed afterwards. The detailed approximate chemical compositions of the materials are presented in Table S1. It is definitely verified that a portion of Ce and Gd cations incorporated into the lattice of SFO perovskite, which indicates that a strong interdiffusional behavior existed in the composite materials. Furthermore, the elemental quantities and concentration distributions of Sr, Fe, Ce and/or Gd within single-phase SFO and dual-phase SFO20-CGO80 samples were carefully monitored by the EPMA line scan technique (Figure 3 and S4). It is demonstrated that both the Fe concentration and the atomic ratio of Sr/Fe remain relatively stable for the isolated SFO ceramic (Figure S4). For the SFO20-CGO80 composite sample, within a perovskite zone, the atomic fractions of Fe, Sr and Ce are almost constant from the centre towards the position near the edge, whereas there is a significant concentration fluctuation of the Gd element across the same area (Figure 3a). Moreover, it can be found simultaneously that the concentrations of Ce and Gd hold steady within a wide fluorite zone (Figure 3b).

3.3 A stabilized membrane reactor for partial oxidation of methane

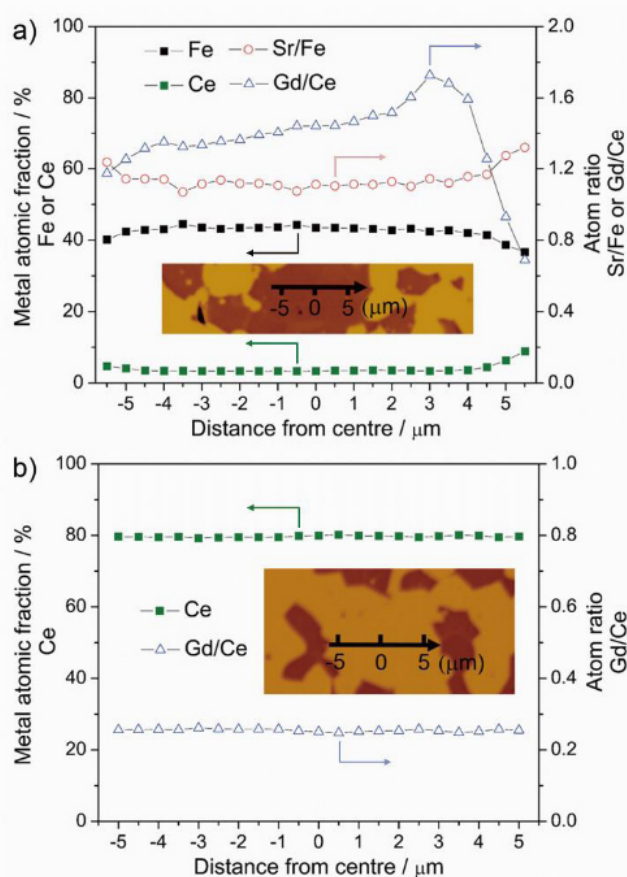


Figure 3. EPMA line scan of the metal atomic fraction or atom ratio as a function of the distance within a) a perovskite (brown) zone and b) a fluorite (yellow) zone respectively of the fractured SFO20-CGO80 sample. Note that the concentrations of Fe and Sr elements in b) are below the credible limit of detection.

On the basis of the above observations, it is reasonable to assume that the formation of SFO-CGO composite materials via a one-pot method can be divided into two progressive steps: solution and exsolution. Like a conventional doping method, when CGO at a very low content, the majority of Ce and Gd cations are prone to enter into the lattice of SFO perovskite. In other words, it is thought that the Ce and Gd ions preferably incorporate into the A- or B-site of the host SFO perovskite, which probably leads to the symmetry changes as well as lattice mismatch^[21] ascribed to the difference in ionic radii and coordination numbers (Table S2). Nevertheless, the exsolution process occurs when the Ce or Gd concentration reaches a sufficiently high concentration with respect to the solid solution limit such that the perovskite structure becomes unstable, and afterwards the Ce and Gd cations will spontaneously exsolve from the host perovskite to re-construct lattice and re-establish stoichiometry.

In addition, the existence of special CGO “islands” could be detected on the surface of SFO80-CGO20 composite ceramic (Figure 2a,b), which is regarded as an unambiguous evidence for the exsolution. Moreover, it is believed that to some degree the Gd concentration gradient in the perovskite can attribute to the high

solubility of Gd cation in the exsolved ceria oxide.^[12] As a consequence, the interdiffusional behaviors have a great impact on the oxygen non-stoichiometry of SFO perovskite. Hence, the anticipated phase transitions of the perovskite from tetragonal to orthorhombic/cubic structure have been accompanied by the immense changes in the chemical composition of the composite materials, which implies an interdiffusion-induced transformation mechanism in the solid oxides. Since a large number of applications of perovskite-based materials are targeted on the elevated temperatures, in-situ XRD was employed to evaluate the phase stability of the SFO20-CGO80 composite materials (Figure S5). It is noticed that both the cubic perovskite and cubic fluorite phases maintain unchanged during a temperature variation from 30 to 1000 °C, which suggests good structural stability of the two phases. This findings indicate that the deleterious phase transition of SFO perovskite can be fully prevented by compositing the dual-phase materials via a one-pot method.

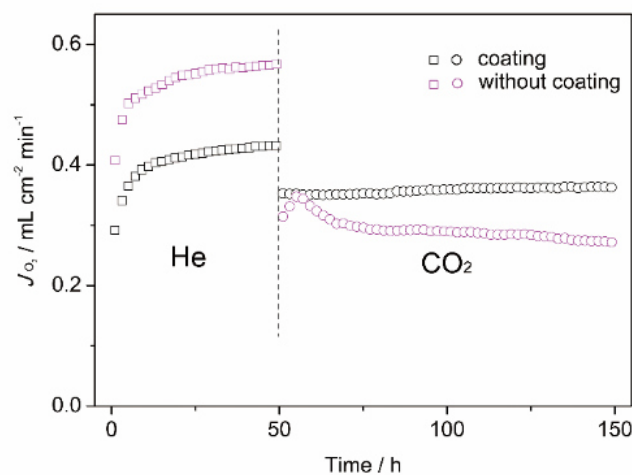


Figure 4. Oxygen permeation fluxes of SFO20-CGO80 dual-phase membrane at 900 °C. Condition: 100 mL min⁻¹ synthetic air (21 vol.% O₂-79 vol.% N₂) as the feed gas, 35 mL min⁻¹ He or CO₂ and 1 mL min⁻¹ Ne as the sweep gas, respectively. Note that a porous 20-μm-thickness CGO layer was coated on the sweep side.

As an appropriate demonstration of the success of the stabilization approach by interdiffusional tailoring, oxygen permeation measurements were carried out afterwards. First of all, pure He and CO₂ were applied as the sweep gas respectively to measure the oxygen permeability of an uncoated 0.5-mm-thickness SFO20-CGO80 composite membrane. As expected (Figure 4), the oxygen permeation fluxes sharply increase initially and then gradually reach to a stable level (around 0.57 mL min⁻¹ cm⁻²) under air/He gradient, which may be explained as the readjustment or reoxidation of the lattice structure from the as-prepared to the operational state.^[22,23] However, after altering the sweep gas from He to CO₂, sudden drop in oxygen fluxes can be detected owing to the degradation of oxygen surface-exchange kinetics caused by CO₂ adsorption, while the later continuous decrease during hundred hours of operation will be put down to the formation of carbonates.^[24,25] According to our previous study, suppressing the CO₂ adsorption

3 Dual-phase membrane reactors

on the surface of alkaline-earth containing perovskite will benefit to stabilize the oxygen permeation behavior of OTMs.^[24] Therefore, a porous CO₂-tolerant CGO^[26] layer was introduced to the SFO20-CGO80 membrane. Consequently, the dual-phase membrane with CGO protective layer shows remarkable stability in a CO₂-rich atmosphere. Moreover, compared to the bare membrane, slightly lower (about 25% loss) oxygen permeability was obtained for the CGO coated composite membrane when swept by He, which is attributed to the slow oxygen surface exchange kinetics,^[26] mainly owing to the lack of electronic conduction for CGO material under a relatively high oxygen partial pressure condition.^[12]

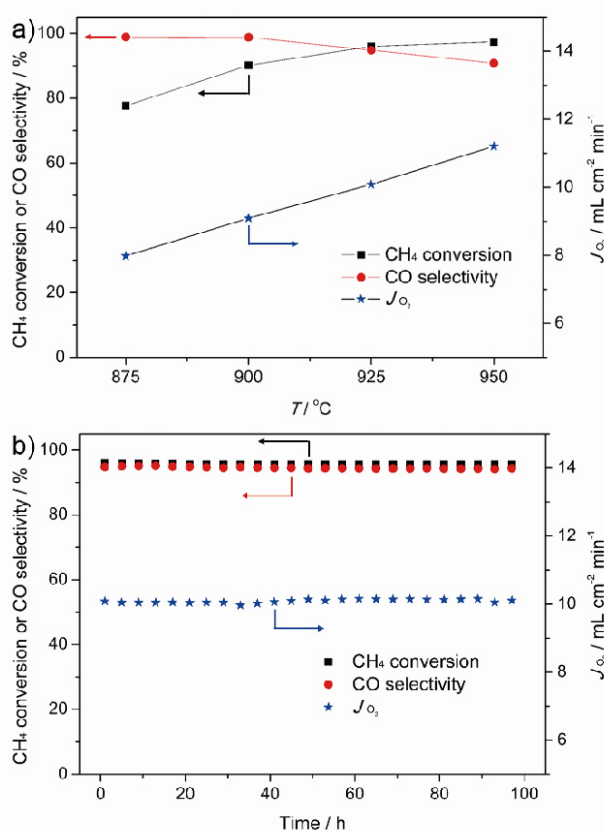


Figure 5. a) Temperature dependent of CH₄ conversion, CO selectivity and oxygen permeability through a CGO-coated SFO20-CGO80 composite membrane reactor. b) Long-term performance of the POM membrane reactor at 925 °C. Condition: 100 mL min⁻¹ synthetic air (21 vol.% O₂-79 vol.% N₂) as the feed gas, 7.5 mL min⁻¹ CH₄ and 1 mL min⁻¹ Ne as the sweep gas, respectively.

It is interesting to note that CGO will be easily converted to a mixed conductor with n-type electronic conductivity in a reducing atmosphere, resulting from the reduction of Ce⁴⁺ to Ce³⁺.^[12] Hence, it is concluded that the CGO-coated SFO20-CGO80 dual-phase membrane may be suitable to employ in a POM membrane reactor. In a commercial operation, a pure methane feed is much better than dilute methane, because no additional step is required to further separate the product gas and diluting gas. Thus, pure methane was used in the following experiments. Figure 5 presents the

effects of temperatures on CH₄ conversion, CO selectivity and oxygen permeability in the POM membrane reactor. As the temperature increases from 875 to 950 °C, the CH₄ conversion and oxygen permeation fluxes increase gradually from 77.7% to 97.4% and from 7.98 to 11.21 mL min⁻¹ cm⁻² respectively, nevertheless the CO selectivity decreases a little from 98.9% to 90.8% at the same time. Generally speaking, elevating the temperature can effectively accelerate the oxygen permeation process,^[27] which increases the amount of the permeated oxygen resulting in an increase in the methane conversion, and meanwhile a small portion of excess oxygen will further oxidize CO to CO₂, leading to a decrease in the CO selectivity. To achieve a high performance of the POM reactor (both CH₄ conversion and CO selectivity at around 95%), the optimization temperature was fixed at 925 °C with the adjusted feed rate of methane. Accordingly, the membrane reactor was subjected to a constant operation measurement. A stable performance with CH₄ conversion of 95.6% and CO selectivity of 94.6% was observed over 100 h of operation. Simultaneously, a proper H₂/CO ratio of 1.9 was achieved due to the highly selective POM reaction, which contributes to integrate with a downstream Fischer-Tropsch synthesis.^[28]

In summary, a dual-phase composite OTM reactor with high permeability and outstanding stability was successfully fabricated. It is further demonstrated that interdiffusion, which is omnipresent in composite materials, has a significant influence on the chemical compositions and phase structure/stability of each individual component. Therefore, it is reasonable to foresee that the proper interdiffusion tailoring by a facile one-pot approach can give rise to the exciting and rational design and development of a wide range of functional composite materials with higher performance and better stability.

Acknowledgements

This work has been supported by German Research Foundation (DFG) (no. FE928/7-1). We also acknowledge A. Wollbrink for technical support.

Keywords: perovskite • composite materials • oxygen-transporting membrane • phase stability

- [1] S. Sengodan, S. Choi, A. Jun, T. H. Shin, Y. W. Ju, H. Y. Jeong, J. Shin, J. T. S. Irvine, G. Kim, *Nat. Mater.* **2014**, *14*, 205-209.
- [2] J. I. Jung, H. Y. Jeong, J. S. Lee, M. G. Kim, J. Cho, *Angew. Chem. Int. Ed.* **2014**, *53*, 4582-4586.
- [3] Z. P. Shao, S. M. Haile, *Nature* **2004**, *431*, 170-173.
- [4] J. Suntivich, H. A. Gasteiger, N. Yabuuchi, H. Nakanishi, J. B. Goodenough, Y. S. Horn, *Nat. Chem.* **2011**, *3*, 546-550.
- [5] J. W. Zhu, G. P. Liu, Z. K. Liu, Z. Y. Chu, W. Q. Jin, N. P. Xu, *Adv. Mater.* **2016**, *28*, 3511-3515.
- [6] Y. Liu, X. F. Zhu, M. R. Li, H. Y. Liu, Y. Cong, W. S. Yang, *Angew. Chem. Int. Ed.* **2013**, *52*, 3232-3236.
- [7] Y. Takeda, K. Kanno, T. Takada, O. Yamamoto, *J. Solid State Chem.* **1986**, *63*, 237-249.
- [8] I. Kaus, K. Wiik, K. Kleveland, B. Krogh, S. Aasland, *Solid State Ionics* **2007**, *178*, 817-826.

3.3 A stabilized membrane reactor for partial oxidation of methane

- [9] X. L. Yu, W. Long, F. J. Jin, T. M. He, *Electrochim. Acta* **2014**, *123*, 426-434.
- [10] V. V. Kharton, A. P. Viskup, A. V. Kovalevsky, J. R. Jurado, E. N. Naumovich, A. A. Vecher, J. R. Frade, *Solid State Ionics* **2000**, *133*, 57-65.
- [11] P. M. Ajayan, J. M. Tour, *Nature* **2007**, *447*, 1066-1068.
- [12] M. Mogensen, N. M. Sammes, G. A. Tompsett, *Solid State Ionic* **2000**, *17*, 2847-2854.
- [13] V. V. Kharton, A. V. Kovalevsky, A. P. Viskup, A. L. Shaula, F. M. Figueiredo, E. N. Naumovich, F. M. B. Marques, *Solid State Ionics* **2003**, *160*, 247-258.
- [14] J. H. Joo, K. S. Yun, Y. Lee, J. Jung, C. Y. Yoo, J. H. Yu, *Chem. Mater.* **2013**, *25*, 4387-4394.
- [15] F. Y. Liang, H. X. Luo, K. Partovi, O. Ravkina, Z. W. Cao, Y. Liu, J. Caro, *Chem. Commun.* **2014**, *50*, 2451-2454.
- [16] W. Fang, F. Steinbach, Z. W. Cao, X. F. Zhu, A. Feldhoff, *Angew. Chem. Int. Ed.* **2016**, *55*, 8648-8651.
- [17] X. F. Zhu, Q. M. Li, Y. F. He, Y. Cong, W. S. Yang, *J. Membr. Sci.* **2010**, *360*, 454-460.
- [18] X. F. Zhu, H. H. Wang, W. S. Yang, *J. Membr. Sci.* **2008**, *309*, 120-127.
- [19] W. Fang, F. Y. Liang, Z. W. Cao, F. Steinbach, A. Feldhoff, *Angew. Chem. Int. Ed.* **2015**, *54*, 4847-4850.
- [20] D. P. Fagg, V. V. Kharton, J. R. Frade, *J. Electroceram.* **2002**, *9*, 199-207.
- [21] D. Neagu, T. S. Oh, D. N. Miller, H. Ménard, S. M. Bukhari, S. R. Gamble, R. J. Gorte, J. M. Vohs, J. T. S. Irvine, *Nat. Commun.* **2015**, *6*, 8120-8127.
- [22] X. F. Zhu, W. S. Yang, *AIChE J.* **2008**, *54*, 665-672.
- [23] J. Xue, A. Feldhoff, *J. Eur. Ceram. Soc.* **2016**, *36*, 3451-3456.
- [24] W. Fang, F. Steinbach, C. S. Chen, A. Feldhoff, *Chem. Mater.* **2015**, *27*, 7820-7826.
- [25] K. Efimov, T. Klände, N. Juditzki, A. Feldhoff, *J. Membr. Sci.* **2012**, *369*, 205-215.
- [26] I. G. Torregrosa, M. P. Lobera, C. Solís, P. Atienzar, J. M. Serra, *Adv. Energy Mater.* **2011**, *1*, 618-625.
- [27] C. Wagner, *Prog. Solid State Chem.* **1975**, *10*, 3-16.
- [28] H. Schulz, *Appl. Catal. A* **1999**, *186*, 3-12.

Supporting information

A method of stabilizing perovskite structure via interdiffusional tailoring and its application in an oxygen-transporting membrane reactor

Wei Fang, Chao Zhang, Frank Steinbach and Armin Feldhoff**

1. Experimental details

1.1 Synthesis of powders and membranes

The SrFeO_{3-δ} (SFO) single-phase powders were synthesized by the citric-nitrate combustion method.^[1] The dual-phase powders comprising of both SFO and Ce_{0.84}Gd_{0.16}O_{2-δ} (CGO) materials with various weight ratios of 80:20, 50:50 and 20:80 (abbreviations as SFO80-CGO20, SFO50-CGO50 and SFO20-CGO80, respectively) were prepared via a one-pot method.^[2] Additionally, a trace of copper cation (max. 1.5 wt.%) was introduced to the dual-phase precursors as the sintering aids.^[3] Briefly, the appropriate amounts of the metallic salts and citrate were dissolved in water and mixed in a beaker. After the water was evaporated, the resultant gel was combusted to remove the organic compounds, and then calcined in air at elevated temperatures. The powders were pre-calcined at 1100 °C for 10 h. Afterwards all the powders were pressed into disks under a pressure of ~20 MPa, then sintered at 1150 °C for 10 h. Subsequently, all the sintered SFO20-CGO80 dual-phase membranes were polished by sandpapers to achieve a 0.5 mm thickness for oxygen permeation test. Besides, a protective layer made of CGO materials was introduced to the SFO20-CGO80 membrane by slurry coating method^[4] to further evaluate the CO₂ tolerance as well as the performance of partial oxidation of methane (POM) reaction with a packed Ni-based commercial catalyst.

1.2 Characterization of membrane materials

The phase structures of the membrane materials were determined by X-ray diffraction (XRD, D8 Advance, Bruker-AXS, with Cu K α radiation) in the 2 θ range 20-80° with a step width of 0.02°. For the in-situ XRD tests in air between 30 °C and 1000 °C, the samples were hold 30 min at each temperature before collecting the patterns, and the heating/cooling rate amounted to 12 °C/min. Surface morphologies of the membranes were observed by secondary electron (SE) and back-scattered electron (BSE) contrast operated at 2-20 kV (JEOL JSM-6700F). The elemental distribution of the membrane surface was studied on the same electron microscope by energy dispersive X-ray spectroscopy (EDXS, Oxford INCA 300) at 10 kV. Moreover, the chemical

3.3 A stabilized membrane reactor for partial oxidation of methane

compositions of the materials were further investigated by an electron probe micro-analyzer (EMPA, CAMECA SX100) equipped with 5 automated wavelength-dispersive X-ray spectrometers (WDXS) and an energy-dispersive X-ray spectrometer (EDXS) at 15 kV.

1.3 Measurements of oxygen permeation

The oxygen permeation was conducted in a home-made high-temperature oxygen permeation device,^[5] and a permeation cell was formed by sealing the disk membrane onto an alumina tube using a glass ring. The effective surface areas of the membranes were around 0.45 cm². Synthetic air (100 ml min⁻¹; 21 vol% O₂ and 79 vol% N₂) was applied as the feeding gas, and high-purity helium (35 ml min⁻¹) or CO₂ (35 ml min⁻¹) or methane (7.5 mL min⁻¹) as the sweep gas, respectively. The flow rates of the gases were controlled by mass flow controllers (Bronkhorst, Germany). The effluents on the sweep side were analyzed by an online-coupled gas chromatograph (Agilent 6890A). The absolute flow rates of the effluents were calculated using high-purity neon (1 mL min⁻¹) as an internal standardization. The leakages of oxygen were no more than 5% for all the oxygen permeation tests and were subtracted when calculating the oxygen permeation fluxes.

2. Supporting figures and table

2.1 XRD analysis of ceramics

As shown in Figure S1, the X-ray diffraction patterns obtained for SFO materials can be indexed as various perovskite structures with different CGO content, while CGO materials exhibit the cubic fluorite structure in all cases, which indicates a significant interaction between two phases.

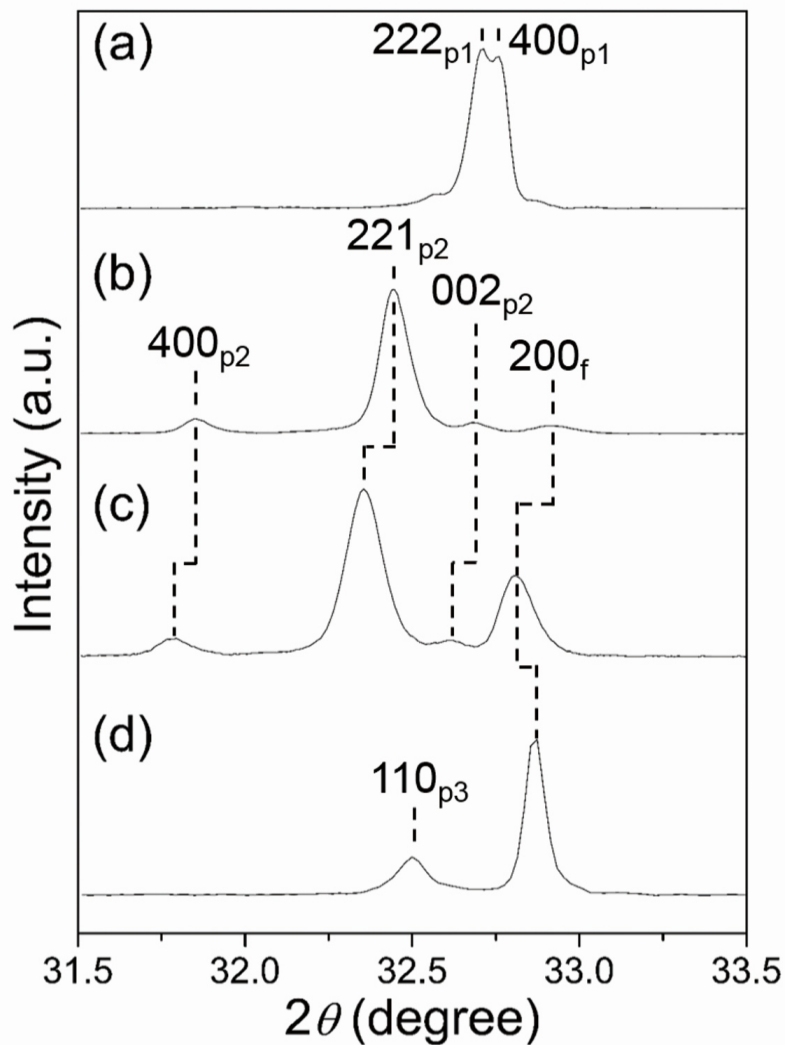


Figure S1 Close-up of the XRD patterns at $31.5^{\circ} \leq 2\theta \leq 33.5^{\circ}$ of Figure 1 of SFO single-phase and SFO-CGO dual-phase ceramics. a) SFO. b) SFO80-CGO20. c) SFO50-CGO50. d) SFO20-CGO80. Note that p1=tetragonal perovskite SFO (PDF #01-070-5776), p2=orthorhombic perovskite SFO (PDF #01-070-5777), p3=cubic perovskite SFO (PDF #00-040-0905), f=cubic fluorite CGO (PDF #01-075-0161). Indication of PDF number at Bragg positions refers to the powders diffraction file database.

2.2 SEM-EDXS analysis of the SFO-CGO dual-phase ceramics

As shown in Figure S2, SEM-EDXS results confirm the presence of Ce and Sr in two different preferential locations, which represent the fluorite phase and perovskite phase respectively.

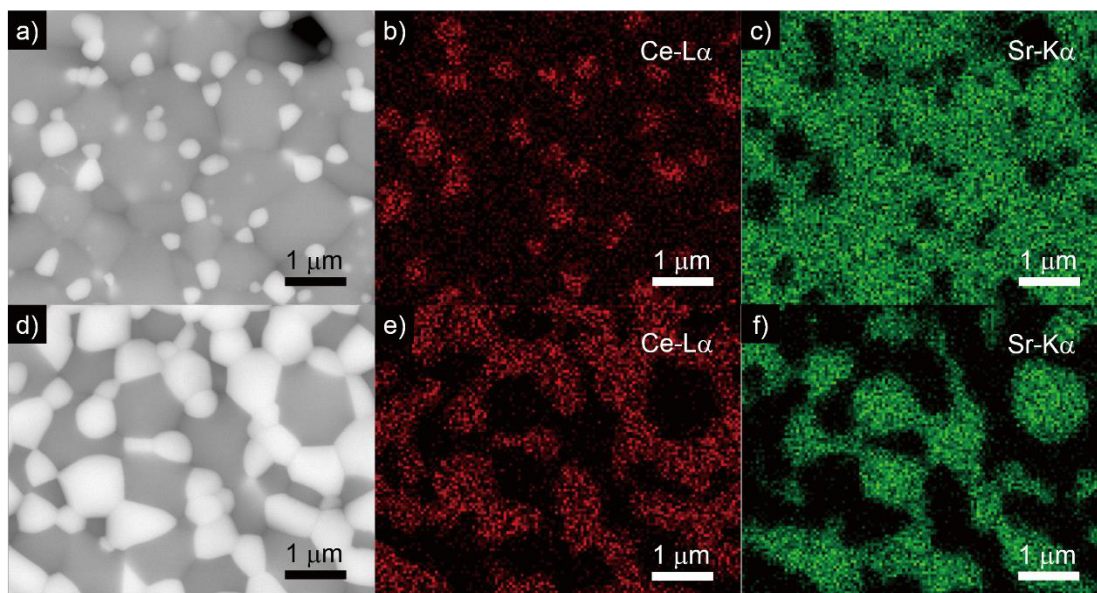


Figure S2 BSE micrographs of the surface of a) SFO80-CGO20 and d) SFO50-CGO50 dual-phase membranes. EDXS elemental distributions of b,e) Ce and c,f) Sr.

2.2 EMPA-mapping for SFO20-CGO80 composite membrane

As depicted in Figure S3, elemental mapping results clearly demonstrate that Sr and Fe have the same distribution, whereas Gd possesses the similar distribution with Ce. Therefore, the composite membrane appears to separate into two phases (perovskite and fluorite), which is also in agreement with the XRD analysis.

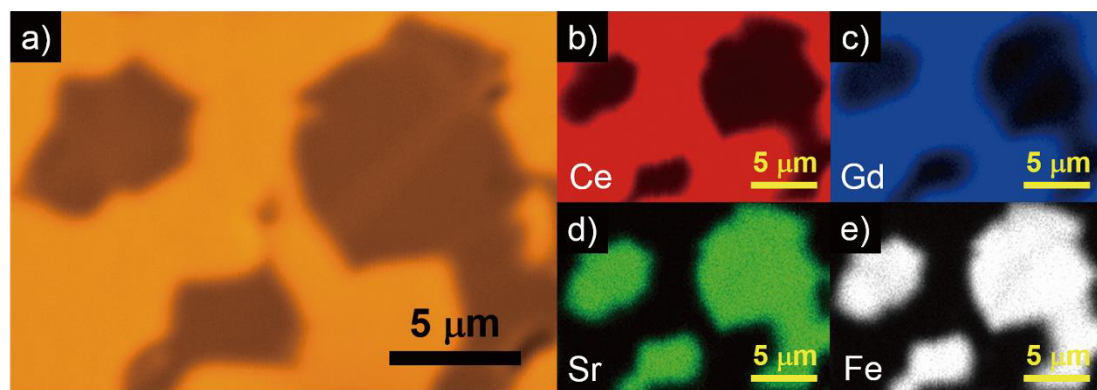


Figure S3 Mapping photographs of Ce, Gd, Sr and Fe within the fractured cross-section of SFO20-CGO80 composite membrane.

3 Dual-phase membrane reactors

Figure S4 describes that both the Fe and Sr concentrations keep stable for the single-phase SFO ceramic. In other words, no obvious concentration gradients of Fe or Sr can be detected.

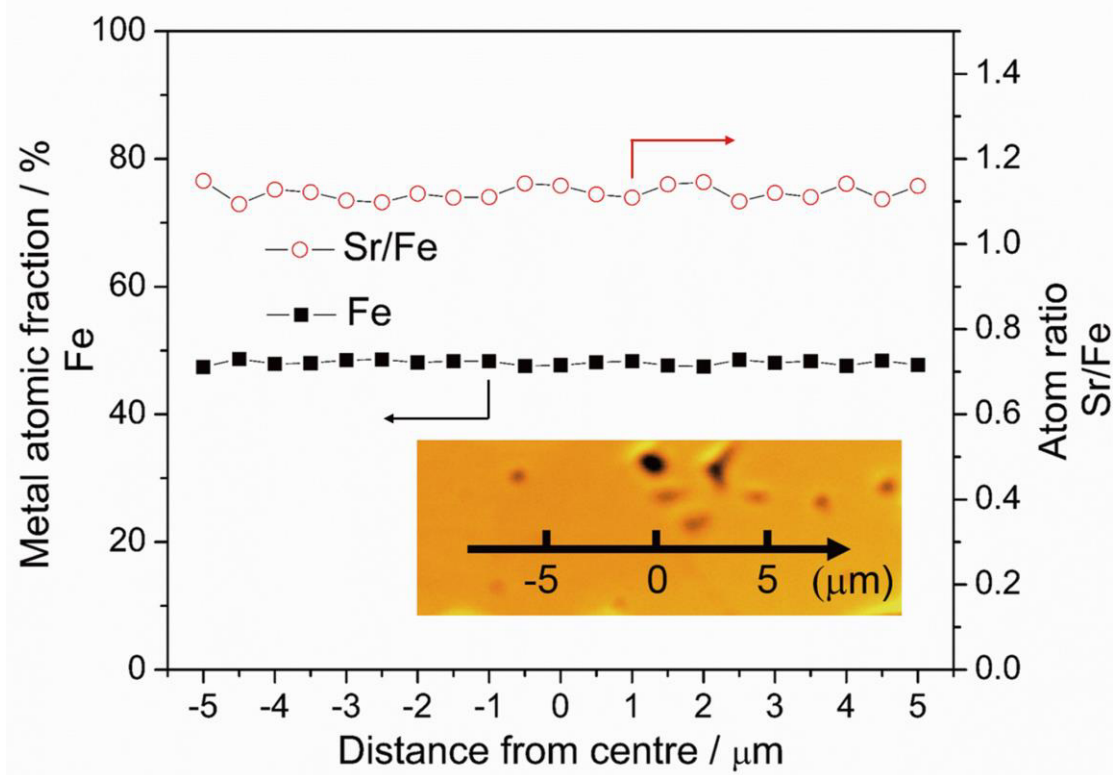


Figure S4 EPMA line scan of the metal atomic fraction or atom ratio as a function of the distance within the fractured SFO single-phase ceramic.

2.4 Chemical nature of the materials

As displayed in Table S1, it is concluded that a portion of Ce and Gd cations incorporated into the lattice of SFO perovskite, which indicates that a strong interdiffusional behavior existed in the one-pot composite systems.

Table S1 The main elemental compositions of the single-phase and dual-phase materials by EMPA measurements. Note that A or B-site occupancy could not be described by this method.

nominal composition	main metal atomic fraction / %					
	perovskite phase				fluorite phase	
	Sr	Fe	Ce	Gd	Ce	Gd
SFO	48.06	51.94	/	/	/	/
SFO80-CGO20	45.30	47.57	5.41	1.72	84.86	15.14
SFO50-CGO50	41.81	38.70	14.50	4.99	79.91	20.09
SFO20-CGO80	46.80	43.43	4.78	4.99	80.35	19.65

3.3 A stabilized membrane reactor for partial oxidation of methane

Table 2 shows the effective ionic radii and coordination number for several metal ions, which gives some useful hints for cation substitution. Thus, it can be deduced that both Ce and Gd cations will probably enter into A or B-site position of the perovskite.

Table 2 Some effective ionic radii according to crystallographic sites (Ln in an LnO₂ fluorite with 8-fold coordination, while A and B in an ABO₃ perovskite with 12-fold and 6-fold coordination, respectively).^[6] For Fe³⁺, the electronic spin is taken into consideration by giving values for low-spin/high-spin.

phase	site	cation	coordination number	effective ionic radius (pm)
fluorite	Ln	Ce ⁴⁺	8	97
		Ce ³⁺	8	114.3
		Gd ³⁺	8	105.3
perovskite	A	Sr ²⁺	12	144
		Ce ³⁺	12	134
		Gd ³⁺	9	110.7
	B	Fe ⁴⁺	6	58.5
		Fe ³⁺	6	55 / 64.5
		Ce ⁴⁺	6	87
		Gd ³⁺	6	93.8

2.5 Phase stability of SFO20-CGO80 dual-phase materials

As shown in Figure S5, both SFO perovskite and CGO fluorite exhibit the cubic symmetry over the entire temperature range (30 °C-1000 °C) during the heating up and cooling down processes. Moreover, it is noticed that the main reflections of both perovskite and fluorite materials gradually shift to the low angles during heating process, while move to the high angles during cooling down. Additionally, the lattice coefficients of thermal expansion (CTEs) of fluorite phase in the composite materials are $13.35 \times 10^{-6} \text{ K}^{-1}$ (heating up) and $13.27 \times 10^{-6} \text{ K}^{-1}$ (cooling down), while the CTEs of perovskite phase are $18.71 \times 10^{-6} \text{ K}^{-1}$ (heating up) and $19.06 \times 10^{-6} \text{ K}^{-1}$ (cooling down), respectively.

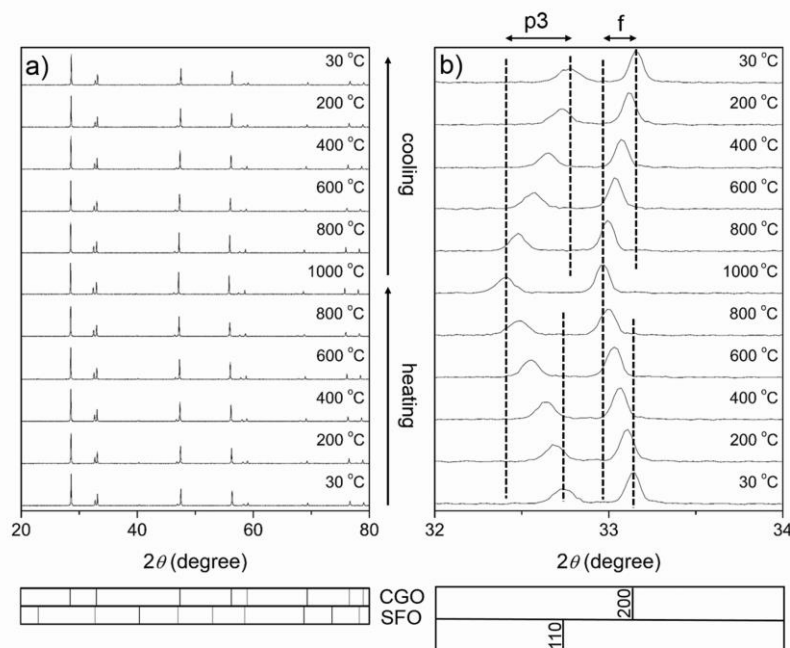


Figure S5 a) In situ XRD patterns of SFO20-CGO80 dual-phase powders in air. b) Close-up of the XRD patterns at $31.5^\circ \leq 2\theta \leq 33.5^\circ$. The dash vertical lines denote the temperature dependent limits of angular position of the reflections. p3=cubic perovskite SFO (PDF #00-040-0905), f=cubic fluorite CGO (PDF #01-075-0161).

References

- [1] Y. Y. Liu, B. Li, X. Wei, W. Pan, *J. Am. Ceram. Soc.* **2008**, *91*, 3926-3930.
- [2] X. F. Zhu, H. H. Wang, W. S. Yang, *J. Membr. Sci.* **2008**, *309*, 120-127.
- [3] C. Kleinlogel, L. J. Gauckler, *Adv. Mater.* **2001**, *13*, 1081-1085.
- [4] X. F. Zhu, H. Y. Liu, Q. M. Li, Y. Cong, W. S. Yang, *Solid State Ionics* **2011**, *185*, 27-31.
- [5] F. Y. Liang, H. X. Luo, K. Partovi, O. Ravkina, Z. W. Cao, Y. Liu, J. Caro, *Chem. Commun.* **2014**, *50*, 2451-2454.
- [6] R. D. Shannon, *Acta Cryst.* **1976**, *A32*, 751-767.

Publications and conferences

Publications included in this thesis

1. **Wei Fang**,* Fangyi Liang, Zhengwen Cao, Frank Steinbach, Armin Feldhoff, A mixed ionic and electronic conducting dual-phase membrane with high oxygen permeability, *Angewandte Chemie International Edition* **2015**, *54*, 4847-4850.
2. **Wei Fang**,* Frank Steinbach, Chusheng Chen,* Armin Feldhoff, An approach to enhance the CO₂ tolerance of fluorite-perovskite dual-phase oxygen-transporting membrane, *Chemistry of Materials* **2015**, *27*, 7820-7826.
3. **Wei Fang**,* Frank Steinbach, Zhongwei Cao, Xuefeng Zhu,* Armin Feldhoff*, A highly efficient sandwich-like symmetrical dual-phase oxygen-transporting membrane reactor for hydrogen production by water splitting, *Angewandte Chemie International Edition* **2016**, *55*, 8648-8651.
4. **Wei Fang**,* Chao Zhang, Frank Steinbach, Armin Feldhoff,* A method of stabilizing perovskite structure via interdiffusional tailoring and its application in an oxygen-transporting membrane reactor, submitted to *Angewandte Chemie International Edition*.

Publication not included in this thesis

5. Yanying Wei,* Jian Xue, **Wei Fang**, Yan Chen, Haihui Wang,* Jürgen Caro, Enhanced stability of Zr-doped Ba(CeTb)O_{3-δ}-Ni cermet membrane for hydrogen separation, *Chemical Communications* **2015**, *51*, 11619-11621.

Contributions to conferences

1. **Wei Fang**, Benjamin Geppert, Jian Xue, Armin Feldhoff, Ca-containing and cobalt-free CO₂-tolerant perovskite materials for oxygen separation, *Electroceramics XIV*, 16th-20th June **2014**, Bucharest, Romania, (**Talk**).
2. **Wei Fang**, Chusheng Chen, Armin Feldhoff, CO₂ reforming of methane to synthesis gas in a CO₂-tolerant dual-phase oxygen-transporting membrane reactor, *12th International conference on catalysis in membrane reactors (ICCMR12)*, 22nd-25th June **2015**, Szczecin, Poland, (**Talk**).

Curriculum Vitae

Personal data:

Name: Wei Fang
Date of birth: February 10th, 1988
Place of birth: Hefei, Anhui, China
Nationality: Chinese
Gender: Male
Marital status: Single



Higher education:

- Since 09/2013:** **Gottfried Wilhelm Leibniz University Hannover, Germany**
Ph.D. in Physical Chemistry at the group of Prof. Dr. Armin Feldhoff, Institute of Physical Chemistry and Electrochemistry.
- 09/2010 – 06/2013:** **University of Science and Technology of China, China**
Master in Materials Science and Engineering at the group of Prof. Dr. Chusheng Chen and Prof. Dr. Jianfeng Gao, School of Chemistry and Materials Science.
- 09/2006 – 06/2010:** **Northwestern Polytechnical University, China**
Bachelor in Materials Engineering, School of Materials Science and Engineering.